Summer 9-8-2017

Compositional and Physical Gradients in the Magmas of the Devine Canyon Tuff, Eastern Oregon: Constraints for Evolution Models of Voluminous High-silica Rhyolites

Shelby Lee Isom
Portland State University

Compositional and Physical Gradients in the Magmas of the Devine Canyon Tuff, Eastern Oregon: Constraints for Evolution Models of Voluminous High-silica Rhyolites

by

Shelby Lee Isom

A thesis submitted in partial fulfillment of the
requirements for the degree of

Master of Science
in
Geology

Thesis Committee:
Martin J. Streck, Chair
Ashley R. Streig
John Bershaw
Anita L. Grunder

Portland State University
2017

ABSTRACT

Large-volume silicic ignimbrites erupt from reservoirs that vary in composition, temperature, volatile content and crystallinity. The 9.7 Ma Devine Canyon Tuff (DCT) of eastern Oregon is a large-volume (>250 km^3), compositionally zoned and variably welded ignimbrite. The ignimbrite exhibits heterogeneous trace element compositions, variable volatile content and crystallinity. These observations were utilized in the investigation into the generation, accumulation and evolution of the magmas composing the DCT. Building off previous research, pumices were selected from the range of trace element compositions and analyzed with respect to crystallinity, mineral abundances and assemblages. The DCT displays a gradational trace element enrichment and decrease in crystallinity from least evolved, dacite, at ~22% crystals to most evolved high-silica rhyolite at 3% crystals. Two distinct mineral populations of feldspar and clinopyroxene were identified in previous work, one belonging to the rhyolitic magma and the other to the dacitic magma. Volatile content derived from melt inclusion Fourier Transform Infrared (FTIR) spectrometer analysis revealed an increase in water content from 1.2 to 3.7 wt.% in the most evolved rhyolite. The DCT exhibits low and variable $\delta^{18}O$ signatures, 4.52‰ to 5.76‰, based on $\delta^{18}O$ values measured on quartz and sanidine. Low $\delta^{18}O$ signatures of all DCT rhyolites suggest the incorporation of hydrothermally altered crust into the melt. Furthermore, quartz phenocrysts from all high-silica rhyolite groups display dark oscillatory zoned cores and Ti-rich bright rims.

These data provide insight into how these magmas were generated and subsequently stored in the crust. Commonalities of petrographic and compositional

features among rhyolites, especially the zoning characteristics of quartz phenocrysts, exclude the possibility of storage and evolution in multiple reservoirs. Envisioning a scenario where all magmas are stored within a single reservoir prior to eruption and assuming rhyolites A and D are the product of partial melting. The mixing of A and D rhyolites produced rhyolite B, and subsequent mixing of intermediate rhyolite B and end-member rhyolite D generated rhyolite C. However, some trace element inconsistencies, between mixing model and observed intermediate rhyolites suggest a secondary process. Post mixing, rhyolites B and C require some modification by fractional crystallization to account for LREE and other inconsistencies between mixed models and observed rhyolites. Finally, the origin of the dacite is likely through mixing of group D rhyolite and an intrusive fractionated basalt, which could have led to the eruption of the Devine Canyon Tuff.

TABLE OF CONTENTS

LIST OF TABLES

LIST OF FIGURES

INTRODUCTION

Large volume (>100 km^3) silicic pyroclastic flows consisting of hot gas, ash, pumice and lithic fragments are the product of destructive caldera forming eruptions, which can evacuate a thermally and compositionally zoned magma chamber (e.g., Hildreth, 1981; Streck and Grunder, 1997; Cathey and Nash, 2004). Large volume zoned magma chambers are of interest because the erupted products show signs of systematic tapping of heterogeneous and variously evolved parts of the magmatic system. Pre-eruptive gradients in composition, temperature, pressure and isotopic composition, among others, remain controversial and are central to constraining the mechanisms of how the magmatic system has evolved through time. Studying the depositional characteristics of ignimbrites, which preserve these gradients, provide insight into magma chamber dynamics prior to eruption.

Silicic, voluminous ignimbrites can exhibit chemical and physical characteristics such as: (1) a low (< 6.5‰) $\delta^{18}O_{magma}$ signature, which suggests introduction of low $\delta^{18}O$ roof rock, which has been modified by low $\delta^{18}O$ meteoric water, into the magmatic system; (2) strong trace element zonation with nearly invariant major elements; (3) trace element gradients and gaps seen in the chemical composition of crystals, pumice and bulk tuff imply discrete magmas were present in a contiguous magma chamber; and (4) variations in H_2O and CO_2 content and fluctuations in temperatures advocate for a heating event before eruption (Hildreth, 1981b; Hildreth et al., 1984; Cathey and Nash, 2004; Ellis et al., 2010).

Over the last several decades many researchers have hypothesized about processes that generate observed chemical and physical characteristics of these deposits. Among these were; (1) generation of low $\delta^{18}O$ rhyolites by cyclical eruptions and assimilation of hydrothermally altered carapace (Simakin and Bindeman, 2012); (2) successive melting events to generate rhyolites with recharge driven mixing (Wolff and Ramos, 2014); (3) segregation of magma into multiple smaller chambers (Ellis et al., 2010) and (4) remelting of cumulates to generate zoned silicic tuffs (Wolff et al., 2015). The mechanisms that generate high-silica rhyolitic magma bodies is a topic of much controversy, as there are arguments against all proposed models. Data and observations collected in this study will provide new insights into this poorly-understood process.

The Devine Canyon Tuff (DCT) is a high-silica (>75 wt% SiO_2), large volume (>250 km^3), crystal-poor to crystal-rich (>25%) ignimbrite situated in the Harney Basin of southeast Oregon. The DCT displays compositional gradients with respect to trace elements, low $\delta^{18}O$ values, variations in H_2O and CO_2 content and pre-eruptive temperature. The Devine Canyon Tuff covers an area of 30,000 km, and is the second best areal exposed tuff in the Harney Basin with respect to the Rattlesnake Tuff (Greene, 1973; Wacaster et al., 2011, Hess, 2014; Ford, 2011; Isom et al., 2016). The DCT is a widely exposed ash-flow tuff, existing data and data obtained in this study allow to test the proposed magma generation models outlined above and to create a hypothesized evolution model for the DCT.

BACKGROUND

High Lava Plains

The regional geology of the Pacific Northwest is complex, involving the subduction of the Juan de Fuca plate, extension of the Basin and Range province, and the Yellowstone hotspot track (Smith and Leudke, 1984; Pierce and Morgan, 1992; Hooper et al., 2002; Shoemaker and Hart, 2002). The High Lava Plains (HLP) is a high desert plateau, in southeastern Oregon, bounded by the Cascade Mountains to the west, the Northwest Basin and Range to the south and the Blues Mountains province to the north (**Figure 1**).

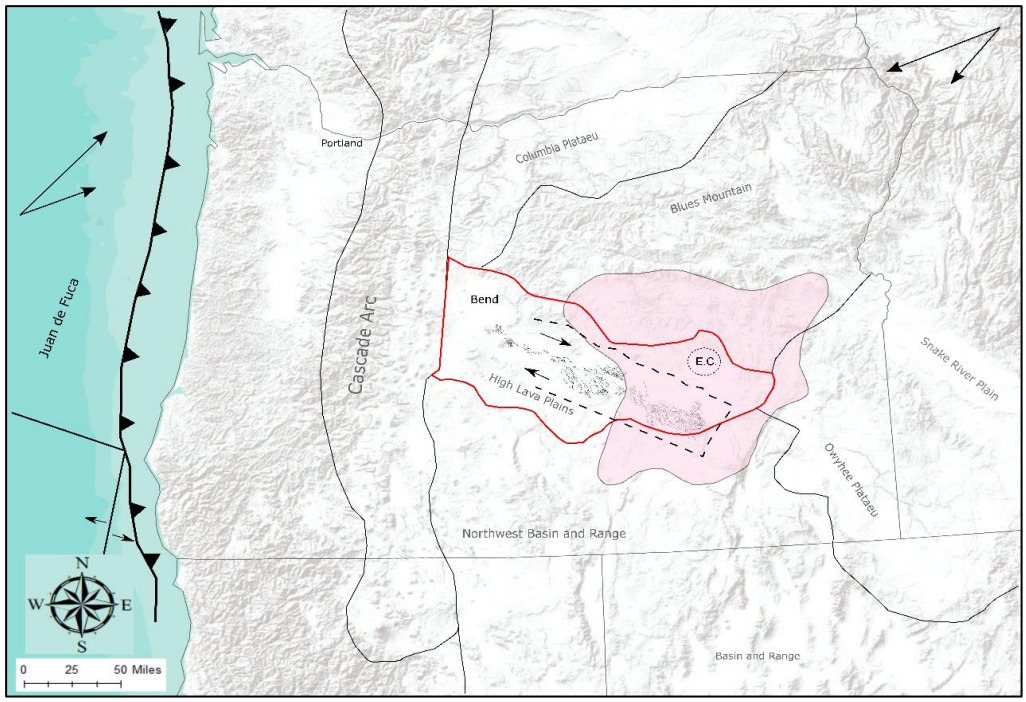

Figure 1. The High Lava Plains (outlined in red), regional plate motion for the Juan de Fuca plate and the North American plate and surrounding provinces (Dicken, 1950; Walker and MacLeod, 1991; Macleod, et al., 1995; Shoemaker and Hart, 2002; Ford et al., 2013). Regional fault escarpments and border of the Brothers Fault Zone (dashed black line) (modified from Trench et al., 2013). Extent of the Devine Canyon Tuff from this study (pink polygon).

Late Cenozoic volcanism associated with the High Lava Plains is bimodal. The volcanic rocks of the HLP that are 12 Ma and younger cover a total area of 25,000 km^2 and consist of basaltic lava flows, rhyolitic domes and flows, and ash-flow tuffs. Intermediate compositions are generally rare and estimated to only account for ~ 5% of the total volume of the <12 Ma volcanic rocks associated with the HLP (Ford et al., 2013). Dominant basalts are high-alumina olivine tholeiites, concentrated in four pulses of volcanic activity with the strongest around 7.5-8 Ma (Hart et al., 1984; Jordan et al., 2004; Streck and Grunder, 2012; Ford et al., 2013). These basalts erupted mainly as lava flows that do not indicate an age-progression trend along the HLP (Jordan, 2004). However, the rhyolites of the HLP display a west-northwest age progression from 10-12 Ma in the southeast moving west-northwest to the youngest eruptions (<1 Ma) near Newberry volcano (MacLeod et al., 1976; Jordan et al., 2004; Ford et al., 2013). This west-northwest younging trend of the High Lava Plains is a mirror image of the coeval east-northeast age progression of the rhyolites of the Snake River Plain. Extension within the HLP, extension coupled with rotation about a fixed point, Yellowstone plume head interaction and the involvement of slab subduction have all been attributed to the generation of these age-progressive rhyolites (Carlson and Hart, 1987; Fitton et al., 1991; Draper, 1991; Christiansen et al., 2002; Camp and Ross, 2004; Jordan et al., 2004; Ford et al., 2013). The Devine Canyon Tuff (DCT) (~9.7 Ma), the Prater Creek Tuff (8.5 Ma), and The Rattlesnake Tuff (7.1 Ma) are the three largest of five extensive tuffs that outcrop within the High Lava Plains and all have presumed sources within the greater

Harney Basin (Greene, 1973; Streck, 2014). Younger silicic centers crop out within the west-northwest younging track towards Newberry Volcano.

Extension during the Cenozoic created a region of normal faulting, known as the Basin and Range province (Wernicke, 1992; Trench et al., 2012). The northwestern corner of this province, characterized by immense displacement (>150 m) north-northeast trending normal faults, extends to the southern limit of the High Lava Plains. The Brothers fault zone (BFZ) runs NNW through the High Lava Plains marking the northern limit of the northwestern Basin and Range (NWBR) extensional province (**Figure 1)**. The BFZ is a ~50 km-wide region of distributed normal faulting that has been characterized by a right-lateral slip component (Lawrence, 1976; Trench et al., 2012).

The HLP sees modest amounts of rainfall and the water that is supplied to the Malheur and Harney Lakes, in the Harney Basin, originates from precipitation and snowmelt collected in the Silver, Silvies, Donner and Blitzen Rivers (Cummings et al., 2009). The headwaters of the Silver and Silvies Rivers originate in the Blue Mountains while the Donner and Blitzen River flows from the south, starting at Steens Mountains (**Figure 2**). At various sites in the Harney Basin oxygen isotope data have been collected from the Donner and Blitzen river, Silver Creek, Harney Lake and SE Harney Lake hot spring (Cummings et al., 2009). The Silver River average is slightly more negative, -15.35‰, than the Donner and Blitzen River value of -14.93‰. The average $\delta^{18}O$ value for all sampled surface water flowing into the Harney Basin is -15.1‰. A sampled hot

spring to the southeast of Harney Lake has an average $\delta^{18}O$ value of -15.4‰ (Cummings et al., 2009).

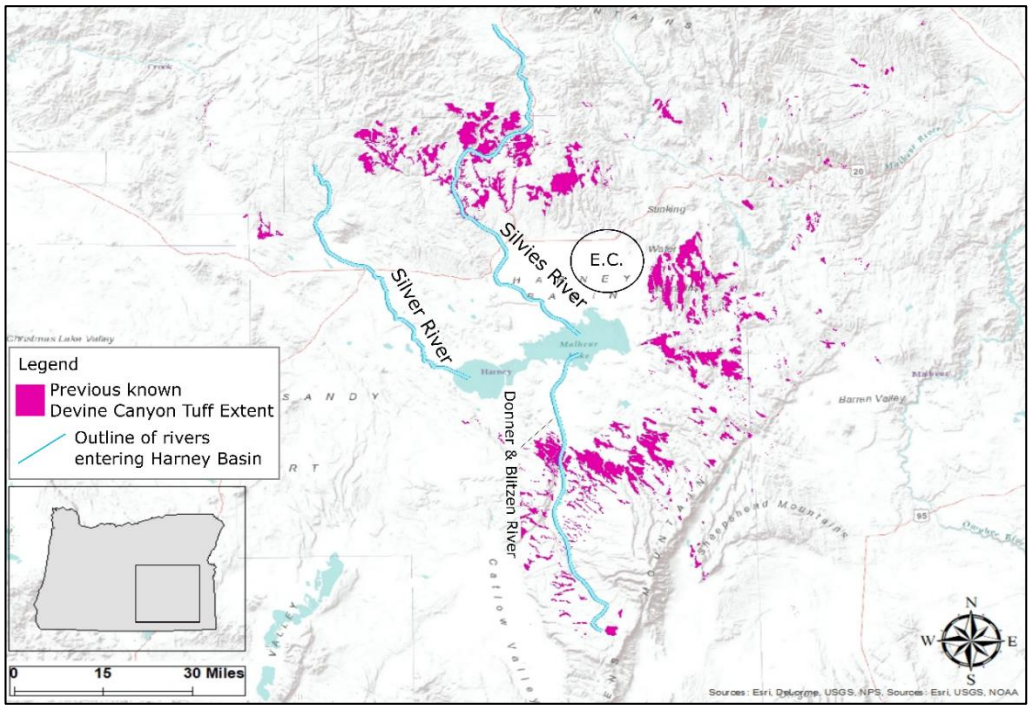

Figure 2. Exaggerated river outlines to accentuate origin. The headwaters of Donner and Blitzen River is located to the south at Steens Mountain. The river flows from south to north into the Harney Basin. The Silver and Silvies River flow north to south into the Harney Basin, with headwaters in the Malheur National Forest to the North. DCT location data from Oregon Geologic Data Compilation, version 6 (Brown, 1960; Walker, 1965; Greene, 1972a; Greene, 1972b).

The Devine Canyon Tuff (DCT)

The 9.7 Ma DCT of eastern Oregon is the second most widespread and voluminous ash-flow tuff in the area, covering an area of 30,000 km^2 with an eruptive volume of ~250-300 km^3. This has been calculated based on average outcrop thickness and measured distance between furthest extent of outcrops running ENE and WNW (Greene, 1973; this study). In 1973, Greene proposed the eruptive center of the DCT to be east of Burns, Oregon based on an ignimbrite thickness isopach map (**Figure 3**).

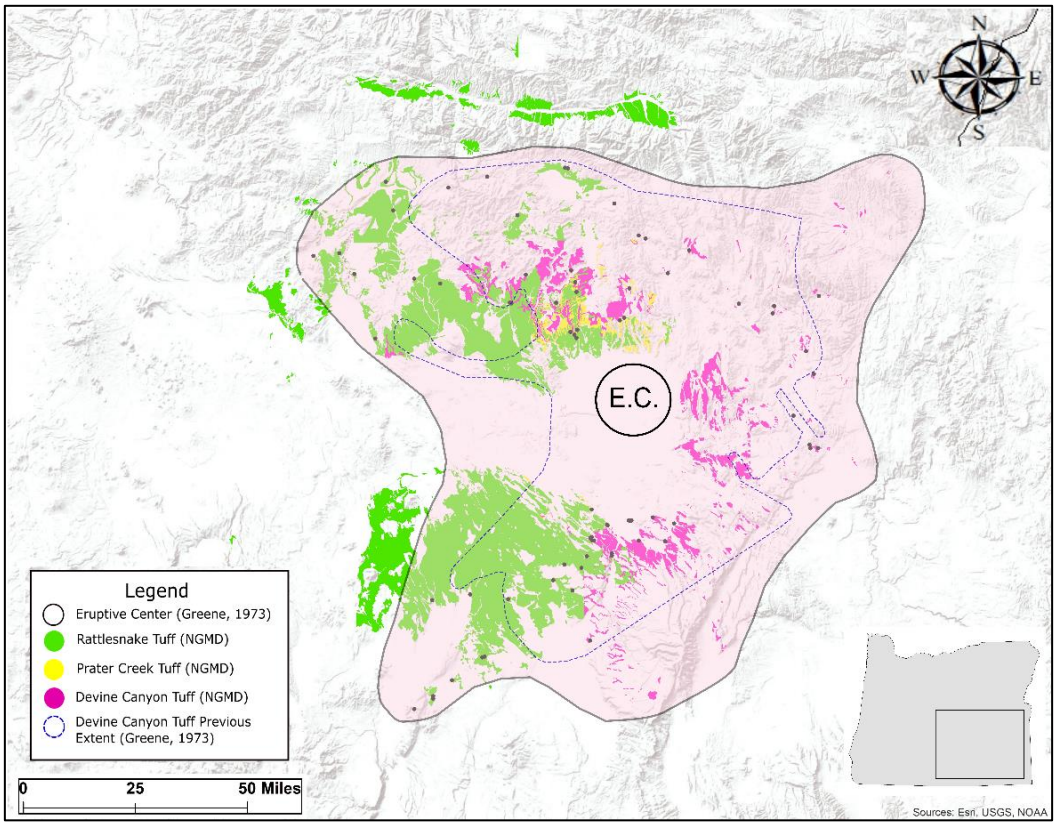

Figure 3. Extent of the Devine Canyon Tuff (pink polygon) determined from sample locations (black dots) from this study and previous studies (Wacaster et al., 2011; Streck, unpublished data). The Rattlesnake Tuff (green pattern), Prater Creek Tuff (yellow patttern) and Devine Canyon Tuff (dark pink pattern). Previous extent mapped by Greene 1973 (dashed blue line). Hypothesized eruptive center of the DCT by Greene, 1973 (dashed black line with E.C. in middle). All tuff location data from Oregon Geologic Data Compilation, version 6 (Brown, 1960; Walker, 1965; Greene, 1972a; Greene, 1972b).

Researchers have proposed that the DCT is a caldera forming eruption, based on

ignimbrite thickness and volume of erupted material (Greene, 1973). East-southeast of the city of Burns lies the caldera, now obscured by subsequent volcanism, and fluvial and pluvial sediments. The DCT is mildly peralkaline (Na+K/Al = 1.0-1.2) and almost entirely composed of rhyolitic compositions (74.6-77.6 wt% SiO_2) with invariable major elements, but a wide variation in trace element concentrations (Wacaster, 2011; Shafer, 2017). The DCT has a dacitic component (68.7-68.9 wt.% SiO_2) found as individual pumices or as streaks within banded pumices, comprised of both rhyolite and dacite. Glass analyses slightly extend the dacitic composition to 61-65% wt.% SiO_2. The DCT is a single cooling unit, which suggests the entire magma chamber erupted during a single eruptive episode (Smith, 1960; Ross and Smith, 1961; Greene, 1973; Wacaster et al., 2011; Shafer, 2017). The DCT varies in degree of welding, from non-welded to densely welded and contains vitric, devitrified and vapor phase zones. Stratigraphic gradation of crystallinity from phenocryst-poor (<5%) in basal sections to phenocryst-rich (>25%) in the upper most portions is observed in the ignimbrite. The thickest outcrops, proximal to the eruption center, exhibits increased crystallinity with respect to the most distal, thin outcrops (Greene 1973). A gradational decrease towards the margins of the tuff is also seen with respect to pumice, suggesting as the pyroclastic current advanced pumice winnowed out (Shafer, 2017). The pumice occurs in variety of forms from friable and highly porous in unwelded sections to fiamme in the densely-welded sections. Previously reported accessory phase minerals include apatite, britholite, chevkinite, Fe-Ti oxides and zircon (Shafer, 2017).

Existing Data – The Devine Canyon Tuff

This project is built upon the results and data from previous studies by Sue Wacaster, Martin Streck, and from Erik Shafer's MS Thesis (defended in Fall of 2016). Shafer (2017) divided the range of compositions observed in unbanded pumices into 4 rhyolite groups and 1 dacite group. These divisions were based on trace element concentrations, e.g. Zr, Nb, Th and Rb. The groups were labeled A-E, with group A being the most evolved and enriched in incompatible trace elements and group E being the least evolved (with respect to silica) and less enriched in trace elements (**Figure 4; Figure 5; Figure 6; Figure 7**). This study uses the same group naming convention as Shafer (2017) and added 22 pumice and bulk tuff samples (Appendix A).

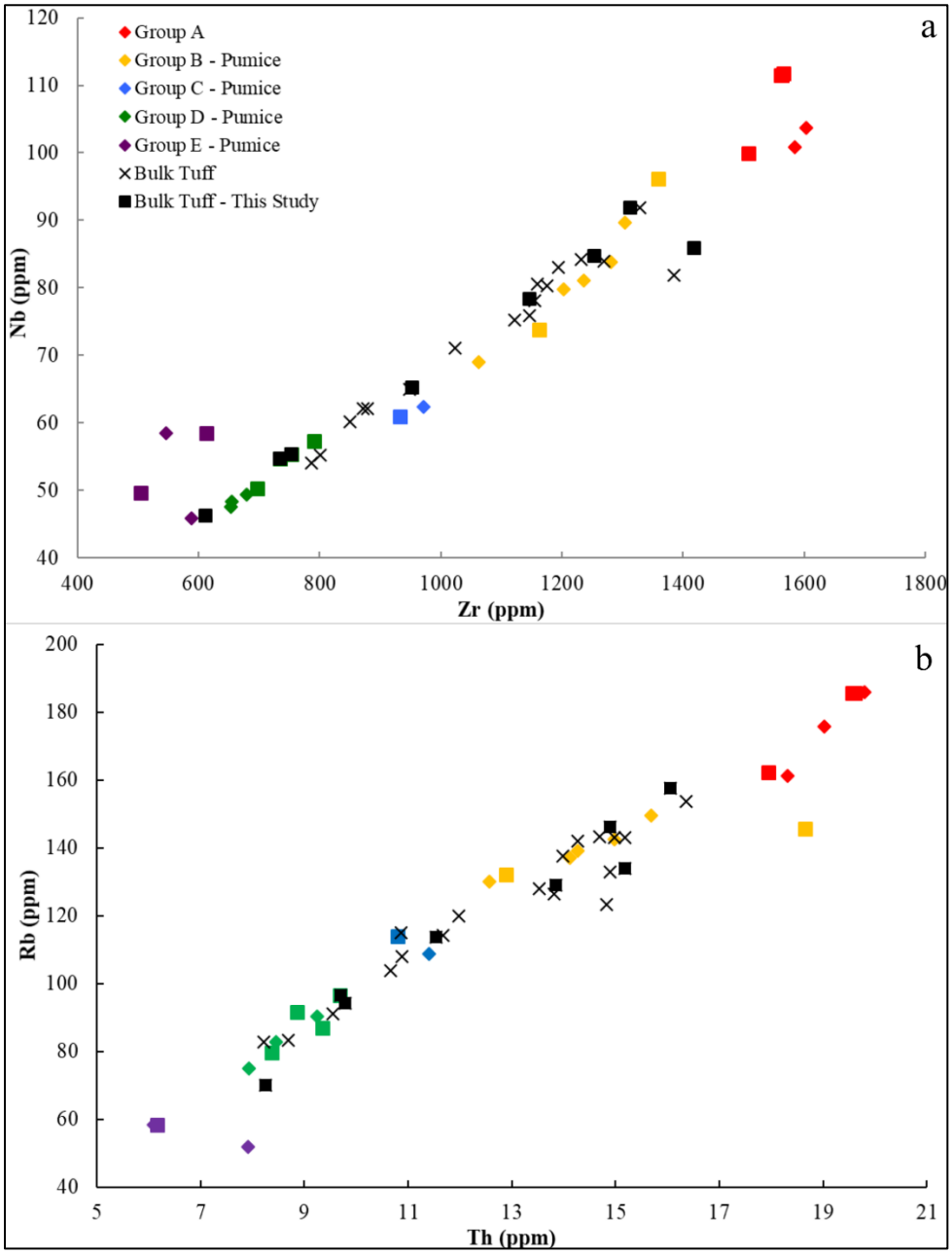

Figure 4. a) Zr vs. Nb concentrations for all compiled DCT data (previous and this study), b) Th vs. Rb concentrations for all compiled DCT data (Shafer, 2017; This study). Note the positive linear relationship among high-silica rhyolites from the least evolved group D compositions to most evolved group A pumice composition. Note most of group E dacite pumices do not fall on the same trend. Bulk tuff samples span nearly the range of pumices (colored icons) analyzed for each group. All samples with squares were collected and analyzed during this study, diamonds indicate samples from previous studies.

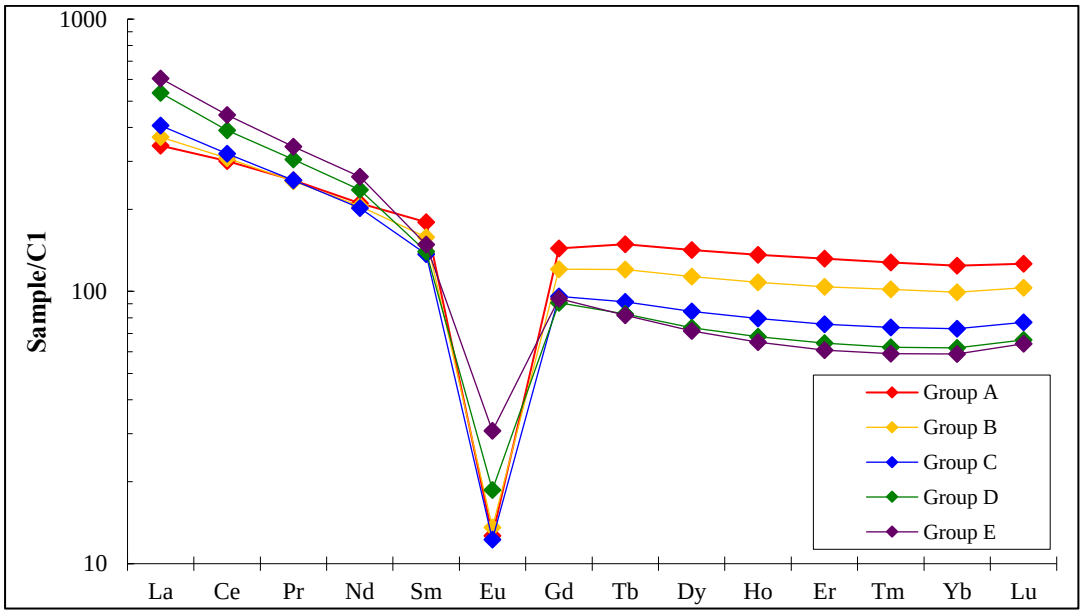

Figure 5. C1 chondrite normalized REE diagram for DCT average pumice compositions representing Group A through E (Shafer, 2017) The crystallization of feldspar yields a Eu anomaly, note the larger anomaly displayed by the high-silica rhyolites (A-D), with respect to the dacite (E), implying fractional crystallization occurred during their generation. Crystallization of chevkinite, D >>1 for LREE, yields a depletion of LREE relative to HREE for all groups (Mahood and Hildreth, 1983).

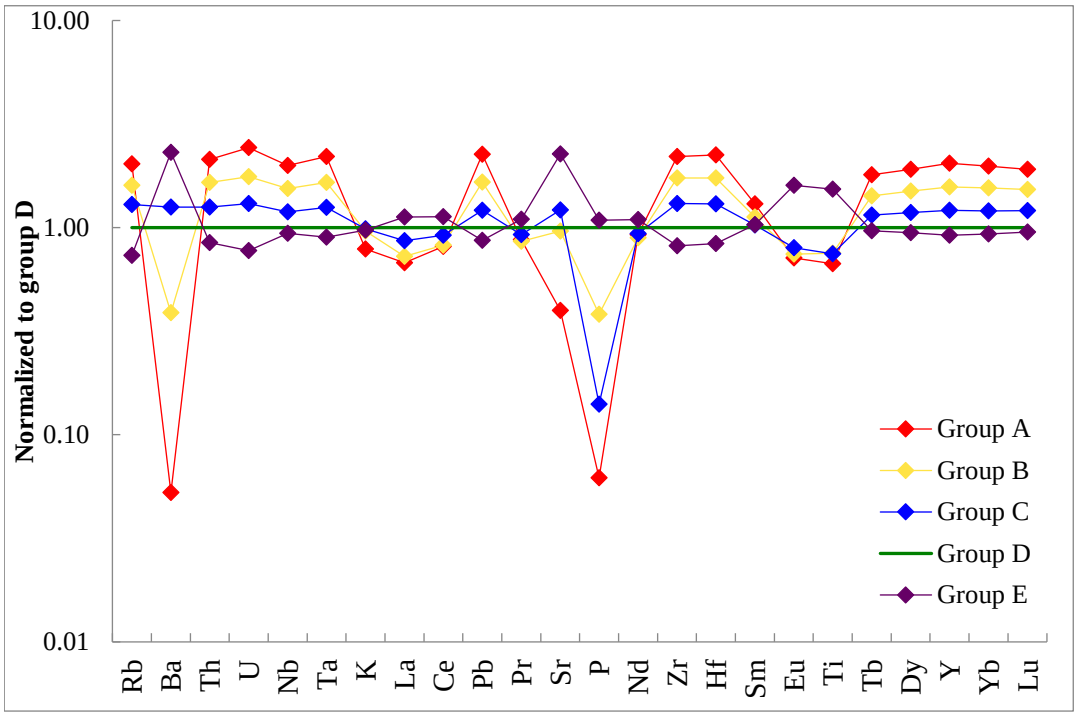

Figure 6. Enrichment factor diagram, all groups normalized to group D for DCT, all pumice samples from this study and Shafer (2017). Groups A, B and C display depleted Eu values, while group E exhibits an enrichment relative to group D. Group A and B are depleted in Ba and groups C and E are enriched relative to group D. Group E displays peaks in Sr, Eu, Ti and Ba. Elements Th, U, Nb and Tb, Dy, Y, Tb, Lu display a gradational enrichment pattern from group E to group A.

Crystallinity

Shafer (2017) analyzed and studied overall crystallinities within the DCT, groups A-E, through quantitative mineral separation after crushing and sieving pumices. Shafer (2017) found that groups display increasing crystallinity from the coarsest size fraction, >991 μm, to the <991 – 425 μm size fraction. All high-silica rhyolite groups yielded a decrease in crystallinity from <991 – 425 μm to <425 – 104 μm size fraction. Crystallinity increases in Group E, with decreasing size fraction, distinguishing it from all high-silica rhyolite groups.

Shafer (2017) calculated percent of felsic and mafic minerals present in each group. All high-silica rhyolite samples yield >92% total felsic crystals, with quartz being the dominant mineral in all groups except groups D and E where feldspar was more

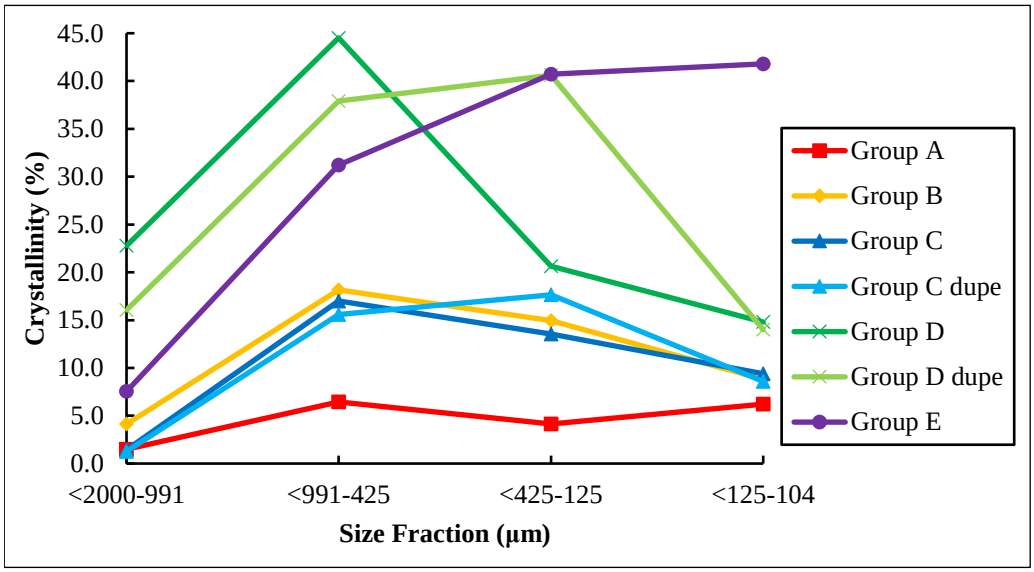

Figure 7. Percent crystallinity of each size fraction for each group (Shafer, 2017). Duplicates of group C and D indicated by "dupe". Groups B, C, and D exhibit similar patterns of decreasing crystallinity with decreasing size fraction after an initial increase. Group A shows nearly uniformly low crystallinity and group E is the only group that exhibits increasing crystallinity with decreasing size fraction.

prevalent. Quartz phenocrysts are subhedral to euhedral with pitted faces, evidence of resorption. In all high-silica rhyolite groups, mafic mineral content is <7.7% (Shafer, 2017). Overall crystallinity in the DCT decreases with increasing evolution degree of the magma from dacite to high-silica rhyolite D, C, B, and A (Shafer, 2017) (**Table 1**).

Table 1. Average crystallinity in each group within the Devine Canyon Tuff (Shafer, 2017).

Group	E (%)	D (%)	C (%)	B (%)	A (%)
Mass weighted average crystallinity	22.2	16.4	5.9	7.0	3.1

Mineral Data

Major and trace element variations among feldspars and pyroxenes within the DCT were also determined by Shafer (2017) with the electron microprobe. This revealed that high-silica rhyolite feldspar compositions grouped closely together while group E, dacite, trended away with increasing An % and Ab % and decreasing Or % percent. Trace element concentrations varied widely (e.g., 9 – 741 ppm Ba) within all groups for single feldspar analysis (Shafer, 2017). Feldspars group in two clusters when using trace elements of sanidine. Group E forms a distinct clustering with low Rb values (< 20 ppm) and higher Sr values (> 25 ppm) separating it from the high-silica rhyolite groups (A-D). The high-silica rhyolite groups trend away from Group E with increasing Rb (**Figure 8**). Interestingly, within the high-silica rhyolite groups A and D cluster together at Rb values of 30-40 ppm while groups B and C cluster at higher Rb values of > 45 ppm. Sanidine of groups B and C are the most enriched in incompatible trace elements, despite group A having the most evolved bulk composition (Shafer, 2017). Shafer (2017) concluded that the DCT displays two crystal populations with shared origins, one belonging to the high silica rhyolite groups A through D and the other representing the dacite, group E (**Figure 9**). Dacite and rhyolite groups exhibit tight clustering with respect to major element oxides in clinopyroxenes, however clino- and orthopyoxene xenocrysts identified (groups B, C and E) reflect a greater decrease in En% (Shafer, 2017). Group A represents the most enriched in REE and LREEs with respect to all other groups. Group B shows enrichment in HREE, Nb and Ta (Shafer, 2017) more so than all other groups (**Figure 10**).

Fayalitic olivine exists as a minor phase in the DCT (Shafer, 2017) and is characteristic of hot-(dry-)reduced rhyolites. Olivines are fayalitic in composition with the exception of group A (Shafer, 2017). One analyzed olivine revealed an increased MgO composition, closer to forsterite ($Mg_2SiO_{4,}$) for group A and we take it to be a xenocryst from regional basalt.

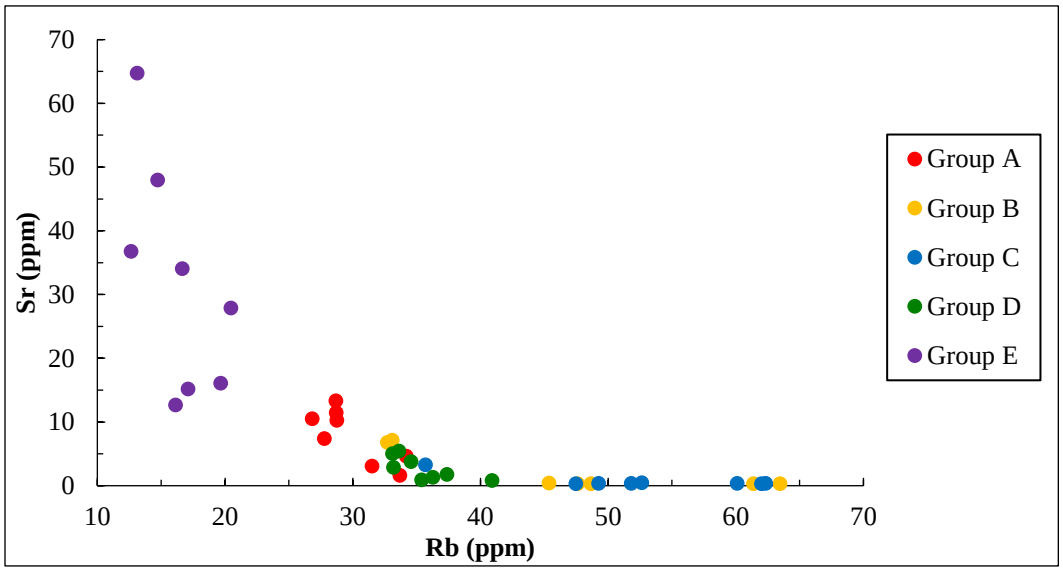

Figure 8. Rb vs. Sr (ppm) of feldspars from Shafer (2017). Sr is compatible into sanidine while Rb behaves incompatible. Group E yields widest Sr range with lowest Rb value. Groups B and C form clusters away from A and D.

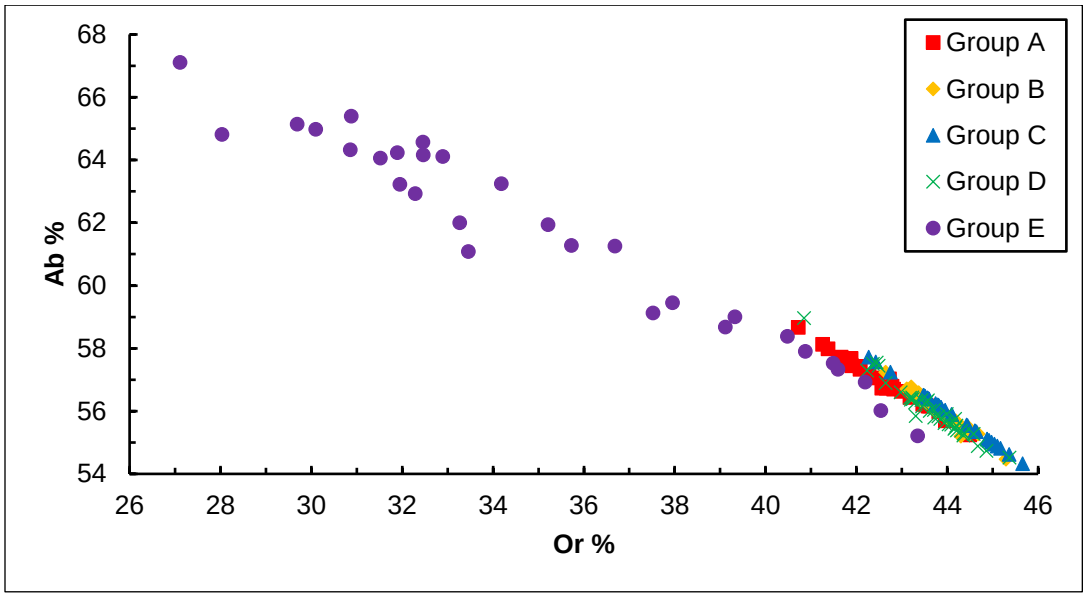

Figure 9. Or vs. Ab %, end member feldspar components, from Shafer, 2017. All groups display negative slope from dacite to high-silica rhyolites. Groups A-D trend away from group E, dacite, with decreasing albite and increasing orthoclase.

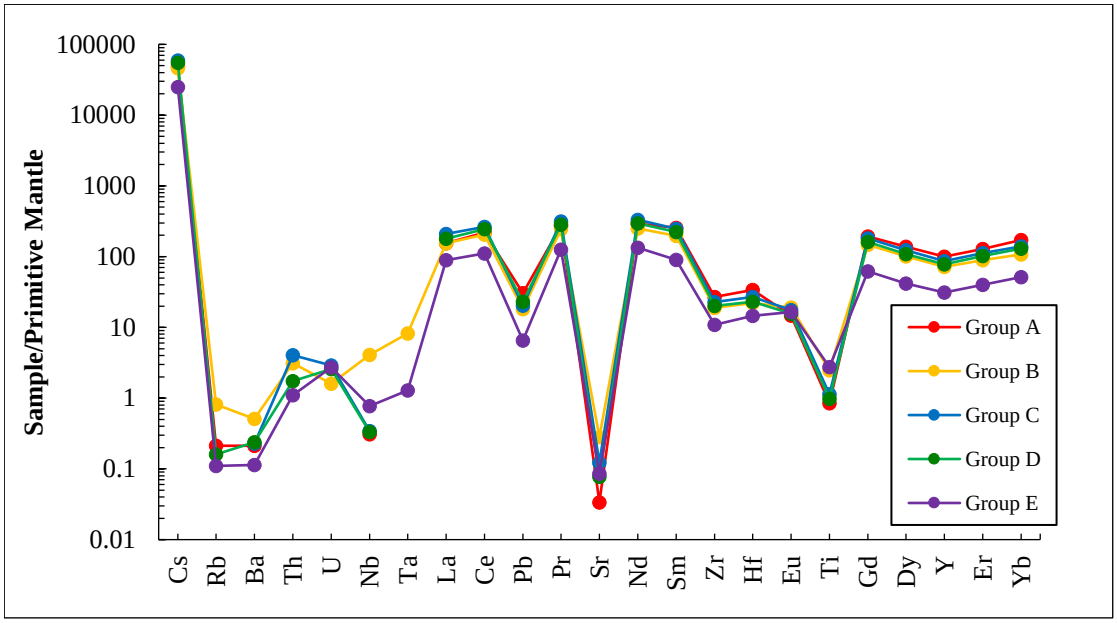

Figure 10. Primitive mantle (Sun and McDonough, 1989) normalized incompatible trace element diagram of average pyroxene trace element composition by group, from Shafer, 2017. Troughs display at Rb, Ba, Pb, Sr and Ti for all groups. Group B is enriched in HREE Nb and Ta compared to all other groups. Group A displays the most enriched concentrations from La to Yb. Group E is the least enriched concentration, except for Sr.

METHODS

Sample Selection

Field work was undertaken with three goals in mind: 1) to supplement existing pumice data, with the particular goal of sampling mafic pumices; 2) to collect banded pumices and distinguish chemical compositions within them and 3) to evaluate chemical zonation on outcrop scale by sampling and chemically analyzing outcrops from base to top.

Geochemical bulk analysis

Twenty-two samples were collected during the field component of this study for major and trace element analysis. These analyses were conducted at the GeoAnalytical Lab at Washington State University, using x-ray fluorescence (XRF) and inductively coupled plasma mass spectrometry (ICP-MS) following the methods of Johnson et al., 1999. Samples were crushed in house at Portland State University and transported to Washington State University for analysis. The GeoAnalytical Lab at WSU states the analytical precision for ICP-MS analysis is 5% (RSD) for Rare Earth Elements and 10% (RSD) for trace elements. The geochemical data obtained for samples collected during this study are found in Appendix A.

Melt Inclusions – CO_2 and H_2O

Shafer (2017) crushed pumice samples using a steal mortar and sieved into 991>425, 425>125 and smaller µm size fractions, for selecting matrix free phenocrysts. He separated hand-picked phenocrysts into mafic and felsic assemblages. I took his

separated felsic mineral fraction and picked large quartz phenocrysts from the 991>425 and 425>125 µm size fractions for further analysis. I submerged the selected quartz crystals in isopropyl alcohol and identified and selected phenocrysts that contain melt inclusions. Quartz crystals with melt inclusions were selected for FTIR analysis (**Figure 14**). I avoided crystallized inclusions as they are not representative of pre-eruptive melt (Wallace et al., 1999). I mounted selected single quartz crystals to a glass slide with crystal bond. I doubly polished the single quartz crystals to expose glass melt inclusions on both sides of the crystal using 600-grit paper, 6 µm and 1 µm polished pastes. Water was used as lubrication for the 600-grit paper and oil as lubrication for the pastes. The resulting wafer varied in thickness from ~40 – 150 µm. I took photos of the first side of the crystal before it was flipped, remounted and doubly polished. I used the photos to document the shape of the inclusions, presence of vapor bubbles, distance from rim and color.

The Fourier Transform Infrared (FTIR) spectrometer interfaced with a Continuum IR microscope at the University of Oregon was used to analyze quartz bearing melt inclusion wafers for CO_2 and H_2O concentrations. I calculated total CO_2 and H_2O concentrations with the Beer-Lambert Law:

$$c = \frac{M_i \cdot A}{\rho \cdot d \cdot \varepsilon} \qquad (1)$$

Where c_i is the concentration of the absorbing species, M_i is the molecular weight of the absorbing species (g/mol), A is the absorbance intensity (height) or the relevant vibration band, ρ is the density of the glass (g/L), d is the wafer thickness (cm) and ε is the molar absorptivity coefficient (L/mol cm). I determined the thickness of the wafer and melt

inclusion with a digital micrometer and the interference fringe method (Wysoczanski and Tani, 2006), used to double check micrometer accuracy. For samples >100 μm thickness the interference fringe method is not reproducible. The ρ and ε are strongly dependent on total H_2O concentration in rhyolitic systems. To correct for this an iterative process, provided by Madison Meyers, was used to converge on appropriate values. The starting ρ and ε values were based on Equation 2 (Skirius et al., 1990) and Equation 3 (Leschik et al., 2004):

$$\rho = 2350 - 12.6C_{H_2O} \quad (2)$$

$$\varepsilon = 80 - 1.36C_{H_2O} \quad (3)$$

Where C_{H_2O} is the concentration of total dissolved H_2O in weight %. Final densities (ρ) ranged from 2302 to 2341 kg/m^3, and final ε values are between 75.3-79.5 L/mol cm. I calculated total H_2O concentration by measuring the characteristic O-H molecule absorbance peaks at 3570 cm^{-1} and 1630 cm^{-1}, the molecular H_2O at 5230 cm^{-1} and the bound hydroxyl at 4520 cm^{-1}. I calculated CO_2 concentrations using the molecular CO_2 peak at 2350 cm^{-1} peak (**Figure 11**).

I applied a correction, described in detail by Befus et al., 2012, to samples GA_MI3 and GD_MI6 because of the interference of the host mineral, quartz, during data acquisition (**Figure 12**). The interference of quartz causes a dampening of the spectra acquired and a resulting peak at 1850 cm^{-1}. To correct for this I collected spectrum of the host mineral and measured the peak at 1850 cm^{-1}, I calculated the ratio for the noise related to quartz interference and the measured quartz (**Figure 12**). I

multiplied the calculated ratio of quartz by the total H_2O and CO_2 measured peaks, reversing the dampening effect caused by the quartz interference.

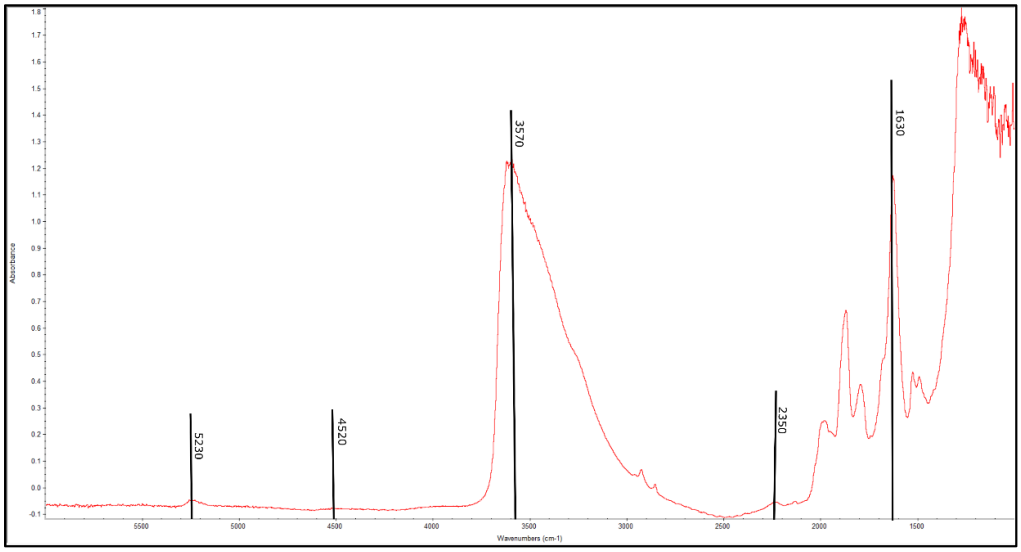

Figure 11. Spectra from sample GA_MI3. Vertical line indicates peak height of absorbance peaks measured for H_2O and CO_2 concentrations. O-H molecule absorbance peaks at 3570 cm^{-1} and 1630 cm^{-1}. Molecular H2O at 5230 cm^{-1}. Bound hydroxyl at 4520 cm^{-1}. Molecular CO_2 peak at 2350 cm^{-1} peak.

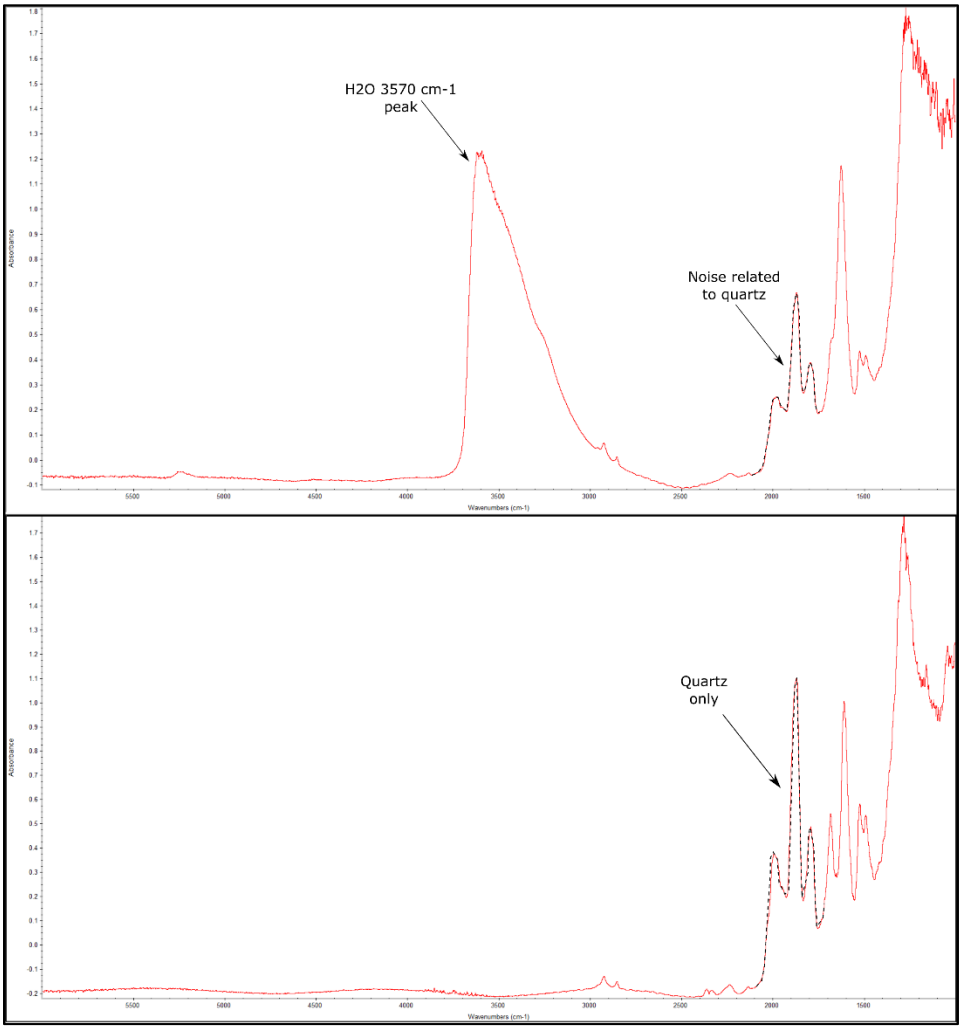

Figure 12. Top figure shows spectrum taken of GA_MI3 with noise related to quartz at the 1850cm^{-1} wavelength. Bottom figure is spectrum of quartz only. Peak height from quartz only was measured and the ratio of the quartz peak for the top and bottom spectra determined. The ratio was then applied to the spectrum of GA-MI3 canceling out the dampened signal caused by quartz interference.

Stable Isotopes - $\delta^{18}O$

Dr. Ilya Bindeman performed oxygen isotope analyses on single and bulk quartz and single and bulk sanidine phenocrysts at University of Oregon. Single crystal analysis is preferred over bulk analysis because the heterogeneity of the magma is lost when analyzing the bulk material. I chose single quartz and alkali feldspar crystals from the 991>425 and 425>125 µm size fractions, from Erik Shafer, and sent the samples to Dr. Ilya Bindeman at the University of Oregon. The oxygen was separated from the phenocrysts using laser fluorination and a 35W Newwave CO_2 IR laser. Final oxygen gas analysis was done using the Finnigan MAT 253, large radius 10 kv gas source mass spectrometer. Samples run on different days yielded standards of ±0.2‰ and ±0.14‰ for sanidine and quartz, respectively.

Accessory Phases

To evaluate accessory mineral assemblages, clinopyroxene crystals were targeted from each group as accessory phases are primarily found as inclusions in clinopyroxene crystals (Shafer, 2017). I plucked and mounted clinopyroxenes on double sided tape in a plastic cylinder and poured epoxy on the crystals, leaving them to set and creating an epoxy round. Polished rounds were then photographed to use as data acquisition maps. Scanning electron microscopy (SEM) was conducted at Portland State University on the Zeiss Sigma VP FEG SEM machine. Two plugs were analyzed, one I prepared and the other prepared by Shafer (2017). The SEM was utilized to obtain back scattered electron images and EDS data on accessory minerals within the clinopyroxenes of the Devine

Canyon Tuff. The compositions of these accessory minerals and investigation of the composition of group E glomerocrysts were obtained with the SEM.

Ti-in-Quartz – Temperature

Quartz phenocrysts (991–425 μm in size) previously separated from pumice groups A-E by Erik Shafer, were chosen. I laid quartz crystals on double sticky tape within a plastic cylinder, with particular care as to lay crystals perpendicular to the c-axis. Epoxy poured on the crystals sat over night to dry. We used photographed polished rounds as data acquisition maps. The variable pressure (VP) detector on the Portland State's Sigma Zeiss machine collected pictures of zoned quartz crystals, which reflect variations in titanium concentrations. Using the Cameca SX-100 electron microprobe at Oregon State University, remotely operated from Portland State University, we collected titanium and aluminum concentration data from the zoned quartz phenocrysts. Settings used during analysis: 100nA current; 15kV voltage and 5 μm beam diameter. The instrument collected titanium and aluminum with a 600 second peak count time and a background condition of 2x300 seconds. We analyzed fourteen crystals, groups A-D, with four spots per crystal moving from the core to rim. Group E was not analyzed, because of the glomerocrystic nature of the minerals and individual quartz were not found.

RESULTS

Distribution of Compositions

Within the Devine Canyon Tuff, the percent of crystals and the thickness of the ignimbrite decrease with distance from the proposed source in the Harney Basin (Greene, 1973). We sampled three outcrops from the stratigraphic base to the top. One of the outcrops (local 62) was targeted to tie a precursor fallout deposit to the overlying base of the ignimbrite. Each outcrop varied in distance from source, welding and crystallinity with respect to one another. Outcrop scale zoning characteristics with respect to trace elements and crystal percent are present in some but not others. One thick outcrop (local 66, **Table 2**), is crystal rich from base to top with compositions near the less enriched end

Figure 13. Photo of banded pumice within non-welded outcrop. Pumice was separated and analyzed bands are found in Appendix A, dark band – SI-16-60D and light band – SI-16-60L. Dark band is characterized as group D, while light band is group C.

of the compositional rhyolite array. However, in the second outcrop (local 8.1-10) crystallinity increased stratigraphically upward. This outcrop has a trace element enriched base and a more depleted top, largely corresponding with group A and D compositions, respectively, although the enriched base is not as enriched as group A (**Table 2**). The

base of the ignimbrite at local 62 record very evolved rhyolites (**Table 2**). Fallout pumices beneath the ignimbrite record group A rhyolite composition. The sample from the base of the ignimbrite yields a slightly less evolved composition than A indicating a mixture of the other rhyolite composition(s) in bulk tuff. Banded pumices collected and analyzed in this study reveal the juxtaposition of two discrete rhyolites, groups C and D, in a single pumice (**Figure 13**). Banded pumices reflect magma mixing or commingling of distinct rhyolite groups prior to eruption (i.e., **Figure 13** C & D mixed pumice). Finally, a crystal-rich and a crystal-poor fiamme sample located at the same stratigraphic level fall into the group D and group A rhyolite composition, respectively (local DC-4 sample, Appendix, and Shafer, 2017).

Table 2. Zirconium content (ppm) as observed in tuff samples across outcrops at different distances from source.

Outcrop Name	Zr (ppm)	Distance from source	Description
Outcrop 66 – Top of outcrop	735	< 20 km	Welded and devitrified middle section of ignimbrite, ~20 m thick
Outcrop 66 – Base of outcrop	611		Incipiently welded middle section of ignimbrite, ~20 m thick
Outcrop 8.1-10 – Top of outcrop	753	~ 30 km	Glassy, crystal rich top ~10 m thick
Outcrop 8.1-10 – Glassy base of ignimbrite	1312		Glassy, crystal poor, welded base. -10 m thick
Outcrop 62 – Base of ignimbrite	1418	~ 50 km	Non-welded base of the Ignimbrite, ~ 48 cm thick
Outcrop 62 – Fall out	1508		Fallout tephra, ~55 cm thick

Melt Inclusions- CO_2 and H_2O

Melt inclusions form when melt gets trapped during growth of a phenocryst, and is quenched to glass during eruption (**Figure 14**). Wallace et al. (1999) described several types of melt inclusions, all are observed in the DCT: 1) wholly enclosed inclusions within the crystal host (**Figure 14c, 14d**); 2) hourglass inclusions that are connected to the rim of crystal by a thin neck (**Figure 14a**) and 3) reentrants that are openly connected to the outside of the crystal (**Figure 14b**). The presence of gas bubbles reflects the exsolution of volatiles from the melt inclusion. In general, inclusions that are closer to the rim are taken to have been trapped later than inclusions found towards the center of the crystal (Wallace et al., 1999). After entrapment, wholly enclosed melt inclusions can only communicate with the coexisting melt by diffusion through the crystal (Wallace et al., 1999). Therefore, H_2O and CO_2 concentrations from wholly enclosed melt inclusions are the most representative of the preexisting melt (**Figure 14c**). A full list of CO_2 and H_2O concentrations and melt inclusions descriptions are found in Appendix C.

High silica rhyolite (75-77 wt.%) groups A through D contained quartz hosted melt inclusions sampled in this study. Group E could not be sampled due to the

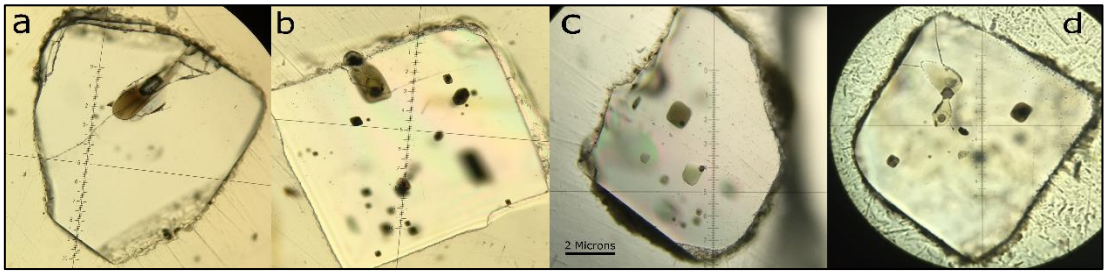

Figure 14. Binocular microscope photos of melt inclusions trapped within DCT quartz crystals. 14a) brown hourglass inclusion with a large vapor bubble; 14b) dark green open reentrant with vapor bubble; 14c) two wholly enclosed inclusions with vapor bubbles, one clear one brown in color and 14d) wholly enclosed clear inclusion with vapor bubble attached by a thin neck to another inclusion with a vapor bubble. Dark crystallized mineral inclusions in background of 14b, 14c and 14d.

glomerocrystic texture of the minerals present within the group. The quartz in group D shows signs of resorption, while groups B and C contain pristine, euhedral quartz with no

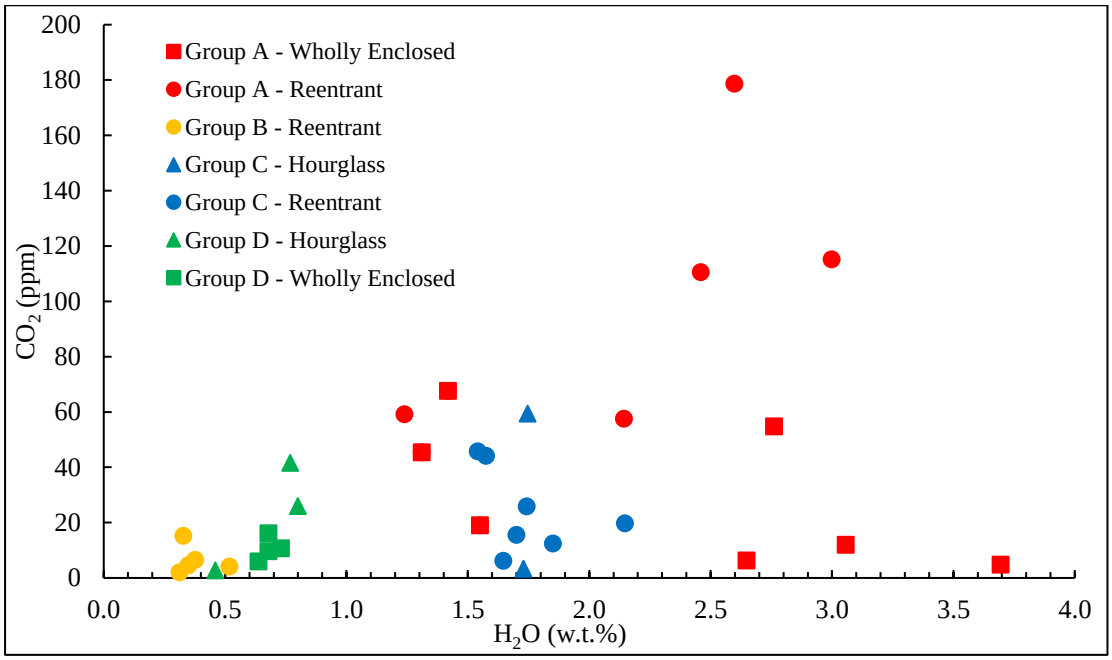

Figure 15. H_2O (wt.%) vs. CO_2 (ppm) from all melt inclusions within each rhyolite group (A-D). Group A has the greatest variable H_2O and CO_2 concentrations relative to all other groups. Melt inclusion type (wholly enclosed, reentrant or hourglass) are also denoted by different symbols.

signs of resorption. However, melt inclusions were sparse in group B possibly skewing the data collected. The greatest and most variable amount of H_2O (1.23 – 3.69 wt.%) occurs in group A. Group C has values greater than 1.5 wt.% but an overall smaller variability of 1.54 – 2.15 wt.% (**Figure 15**). Group B and D contain H_2O concentrations lower than 1 wt.% (0.31 – 0.80 wt.%). Reentrant melt inclusions analyzed from Groups B and D have low H_2O and CO_2 concentrations, due to volatile loss from the inclusion not being wholly encased in the host. A roofward increase in H_2O concentration is generally recognized in large-volume magma chambers, this may be reflected in the highest H_2O contents recorded in group A. Using the VolatileCalc software (Newman and Lowenstern, 2002) vapor saturation isobars derived at a temperature of 900^{o} C, estimated

from temperature derived using zircon thermometer (**Table 13**), are shown in **Figure 16**.

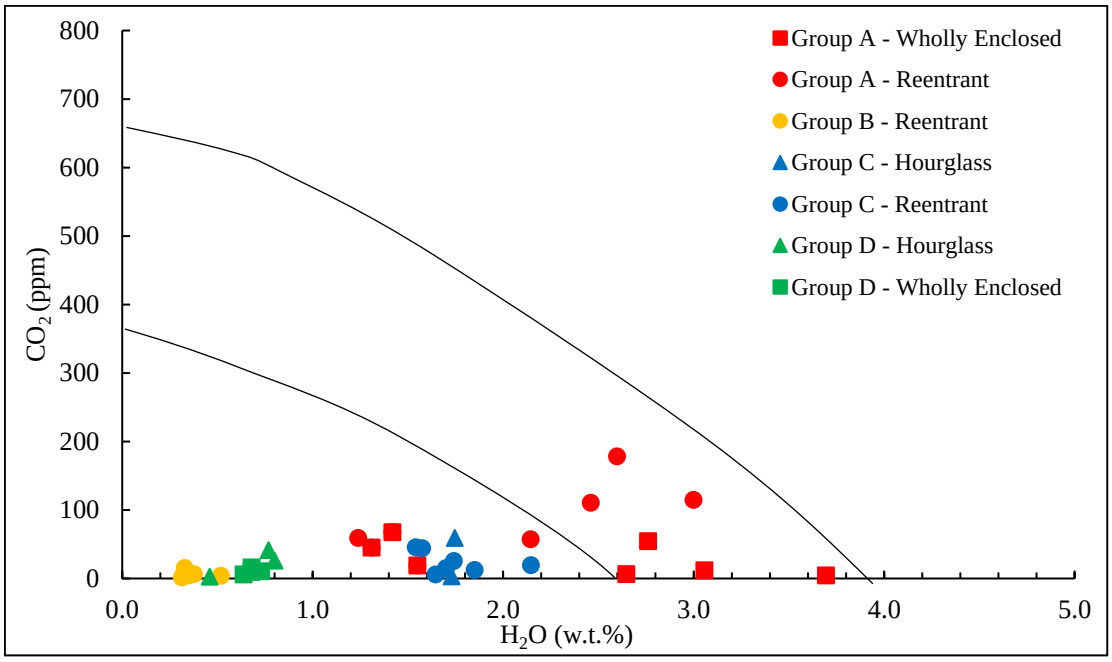

Figure 16. All high-silica rhyolite groups H2O vs. CO2. Isobars at 1 kbar and 500 bars are plotted from average temperature, calculated below, 900°C. The only group to record a pressure greater than 500 bars is group A.

Estimated pressure recorded in all high-silica rhyolites is less than 1,000 bars corresponding to a depth of less than ~3.5 km. Pressure estimates corresponding to depth of ~ less than 2 km are unrealisticly low suggesting either that rhyolites were undersaturated with respect to H_2O and CO_2 or that inclusions experienced a loss of volatile prior to eruption.

Stable Isotopes – $\delta^{18}O$

The $\delta^{18}O_{mineral}$ values collected from the high-silica rhyolites of the DCT are converted into $\delta^{18}O_{magma}$ that represent the $\delta^{18}O$ value of melt that the mineral crystallized from, using equations developed by Bindeman and Valley (2002, 2003). The MELTS program was used to determine how $\delta^{18}O$ changes relative to SiO_2, treating the melt (bulk rock) as a mixture of normative minerals (Bindeman, 2008b). The normative approach assumes

that all minerals in the melt have the same partition coefficient for the isotope distribution. This has been demonstrated to be a correct assumption for quartzo-feldspathic mixtures and is appropriate for this analysis (Bindeman, 2008; Matthews et al., 1998). The equations used are:

$$\text{Quartz: } \delta^{18}O_{magma} = \delta^{18}O_{qtz} - 0.45 \quad (4)$$

$$\text{Alkali Feldspar: } \delta^{18}O_{magma} = \delta^{18}O_{feldspar} + 0.29 \quad (5)$$

An important caveat to note is that the application of these equations or correction factors cannot be applied to crystals involved in magma mixing because the SiO_2 bulk rock content is not the same as the melt the minerals crystallized from (Bindeman et al., 2004). These equations provide a useful interpretation of $\delta^{18}O$ data by relating it to the preeruptive magma $\delta^{18}O$ value (**Table 3**).

Single and groups of quartz and feldspar crystals from each of the 5 DCT groups were analyzed for $^{18}O/^{16}O$ ratios. The $\delta^{18}O$ magma values calculated for the DCT, based on all quartz and alkali feldspar phenocrysts, have a maximum range of 1.5‰ from 4.52‰ to 5.76‰ (**Figure 17**). There are $\delta^{18}O$ magma variations within specific groups that exceed instrument error. For example, group B has $\delta^{18}O$ magma values ranging from 4.5 to 5.8‰ within individual feldspar crystals and group D has values ranging from 4.9 to 5.5‰.

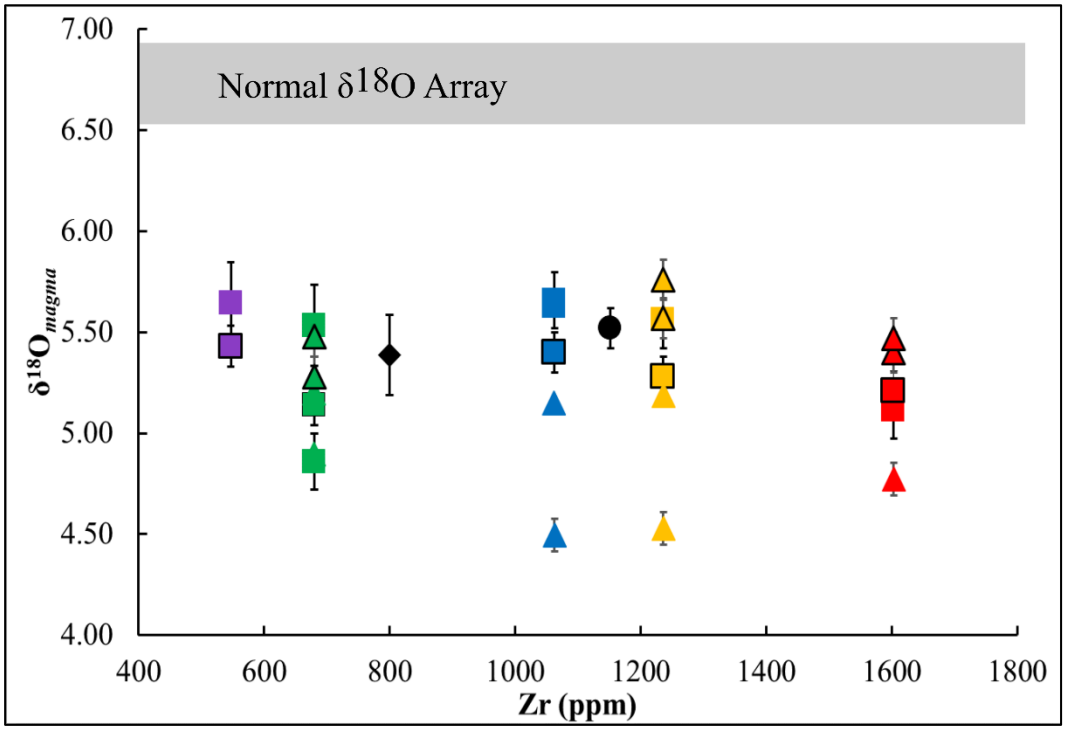

Figure 17. $\delta^{18}O$ Magma vs. Zr in ppm for compositional groups A – E in the DCT. Single quartz - black outlined triangles, bulk quartz - triangles, single feldspar - black outlined squares and bulk feldspar - squares. Errors bars vary between groups and phenocrysts due to different day analysis. Group A -red, group B- orange, group C – blue, group D - green, group E – purple. Bulk sanidine analysis – black diamond (Hess, 2014) and black circle (data from M.T. Ford).

Table 3. Analyzed $\delta^{18}O_{Quartz}$, $\delta^{18}O_{Feldspar}$, and calculated $\delta^{18}O_{magma}$ values from quartz and alkali feldspar phenocrysts. Multiple pumice samples used for one group indicated by multiple Sample IDs. Analysis column indicates if the values came from single crystal analysis or bulk crystal analysis.

Group	Sample ID	^{18}O SMOW	^{18}O Magma	Analysis	Uncertainty ±
		Quartz			
Group A	DC11_1P	5.223	4.773	Bulk	0.08
	SI-16-62a	5.850	5.400	Single	0.1
	SI-16-62a	5.920	5.470	Single	0.1
Group B	DC11_33P8	4.978	4.528	Bulk	0.08
		5.635	5.185	Bulk	0.01
		6.020	5.570	Single	0.1
		6.210	5.760	Single	0.1
Group C	MS10-28-DCA	4.945	4.495	Bulk	0.08
		5.599	5.149	Bulk	0.01
Group D	DC11_33P7	5.648	5.198	Bulk	0.08
		5.346	4.896	Bulk	0.01
		5.93	5.48	Single	0.1
		5.73	5.28	Single	0.1
		Feldspar			
Group A	DC11_1P	4.824	5.114	Single	0.14
		4.920	5.210	Bulk	0.1
Group B	DC11_33P8	5.272	5.562	Single	0.14
		4.990	5.280	Bulk	0.1
Group C	MS10-28-DCA	5.110	5.400	Bulk	0.1
		5.336	5.626	Single	0.14
		5.368	5.658	Single	0.2
Group D	DC11_33P7	4.569	4.859	Single	0.14
		5.244	5.534	Single	0.2
		4.850	5.140	Bulk	0.1
Group E	DC11_P11	5.355	5.645	Single	0.2
		5.140	5.430	Bulk	0.1

Accessory Phases

Accessory phases of variable composition are commonly found in or adhering to mafic minerals, such as hedenbergite (Michael, 1988). Diverse accessory minerals, some containing REE, are present in the all pumice groups A through E (**Table 4**). Appendix B contains all accessory mineral compositional data from this study.

Table 4. Summary table of accessory phases found in each group, "x" in the row under the mineral indicates the presence of the mineral in the group.

Group	Chevkinite	Apatite	Ti-magnetite	Ilmenite	Zircon	Pyrite
A	x	x		x	x	x
B	x	x		x		
C	x	x	x	x		x
D	x	x		x	x	x
E	x		x	x		x

Chevkinite, ilmenite, zircon, apatite, titanomagnetite, and pyrite are accessory phases identified and reported in this study. The minerals chevkinite and Fe-Ti oxide occur in all groups, A – E. Apatite was only found in high-silica rhyolite groups, A through D. Pyrite occurs in all groups, except for group B. Groups A and D also contain zircon.

Chevkinite, a light rare earth element rich silicate is dominantly found in rhyolites, syenites and fenites (Macdonald and Belkin, 2002). La, Ce, Pm, Nd, and Sm., i.e. LREE's, are the primary cations incorporated into chevkinite, beside Si, Ti, and Fe. The progressive depletion reflected in LREE patterns from high-silica rhyolite group D to A is consistent with removal of chevkinite (**Table 5 and Figure 5**).

Table 5. Average composition of chevkinite per each group, normalized weight %.

	Grp A	±1σ	Grp B	±1σ	Grp C	±1σ	Grp D	±1σ	Grp E	±1σ
Na_2O	0.3	0.1	0.9	0.0	0.3	0.0	0.3	0.0	0.0	0.0
Al_2O_3	0.3	0.3	0.3	0.0	0.2	0.0	0.3	0.2	0.3	0.1
SiO_2	20.8	4.1	18.2	2.3	19.9	0.3	18.5	1.5	17.2	0.7
P_2O_5	0.1	0.1	0.1	0.1	0.1	0.1	0.1	0.1	0.1	0.1
CaO	3.3	2.1	3.2	0.3	3.0	0.2	3.0	0.3	3.2	0.3
TiO_2	19.1	2.5	20.1	1.0	19.3	0.2	20.1	0.6	20.8	0.4
MnO	0.2	0.2	0.0	0.0	0.2	0.1	0.2	0.1	0.0	0.0
FeO	11.4	2.5	11.4	0.7	11.5	0.4	11.1	0.4	10.8	0.4
Y_2O_3	1.0	0.0	0.0	0.0	0.0	0.0	0.7	0.0	0.0	0.0
Nb_2O_5	0.6	0.0	0.7	0.0	0.0	0.0	0.6	0.0	0.3	0.2
La_2O_3	12.1	1.7	13.2	1.1	12.8	0.6	12.9	0.7	13.2	0.6
CeO_2	21.6	2.9	22.6	0.8	22.0	0.3	22.5	0.6	22.9	0.5
Pr_2O_3	1.9	0.4	2.0	0.4	2.0	0.2	2.1	0.3	2.2	0.3
Nd_2O_3	7.7	1.0	7.6	0.6	7.7	0.3	7.9	0.4	7.8	0.4
Sm_2O_3	1.1	0.2	1.1	0.4	0.9	0.2	1.1	0.3	1.0	0.3
Eu_2O_3	0.3	0.2	0.5	0.3	0.0	0.0	0.3	0.3	0.2	0.2

Fe-Ti oxides, found in all groups, appear as three different mineral phases (**Table 6).** Ilmenite is the most common Fe-Ti oxide phase occurring in all groups. Titanomagnetite occurrs in group C and E. Hematite is only in group A, and is likely xenocrystic or a product of post-emplacement oxidation (**Table 7**).

Table 6. Average Ilmenite composition for all groups, normalized weight %. All Fe calculated as Fe^{3+}.

	Group A	Group B	Group C	Group D	Group E
SiO_2	0.1	0.0	0.8	0.1	0.1
TiO_2	52.2	52.3	50.7	51.5	52.9
Al_2O_3	0.1	0.0	0.1	0.0	0.0
Fe_2O_3	45.8	45.5	46.5	45.7	44.8
MnO	1.5	1.7	1.5	1.5	1.6
MgO	0.0	0.0	0.0	0.0	0.0

Table 7. Average Fe-Ti oxide mineral, with differing composition from ilmenite, found in groups A, C and E. Mineral indicates the hypothesized oxide mineral, normalized weight %. All Fe calculated as Fe^{3+}

Mineral	Ti-magnetite	Ti-magnetite	Hematite
	Group C	Group E	Group A
SiO_2	0.8	0.0	1.1
TiO_2	21.2	27.7	0.0
Al_2O_3	1.5	0.4	0.2
Fe_2O_3	73.2	70.5	95.4
MnO	0.4	1.4	1.6
MgO	2.7	0.0	0.2

Zircon appears to occur only in groups A and D (**Table 8**). We infer that zircon is also present in groups B and C rhyolites, but have not been identified.

Table 8. Average zircon composition for groups A and D, normalized weight %.

	Group A	Group D
SiO_2	22.27	23.06
Fe_2O_3	0.00	0.29
ZrO_2	76.75	75.77
HfO_2	0.98	0.84

Apatite occurs only in the high-silica rhyolite groups (**Table 9**). Fractional crystallization of intermediate compositions towards felsic compositions saturate the system with apatite, and subsequently deplete the melt in REE (Watson and Capobianco, 1981). All apatite in the high-silica rhyolite groups contain varying amounts of REE. It is inferred that the lack of apatite in group E is not from sampling bias and the group does not contain apatite.

Table 9. Average apatite compositions for high-silica rhyolite groups, normalized weight %.

	Group A	Group B	Group C	Group D
SiO_2	7.2	5.7	6.5	4.0
Al_2O_3	0.1	0.0	0.0	0.0
Fe_2O_3	0.9	0.0	0.5	0.9
MnO	0.0	0.0	0.0	0.0
MgO	0.0	0.0	0.0	0.0
CaO	46.1	44.6	45.3	48.0
Na_2O	0.4	0.1	0.2	0.2
P_2O_5	34.0	30.6	32.3	34.5
SO_2	0.0	0.0	0.0	0.0
NiO	0.0	0.0	0.0	0.0
Y_2O_3	0.0	0.0	0.0	1.0
La_2O_3	2.1	1.0	1.6	1.2
CeO_2	5.1	2.9	4.0	3.3
Pr_2O_3	0.3	2.2	1.2	1.9
Nd_2O_3	3.1	5.7	4.4	2.0
Pm_2O_3	0.0	0.9	0.4	0.9
Sm_2O_3	0.0	3.6	1.8	0.3
Gd_2O_3	0.0	0.8	0.4	0.2
Dy_2O_3	0.0	0.2	0.1	0.2
Ta_2O_5	0.0	0.4	0.2	0.0

Pyrite is found in all groups, high-silica rhyolite and dacite, except for group C (**Table 10**). We infer that pyrite also occurs in group C. The presence of pyrite in group A indicates that the hematite identified there is in fact a secondary phase, as pyrite indicates reducing, low oxygen fugacity that would not lead to forming hematite.

Table 10. **Average pyrite composition for all groups, except group C, normalized weight %**.

	Group A	Group B	Group D	Group E
Si	0.33	0.24	0.14	0.00
Fe	46.79	47.95	47.29	44.75
Ca	0.30	0.23	0.18	0.00
P	0.18	0.07	0.03	0.06
S	51.85	51.17	51.86	53.73

Temperature – Cathodoluminescence (CL) & LA-ICP-MS

Electron Microprobe (EMP) analysis yielded titanium concentrations within zoned quartz phenocrysts from the high-silica rhyolite groups, A to D. Due to the glomerocrystic texture and lack of quartz in group E individual quartz crystals could not be analyzed Average inner core Ti values range from 40-66 (ppm) and outer rim concentrations yield greater values ranging from 100-140 (ppm) (**Table 11**).

Table 11. Average titanium concentration from the four zones analyzed on the crystal, inner core to outer core.

Group	Avg. Ti (ppm)	Std (σ)	Crystal Location
A	80	0.0	Inner Core
B	49	17.9	Inner Core
C	83	9.7	Inner Core
D	55	5.2	Inner Core
A	66	27.7	Outer Core
B	55	20.1	Outer Core
C	40	7.5	Outer Core
D	57	2.1	Outer Core
A	80	53.0	Inner Rim
B	82	13.1	Inner Rim
C	96	9.7	Inner Rim
D	99	22.9	Inner Rim
A	98	15.6	Outer Rim
B	86	20.2	Outer Rim
C	97	6.6	Outer Rim
D	98	17.9	Outer Rim

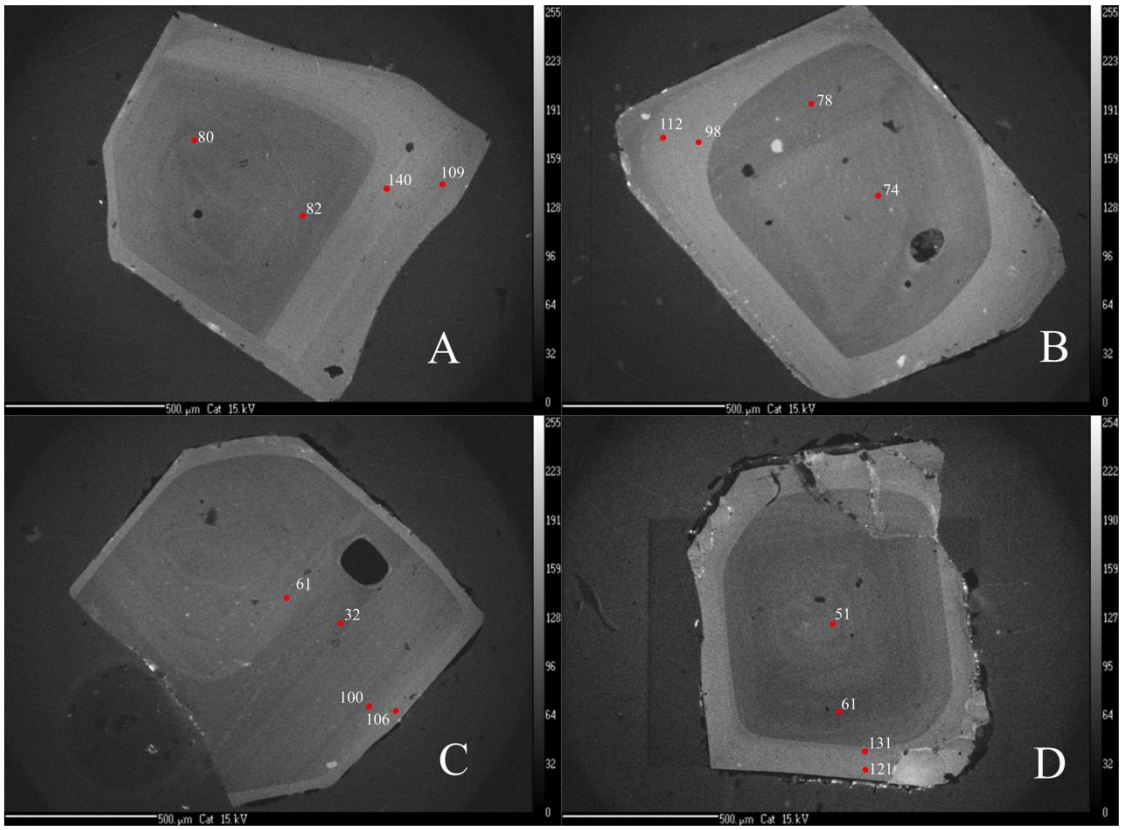

Figure 18. CL images of quartz phenocrysts from high-silica rhyolites, labeled A-D. Numbers are Ti concentrations, in ppm. Dark core of crystals B and C are subhedral with bright rims anhedral-euhedral in shape. Dark cores of A and D are more anhedral than B and C with euhedral bright rims. All phenocrysts have oscillatory zonations within the dark core, but bright cores are similar in width and shape. Red dots indicate EMP analysis spots.

Cathodoluminescence (CL) images of quartz phenocrysts revealed oscillatory internal zonations, with analogous bright rims of similar shape and width in all high-silica rhyolite groups (**Figure 18**). Thermal histories and crystallization temperatures can be evaluated in silicic magmas through a systematic correlation with temperature and Ti content in quartz (Leeman et al., 2012). Wark and Waston (2006) empirically derived Equation (6), calculating the temperature of formation of a quartz crystal in a rutile-free melt. Temperature is in Celsius (C°) and X_{Ti}^{qtz} is the concentration of Ti (ppm) and a_{TiO_2} is the activity of TiO_2 in the melt;

$$\mathrm{T\ (C°)} = \frac{-3765}{\log\left(\frac{x_{Ti}^{qtz}}{a_{TiO_2}}\right) - 5.69} - 273 \qquad (6)$$

The derivation of the activity of TiO_2 in the melt is fundamental when applying Equation (6) to a rutile-free melt, like that of the DCT (Watson et al., 2006; Leeman et al., 2012; Wilson et al., 2012). A separate thermometer is commonly utilized to derive the activity of TiO_2, this approach is also used with the DCT. Zircon saturation thermometry provides useful estimates of temperature. If magma is undersaturated in zirconium the thermometer yields a minimum estimate of temperature, when magma is saturated in zirconium it provides a maximum estimate of temperature. The presence of zircon in groups A and D suggests the DCT was saturated with respect to Zr and allows for a discrete calculation of temperature with a zircon thermometer. However, the low abundance of zircon and the strong incompatible behavior of Zr from least to most evolved rhyolite probably suggest local Zr saturation near mafic phenocyrsts. This in turn may suggest that derived Zr saturation temperatures may or may not reflect true magma temperature. Rearranging Equation (7) and solving for temperature (Watson and Harrison, 1983).

$$\ln D_{Zr}^{zircon/melt} = \{-3.80 - [0.85(M-1)]\} + 12900/T \qquad (7)$$

$$M = \frac{Na+K+2Ca}{Al*Si} \qquad (8)$$

In Equation (7) D represents the concentration ratio of Zr in the stoichiometric zircon to the melt, T is the absolute temperature, and M is the cation ratio (Na + K + 2Ca/Al*Si). The derived temperature for group A is 1014 C° and for D is 904 C°. Temperature values derived from group A appear to be very high and may be incorrect. Thus, applying the

derived temperature, from group D, to Equation (6) and solving for the a_{TiO_2} yields a range in values from 0.15-0.27, with an average value of 0.20. The average a_{TiO_2} value of 0.20 is used in Equation (6) to derive temperatures of formation from Ti content fluctuations in quartz zonations (**Table 12**). If the activity of Ti can be estimated within ± 0.1 the calculated temperature can be off by no more than ± 20°C (Wark and Watson., 2006). Analysis points that yielded the highest temperatures are located in the inner and outer rim with lower temperatures being concentrated in the core. The highest core temperature is found in group A (~950° C), and all other high-silica rhyolite groups core temperatures indicate temperature value, roughly ~80° or less. All groups converge in temperatures when comparing the outer rim of the quartz crystals (**Figure 19**). This observation indicates the influx of hotter magma, which affected all rhyolite magmas to the same degree within a contiguous magma chamber.

Table 12. Average temperature derived for all high-silica rhyolites from equation 3, using a activity of TiO_2 = 0.20. Note the change in temperature as you move from the core to the outer rim seen in all groups.

	Core	Std σ	Core to Rim	Std σ	Inner Rim	Std σ	Outer Rim	Std σ
Group A	946.3	0.0	900.0	52.8	897.8	29.9	980.3	14.3
Group B	861.7	81.8	876.5	61.6	949.6	27.2	954.7	5.5
Group C	876.4	158.0	834.2	27.8	978.3	18.7	979.3	40.4
Group D	883.8	30.3	895.2	41.0	980.1	12.3	978.1	32.9

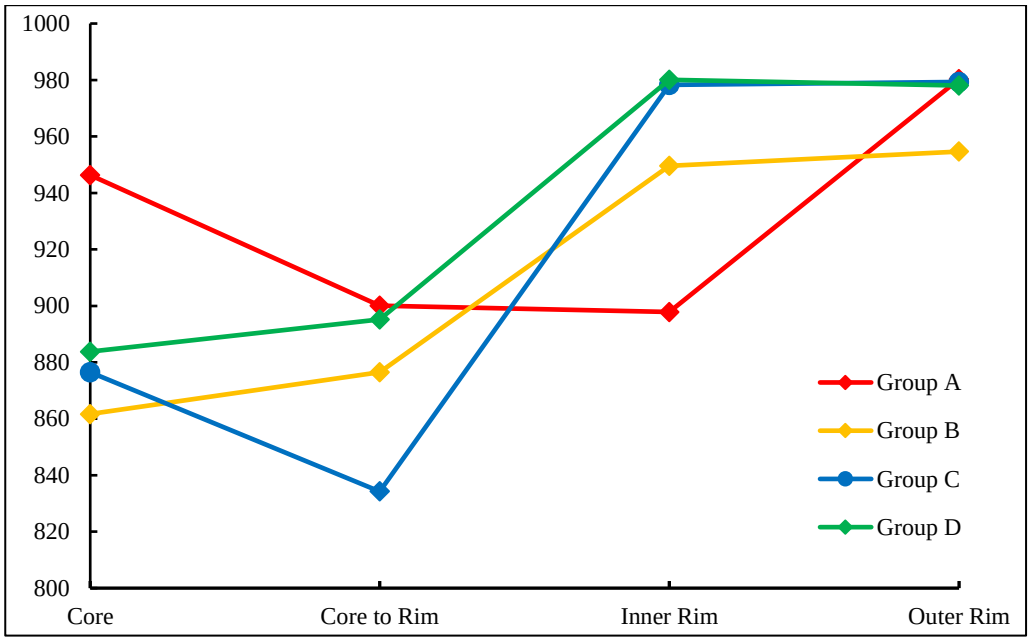

Figure 19. Average calculated temperatures at four locations on quartz phenocrysts, moving from the core outward to the rim. Temperature derived using a_{TiO2} = 0.20. Note similar core temperatures for groups B, C and D. All crystals converge at ~980° towards the outer rim.

DISCUSSION

The Devine Canyon Tuff exhibits compositional, crystallinity, and volatile gradients across rhyolite magmas. Feldspar and quartz phenocrysts in all groups, A – E, record variable and low $\delta^{18}O_{magma}$ values. Decreasing crystallinity accompanies progressive enrichment of incompatible trace elements, e.g., increase in Zr ~500 to 1600 ppm, from the least evolved (group E) to most evolved (group A) magmas. Mingling is apparent between the high silica rhyolite groups, A to D, and dacitic magmas recorded in discrete dacitic or banded pumices. Observed lithological and geochemical features of the erupted DCT magmas are outlined in **Table 13** and require explanation in any magma evolution model.

Table 13. Summary of all observations to be reconciled in magmatic evolution model for the DCT.

1. Some pumices exhibit mingling within high-silica rhyolite magmas and with dacite magmas
2. Decrease in crystallinity from least to most evolved rhyolite
3. Greater than two-fold increase in incompatible trace elements from least to most evolved rhyolite
4. Highest water content concentrated in group A
5. Compositional tight range for sanidine of all rhyolites, sanidine of dacites overlap with those of rhyolite but trend away to higher albite content
6. Greater decrease of En % displayed in groups B, C and E
7. Low (<7) and variable delta $\delta^{18}O_{magma}$ value for all groups
8. Ti-rich rim on quartz phenocrysts from all high silica rhyolites (increase related to late temperature increase)

Proximity of rhyolite magmas

Two explanations are commonly used to explain the compositional zonation in ignimbrites; 1) a single reservoir that is zoned with respect to chemical composition, volatile content and crystallinity (Hildreth, 2004), or 2) separate and distinct reservoirs housing independent magmas, either as melt lenses held within a rigid network of mushy material or multiple reservoirs of magma that are not interconnected (Ellis et al., 2010,

2014). Magmas stored in adjacent, but separate reservoirs can have distinct identities as expressed by chemical composition, mineral assemblages and volatile contents even though they have originated through similar petrogenetic steps. Separate batches of magma can mix during explosive eruptions to create the chemical zonation observed in the emplaced ignimbrites. If magmas from shallow and horizontally separated reservoirs can erupt from a shared conduit where they may also mix is doubtful.

Data of the DCT provide evidence for invoking a single, contiguous magma reservoir rather than multiple reservoirs. As discussed in Shafer (2017), the DCT exhibits considerable compositional overlap when comparing major elements of bulk tuff, bulk pumice and individual phenocrysts. Greene (1973) described the DCT as a single flow unit. The results presented here show that discrete fiamme of group A and D compositions are found in the same tuff horizon. Furthermore, group C and D compositions found within a single banded pumice suggest mingling between rhyolite groups. There are abundant banded pumices indicating mingling of the rhyolites prior to eruption within conduits or the reservoir of a contiguous magma body. The major phases, alkali feldspar and clinopyroxene, are indistinguishable among the high-silica rhyolites. In contrast, the major phases in the dacite magma have a greater range in major and trace elements than in rhyolites, but slightly overlap with compositions of the rhyolite groups. Similarities in mineral assemblages imply that all rhyolites crystallized under the same conditions and the presence of banded pumices suggest these magmas resided in a single magma reservoir. And finally, quartz zoning indicates that a late thermal overprint affected all high-silica rhyolite magmas. This effectively excludes the possibility of

multiple reservoirs that only mingled sub-aerially during eruption (Ellis et al., 2010; Ellis et al., 2014). Instead, I argue for a pre-eruptive contiguous magma reservoir that underwent a multitude of processes, including magma mixing and fractional crystallization to generate the compositional zonation expressed in the ignimbrite.

Role of Magma Mixing

The mixing of end-member magmas of varying density and composition is an important process to produce diversity in magmas (Eichelberger, 1975; Anderson, 1976). Driven by convection, discrete magmas with differing compositions and densities can stir and mingle. If density and thermal gradients are great enough, a chamber overturn can initiate (Sparks et al., 1984). Furthermore, injection or underplating of a basic hot magma can initiate convection at the base of a magma chamber causing a large thermal gradient.

The Devine Canyon Tuff exhibits mingling between high-silica rhyolite groups as recorded by banded pumices. Magma mixing may not only be an important process that leads to mingling of magmas during final ascent, but possibly to the diversity within the high-silica rhyolites. Below we evaluate whether intermediate rhyolite members (composition B and C) could be explained by mixing of end-member rhyolites (composition A and D) using a binary mixing equation. Samples chosen for all mixing models are highlighted in **Figure 20**. The simple mixing equation was rearranged to solve for the mixing proportion of one of the two end-member rhyolites (Equation 9). M is the concentration of the resulting mixture, x is the proportion of the end-member rhyolite denoted by a in the mixture and a and b are the concentrations of the two end-member rhyolites mixed.

$$x = \frac{M - b}{a - b} \qquad (9)$$

To evaluate the fit of both models the relative standard deviation (RSD) was calculated (Equation 10). Summary of all models and a, b and M inputs into Equation (9) in **Table 14**.

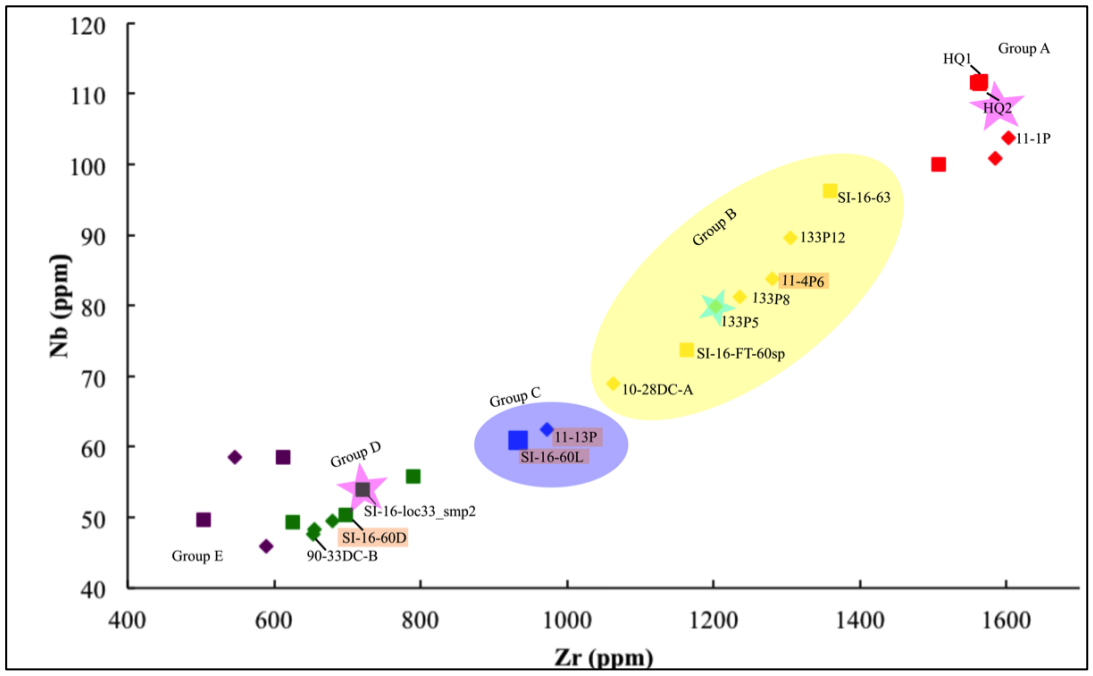

Figure 20. Zr vs. Nb (ppm) pumice (c.f., Figure 4). Pink star indicates end-member rhyolite, group A and D, values used in all eight mixing models (21a-24f) to generate all eight group B pumices (yellow shaded region). Single group B pumice with turquoise star is used in 25a and 25b mixing models to compare results of using different A and D end-members for generating the same B rhyolite. Sample highlighted by pink star were also used in mixing models 26a and 26b to generate C pumices. Samples highlighted by orange (mixing models 27a and 27b) indicate intermediate rhyolite, group B, mixed with end-member rhyolite, group D, to generate both group C pumices (blue shaded region with highlighted sample ID).

$$RSD = \left(\frac{standard\ deviation}{mean}\right) * 100 \qquad (10)$$

The model would yield a flat line if the same proportion of mixing were needed for all elements. Eight mixing scenarios were modeled where the end-member rhyolite

values chosen for *a* and *b* (Equation 9) remained the same, but values for *M* changed with each model, in this case all compositions of B pumices (**Figures 21, 22, 23 & 24**).

Table 14. Summary of all mixing models. Mixing Model number corresponds to Figure numbers and *a, b* and *M* values indicate pumice concentrations used in Equation 9. Zr vs. Nb sample concentrations (Group - Sample ID) are shown in Figure 20.

Mixing Model (Figure number)	*a*	*b*	*M*
21a	Group A - HQ2	Group D - SI-116-loc33_smp2	Group B - 11-4P6
21b	Group A - HQ2	Group D - SI-116-loc33_smp2	Group B - 133P5
22c	Group A - HQ2	Group D - SI-116-loc33_smp2	Group B - 133P12
22d	Group A - HQ2	Group D - SI-116-loc33_smp2	Group B - 133P8
23e	Group A - HQ2	Group D - SI-116-loc33_smp2	Group B - 10-28-DC-A
23f	Group A - HQ2	Group D - SI-116-loc33_smp2	Group B - SI-16-FT-60sp
24g	Group A - HQ2	Group D - SI-116-loc33_smp2	Group B - SI-16-63
24h	Group A - HQ2	Group D - SI-116-loc33_smp2	Group B - Average B
25a	Group A - HQ2	Group D - SI-116-loc33_smp2	Group B - 133P5
25b	Group A - 11-1P	Group D - 90-33DC-B	Group B - 133P5
26a	Group A - HQ2	Group D - SI-116-loc33_smp2	Group C - 11-13P
26b	Group A - HQ2	Group D - SI-116-loc33_smp2	Group C - SI-16-60L
27a	Group B - 11-4P6	Group D - SI-16-60D	Group C - SI-16-60L
27b	Group B - 11-4P6	Group D - SI-16-60D	Group C - 11-13P

In general, the mixing proportions of A and D to generate B yield RSD values of 18 to 40%. Ten to 15 of the trace elements evaluated produce consistent mixing proportions of end-member group A ranging from 40% to 72% with low RSDs. When all elements are considered, high RSD values are mainly caused by the Light Rare Earth

Elements Nd, Pr, La and Ce and Ba ± Eu. These require higher proportion of end-member group A than most elements to satisfy the mixing equation while a smaller number of elements, Sm, Sr, Gd, ±Eu, require lower proportions of group A. Some elements do not yield a valid mixing solution where values of x are greater than 1 or lower than 0. More specifically, in all models (21a through 24h), Sm requires a lower mixing proportion relative to the calculated average for each group. Mixing calculations to reproduce all group B pumices display similar trends despite requiring variable proportions of end-member group A.

To further investigate the generation of group B compositions, two mixing scenarios were calculated where the value chosen for *M* was kept constant for each scenario, but the end member rhyolites chosen for *a* and *b,* varied between each scenario. In other words, two different A pumice and D pumice compositions were used to generate the same B pumice composition. In both mixing scenarios (**Figure 25a & 25b**) Sm and Pb require significantly lower proportions than average or yield negative values (i.e. violate mixing). However, Ba, Eu, Sr, La, Ce, Pr, Nd, require higher proportions of group A.

The generation of group C through the mixing of end-member rhyolites, A and D, was also modeled (**Figure 26**) using the same A and D compositions as 21a-24h models. Alike the models of group B, LREE require higher mixing proportions of group A composition and Sm lower values than most elements that yield a fairly consistent proportion. Contrary to group B models, Rb, Hf, Zr, and Sr now also require higher mixing proportion of the group A composition relative to the average. The resulting RSD

values for model 26a is 146.5% and 26b is 120.9%, far larger than any group B models. The poor fit and very high RSD values for both models eliminate mixing of A and D compositions to yield C compositions as viable scenario.

Thus, another attempt was undertaken to generate group C compositions by mixing but now using group B as the more evolved end-member, instead of group A (**Figure 27**). In these calculations, the RSD values from both mixing scenarios (**Figure 27a and 27b**) were not as high as the models of 26a and 26b. However, in both models, Sm does not yield a valid solution, and Gd requires less of the evolved end-member. The LREE (Ce, La, Pr, and Nd) again require higher proportions of the evolved mixing member, in some instances values outside a valid solution ($x \geq 1$). In mixing model 27a, Zr and Rb are also in the group of the LREE requiring higher proportion of B composition. Sr is not shown because it cannot be explained by this mixing. The majority of elements still yield almost the same mixing proportion in either model (27a or 27b).

In summary, mixing group A and D composition to make B composition is consistent with a majority of trace elements, however a group of elements consistently require either higher or lower proportions or fall outside a valid solution. The generation of C compositions from mixing of A and D is unlikely and it would be better explained by mixing B and D compositions. In these models, the same subset of elements yields higher, lower, or invalid proportions of the *a* mixing member. Some misfit may be explained by nearly the same trace element concentration across the rhyolite spectrum. For example, Sm concentrations are nearly the same in all rhyolites and thus tiny deviations, which may in part be analytical, can produce a misfit (**c.f., Fig. 5**). Overall,

mixing alone cannot account for the generation of rhyolites B and C but require compositional modifications, by concomitant fractional crystallization.

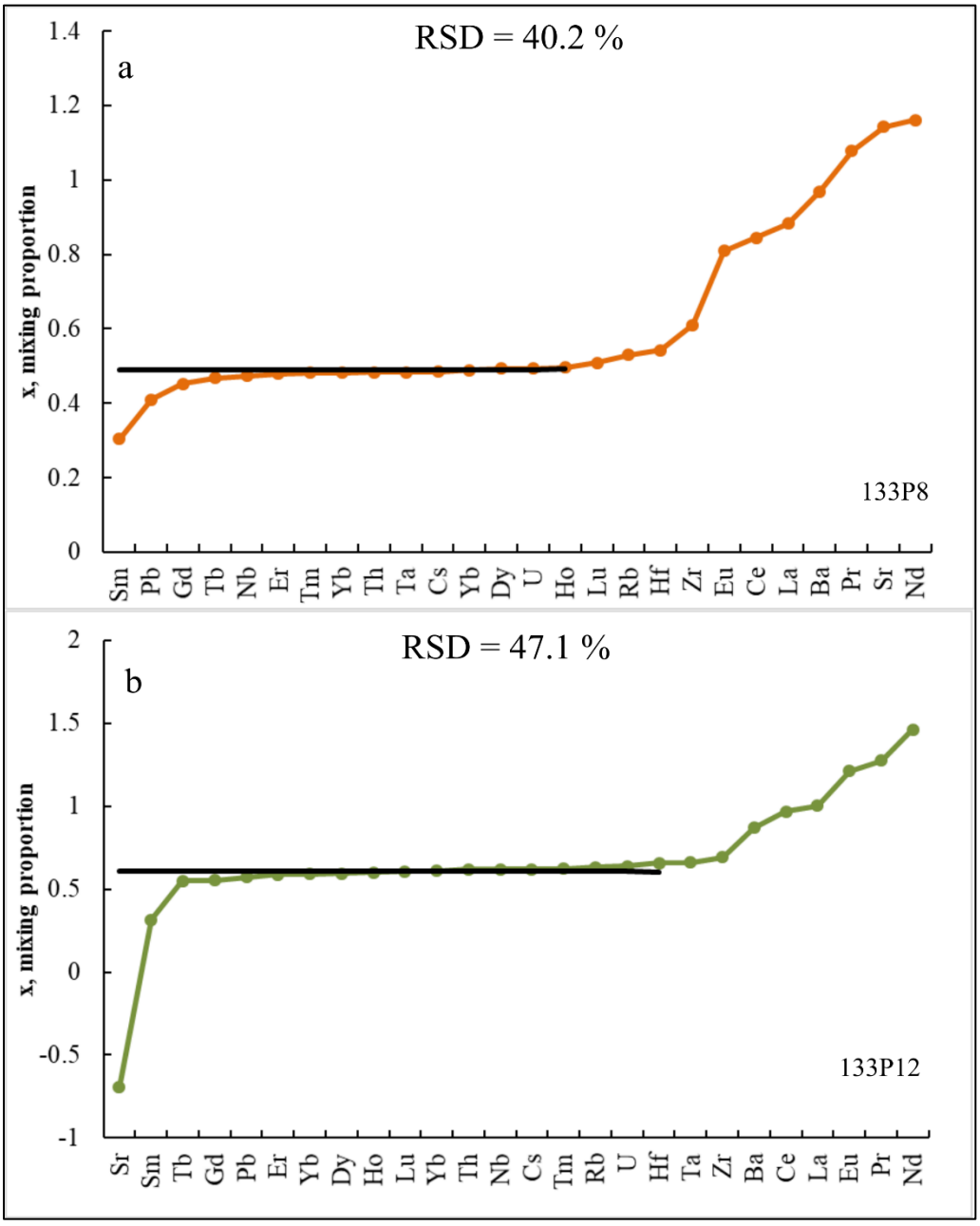

Figure 21. Mixing models using end-member group A (HQ2) and D (SI-16-loc33_smp2) values for *a* and *b* in equation 9 but different M values in a) and b). Sample ID in bottom right corner indicates B pumice used for M values (see text). General negative mixing proportions calculated for Sm, Sr and Pb in all models. Higher than average mixing proportions for *a* component observed in LREE and Eu, Zr and Ba. The average (horizontal line) is calculated from values that are nearly the same, i.e., 21a average derived from values of Tb through Hf.

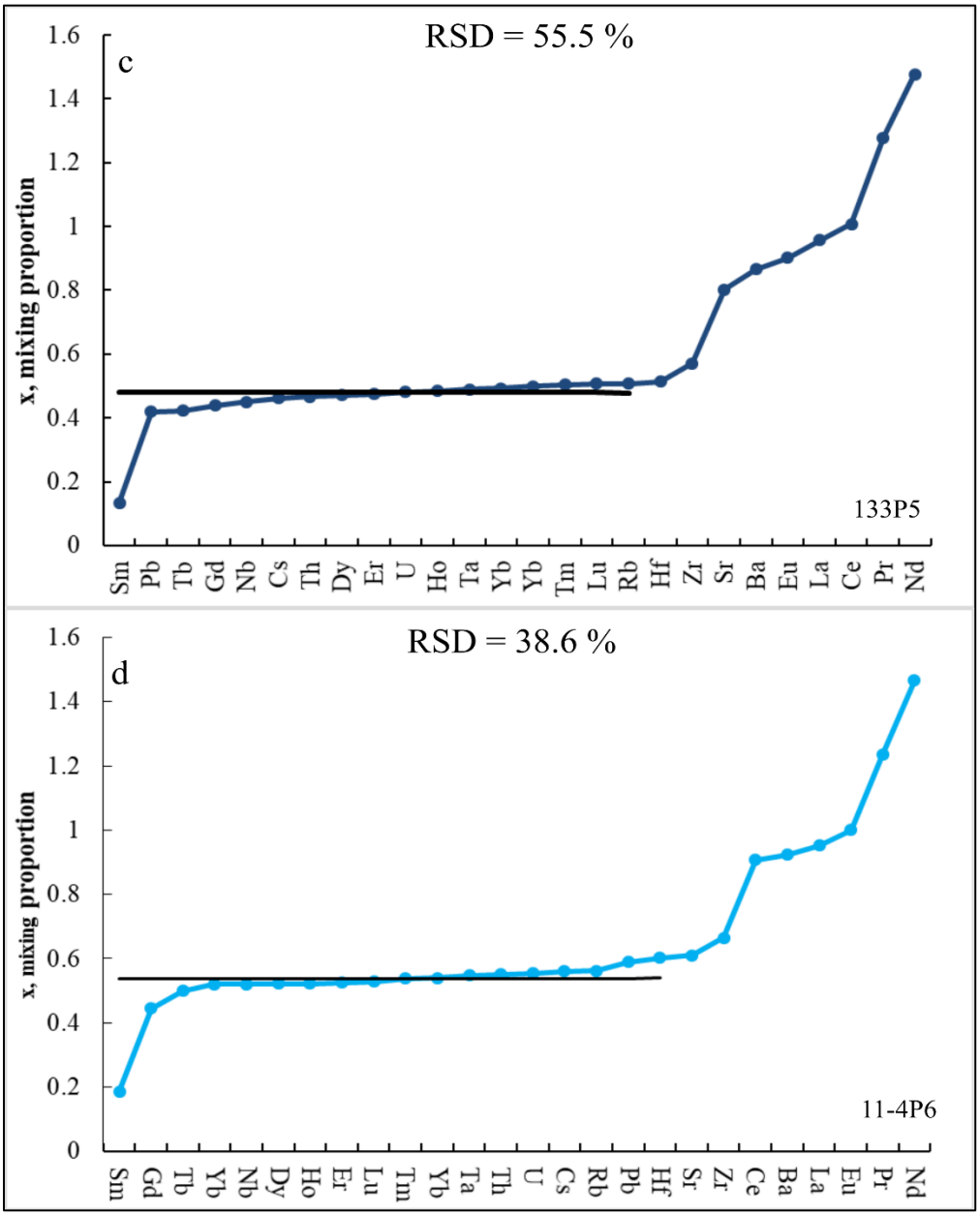

Figure 22. Mixing models using end-member group A (HQ2) and D (SI-16-loc33_smp2) values for *a* and *b* in equation 9 but different M values in c) and d). Sample ID in bottom right corner indicates B pumice used for M values (see text). General negative mixing proportions calculated for Sm, Sr and Pb in all models. Higher than average mixing proportions for *a* component observed in LREE and Eu, Zr and Ba.

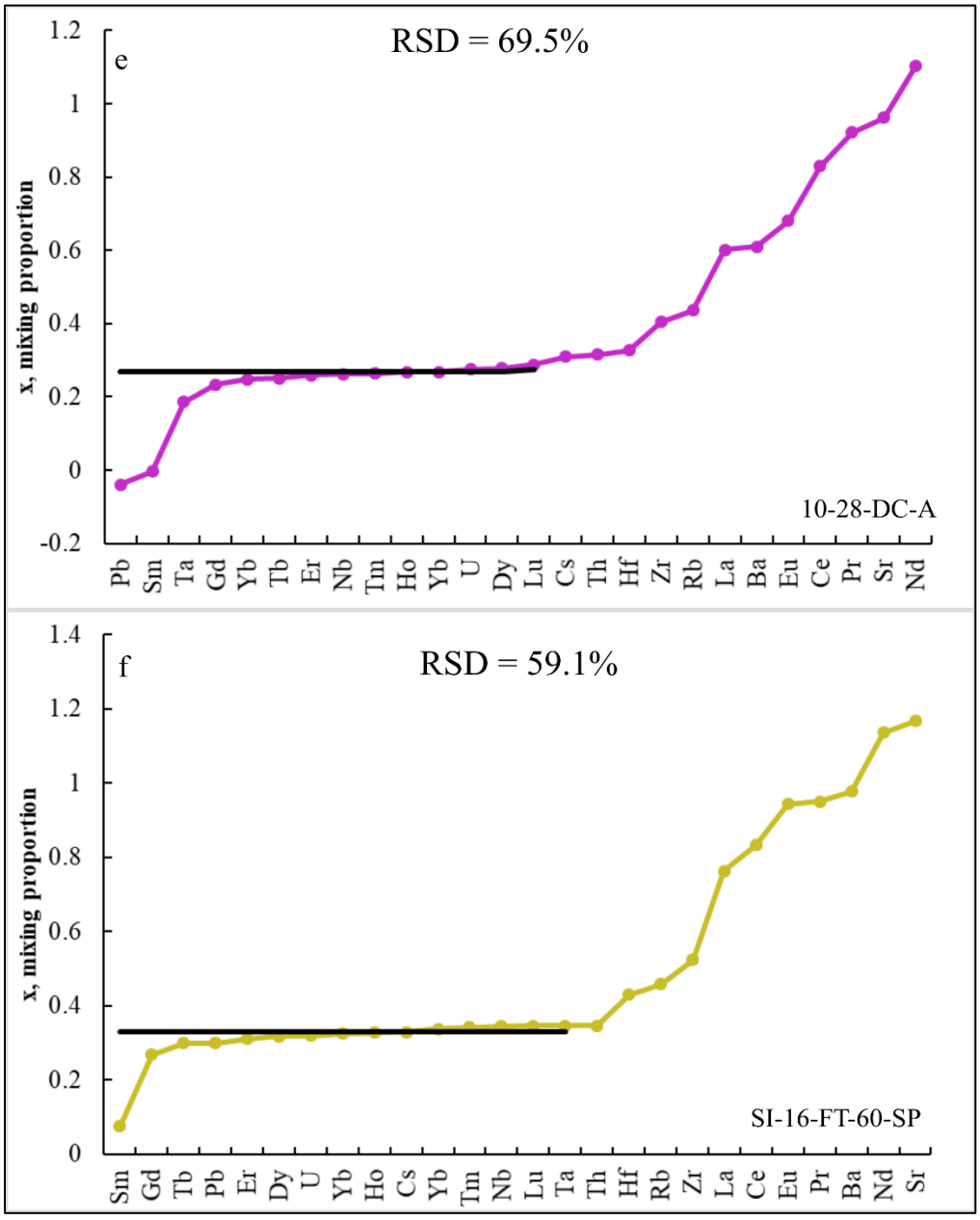

Figure 23. Mixing models using end-member group A (HQ2) and D (SI-16-loc33_smp2) values for *a* and *b* in equation 9 but different M values in e) and f). Sample ID in bottom right corner indicates B pumice used for M values (see text). General negative mixing proportions calculated for Sm, Sr and Pb in all models. Higher than average mixing proportions for *a* component observed in LREE and Eu, Zr and Ba.

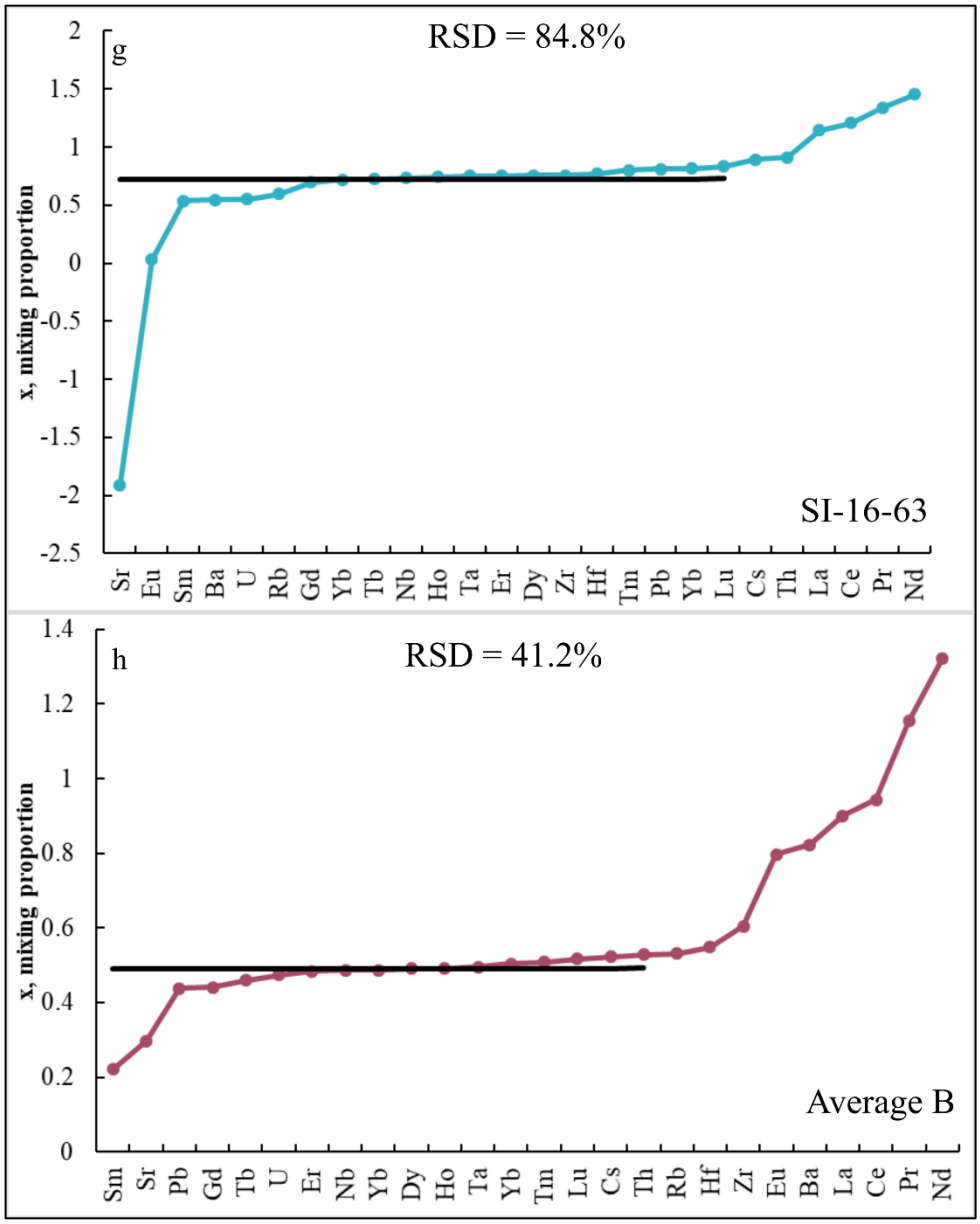

Figure 24. Mixing models using end-member group A (HQ2) and D (SI-16-loc33_smp2) values for *a* and *b* in equation 9 but different M values in g) and h). Sample ID in bottom right corner indicates B pumice used for M values (see text). General negative mixing proportions calculated for Sm, Sr and Pb in all models. Higher than average mixing proportions for *a* component observed in LREE and Eu, Zr and Ba.

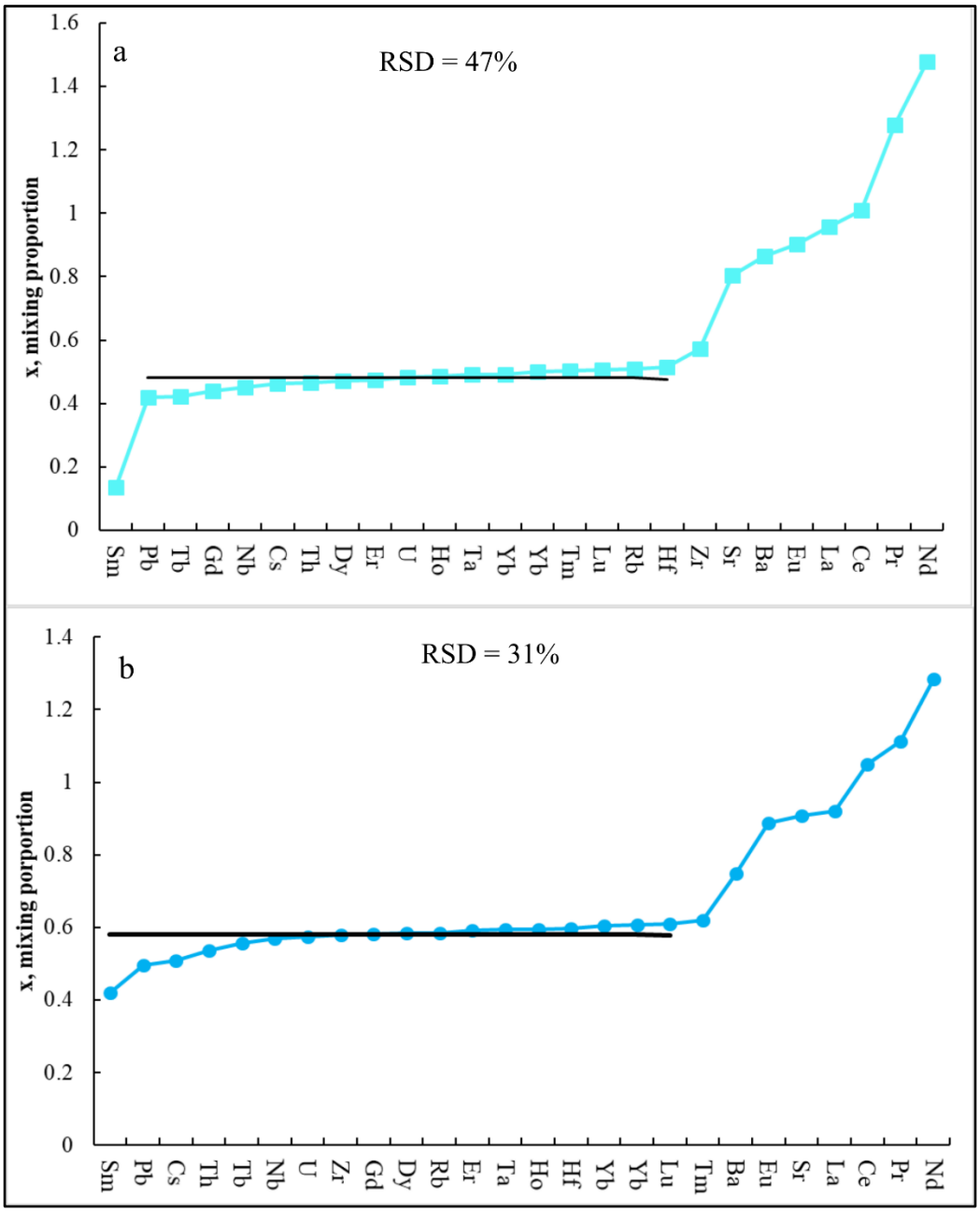

Figure 25. Mixing model 25a and 25b demonstrating the application of variable end-member rhyolites, group A and D, with the same group B value. Group B value used is indicated in Figure 20 with blue star. Group A and D samples used in mixing model 25a are HQ2 and SI-16-loc33_smp2. Group A and D samples used in mixing model 25b are 11-1P and 90-33DC-B. In both mixing models LREE plus Ba and Eu all trend away from the average mixing proportion in a positive trend. Sm is the only element displaying a negative mixing proportion in both models. Average (black line) calculated from values that agree with the most elements, i.e., 25a average derived from values of Pb through Hf.

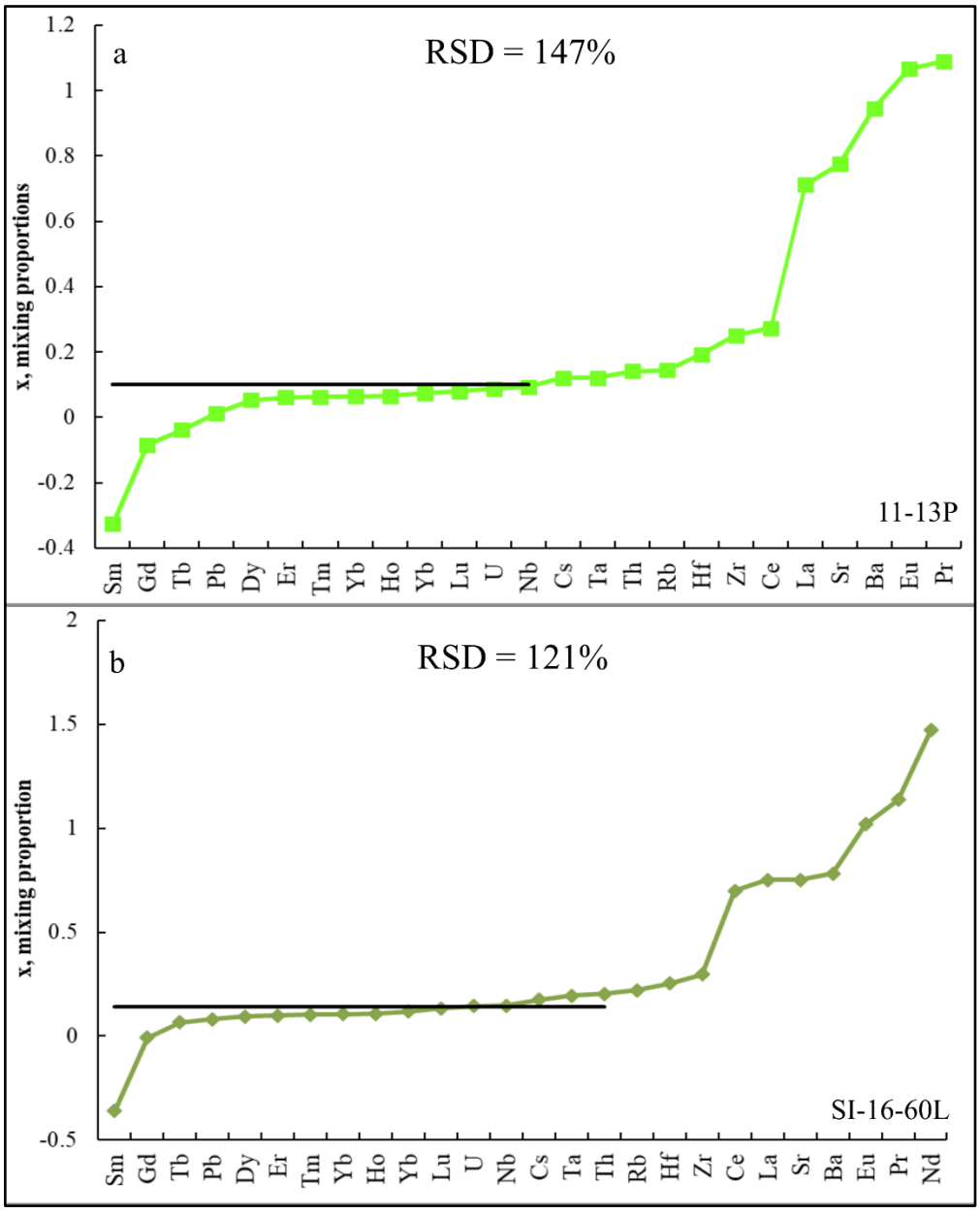

Figure 26. Mixing models 26a and 26b demonstrating the applicability of mixing end-member rhyolites A and D to generate group C pumices (11-13P and SI-16-60L). End-member rhyolites A and D values used in both models are the same as used in 21a-24h models. Note the large RSD values in both models, greater than all mixing models of A and D to produce group B. The LREE and Ba, Eu and Zr trend away from the average with greater mixing proportions relative to Sm that displays a negative mixing proportion in both models. Average (black line) calculated from mixing proportion values that satisfy the most elements.

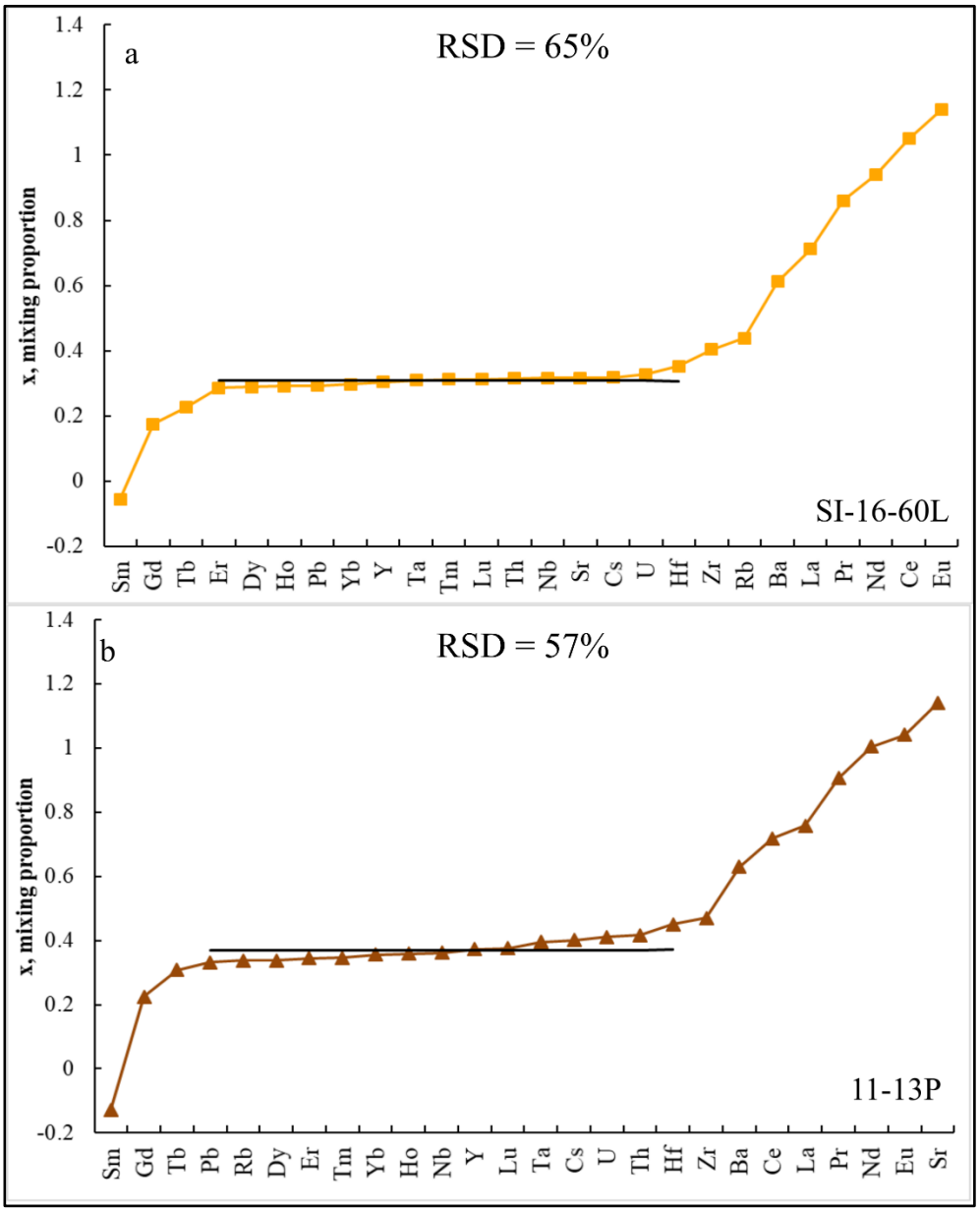

Figure 27. Mixing models 27a and 27b testing the applicability of intermediate rhyolite group B (11-4P6) and end-member rhyolite group D (SI-16-60D) mixing to generate group C pumices. Pumices used in mixing model are highlighted in orange in Figure 20. Notice the lower RSD values for 27a and 27b relative to the prior group C mixing models 26a and 26b. The LREE plus Eu, Ba and Zr display a positive trend away from the average mixing proportion line. Average calculated from mixing proportion values that agree with the most elements.

Role of Fractional Crystallization

The compositional range in the DCT was modeled in terms of Rayleigh fractional crystallization of rhyolite group D to generate C, C to generate B and B to generate A, with respect to Rb and Nb (**Figure 28**). The goal was to calculate the amount of crystal fractionation necessary to explain observed trace element gradients. Rb and Nb are likely among the most incompatible elements during fractional crystallization of DCT magmas based on observed enrichment patterns among DCT rhyolites. Rb is incompatible in all observed minerals of DCT magmas. In the case of Nb, the only mineral that indicates a compatible behavior is chevkinite, if obtained Nb_2O_5 concentrations reported in Table 6 are correct. However, Nb_2O_5 are low and combined with very low abundances of chevkinite, Nb is still highly incompatible. For these elements, a bulk partition coefficient near 0 is likely. A partition coefficient (D) ranging from 0.1 to 0.001 was used for Rb and Nb for mixing model calculations. Equation 11 is the equation for fractional crystallization where C_l is the concentration of the melt after crystallization, C_o is the original concentration of the melt, F is the fraction of melt remaining and D is the partition coefficient.

$$C_l = C_o * F^{D-1} \qquad (11)$$

The process of fractional crystallization enriches the melt in incompatible elements and depletes elements that behave compatibly. The actual processes to separate the crystalized minerals from the surrounding melt are debated. Separation can occur through crystal settling, sidewall crystallization where convection cells can assist in

liquid crystal separation from the crystallizing margins of the magma chamber, extraction of the melt from the crystals in a crystal rich mush zone, and possibly others.

The fractional crystallization of group D was modeled to determine the percent of crystallization needed to generate the concentrations of Rb and Nb in group C (**Table 15**). Observed concentrations of Nb in group C pumices range from 60.9-62.4 ppm while the Rb values are 108.8-114.0 ppm. The lowest Rb and Nb values of group C are generated after 10% fractional crystallization of group D. It only takes 12-16% crystallization to generate the entire Rb and Nb range exhibited in group C.

Table 15. Fractional crystallization model for group D to generate daughter liquid (C_l) similar in Rb and Nb concentration as group C. Bold indicates starting and ending range of Rb and Nb concentrations in group C pumices. Blue highlight indicates original concentration (C_o) of Rb and Nb in group D.

***F* (melt remaining)**	**C_l Rb (D = 0.01)**	***C_l Nb (D = 0.1)***
1	96.64	55.87
0.98	98.59	56.90
0.96	100.62	57.96
0.94	102.74	59.07
0.92	104.95	60.22
0.9	**107.26**	**61.43**
0.88	**109.67**	**62.68**
0.86	**112.20**	63.99
0.84	**114.84**	65.36

The percent of crystallization needed to generate the range in concentrations of Rb and Nb in group B was calculated through the fractional crystallization of group C (**Table 16**). The range of Nb values observed in group B are 69.0-96.2 ppm and 130.1-149.3 ppm for Rb. The lowest Rb and Nb group B values are attained after 12% crystallization of group C and 24% fractional crystallization produces the entire range of

Rb values exhibited in group B. However, it takes 36% crystallization of group C to attain the entire range of group B Nb values.

Table 16. Fractional crystallization model for group C to generate daughter liquid (C_l) similar in Rb and Nb concentration as group B. Bold indicates starting and ending range of Rb and Nb concentrations in group B pumices. Blue highlight indicates original concentration (C_o) of Rb and Nb in group C.

***F* (melt remaining)**	**C_l Rb (D = 0.01)**	**C_l Nb (D = 0.001)**
1	113.97	60.90
0.98	116.28	62.15
0.96	118.67	63.44
0.94	121.17	64.79
0.92	123.78	66.19
0.9	126.50	67.66
0.88	**129.35**	**69.20**
0.86	**132.33**	**70.81**
0.84	**135.45**	**72.49**
0.82	**138.72**	**74.26**
0.8	**142.15**	**76.11**
0.78	**145.76**	**78.06**
0.76	**149.55**	**80.11**
0.74	153.55	**82.28**
0.72	157.78	**84.56**
0.7	162.24	**86.97**
0.68	166.96	**89.53**
0.66	171.97	**92.24**
0.64	177.29	**95.12**

The percent of fractional crystallization of group B is calculated to generate Rb and Nb concentrations of group A (**Table 17**). The concentrations of Rb and Nb in group A are 161.4-186.0 ppm, and 99.9-111.7 ppm respectively. Ten percent crystallization of group B generates the lowest values of Rb and 4% crystallization of Nb in group A. The entire range of Rb is produced after 22% fractional crystallization. It takes 16% crystallization of group B to attain the entire range of Nb values in group A.

Table 17. Fractional crystallization model for group B to generate daughter liquid (C_l) similar in Rb and Nb concentration as group A. Bold indicates starting and ending range of Rb and Nb concentrations in group A pumices.

F (melt remaining)	Cl Rb (D = 0.01)	Cl Nb (D = 0.1)
1	145.70	96.21
0.98	148.64	97.97
0.96	151.71	**99.81**
0.94	154.90	**101.72**
0.92	158.23	**103.71**
0.9	**161.72**	**105.78**
0.88	**165.35**	**107.94**
0.86	**169.16**	**110.20**
0.84	**173.15**	**112.55**
0.82	**177.33**	115.02
0.8	**181.72**	117.61
0.78	**186.33**	120.32
0.76	191.18	123.16
0.74	196.30	126.16
0.72	201.69	129.30
0.7	207.40	110.96

Fractional crystallization accompanied with the mixing scenarios described above may explain the trace element gradients in all high-silica rhyolites. However, when considering fractional crystallization scenarios, it is important to remember that rhyolitic melt must be essentially invariant at 76 w.t.% SiO_2 and alkali concentrations must stay above 1 in molar (Na+K/Al), i.e. to stay in the peralkaline field. The total amount of crystal fractionation from D to B is 32%, when only considering the percent of crystallization needed to attain the lowest Rb and Nb value in the daughter liquid. During progressive crystallization, the following minerals will crystallize; quartz, feldspar,

clinopyroxene, ilmenite, and chevkinite as an accessory phase. As quartz contains 100% SiO_2, crystallization of this mineral will subsequently deplete the melt in silica. However, feldspar containing 67% SiO_2, clinopyroxene containing 48% SiO_2 and ilmenite containing no silica, all will enrich the melt in silica during crystallization. Chevkinite contains ~20% SiO_2, thus principally its crystallization will enrich the melt in SiO_2, however the expected amounts of chevkinite to crystallize are minimal and therefore no noticeable effect on major elements is expected. On the other hand, the light rare earth elements, that are exceedingly compatible in chevkinite, which will deplete the melt in LREE elements. To maintain the silica in the melt at 76% a ratio of minerals depleting the melt versus minerals enriching the melt must remain balanced. During fractional crystallization, the percentage of minerals crystallizing are as follows: 33% quartz, 58.5% feldspar, 8% clinopyroxene and 0.5% ilmenite, this proportion of minerals will keep the silica buffered at 76% SiO2 and mol Na+K/Al of this assemblage is 0.95 indicate that fractionation of this assemblage will keep melt peralkaline with a slight increase in degree of peralkalinity.

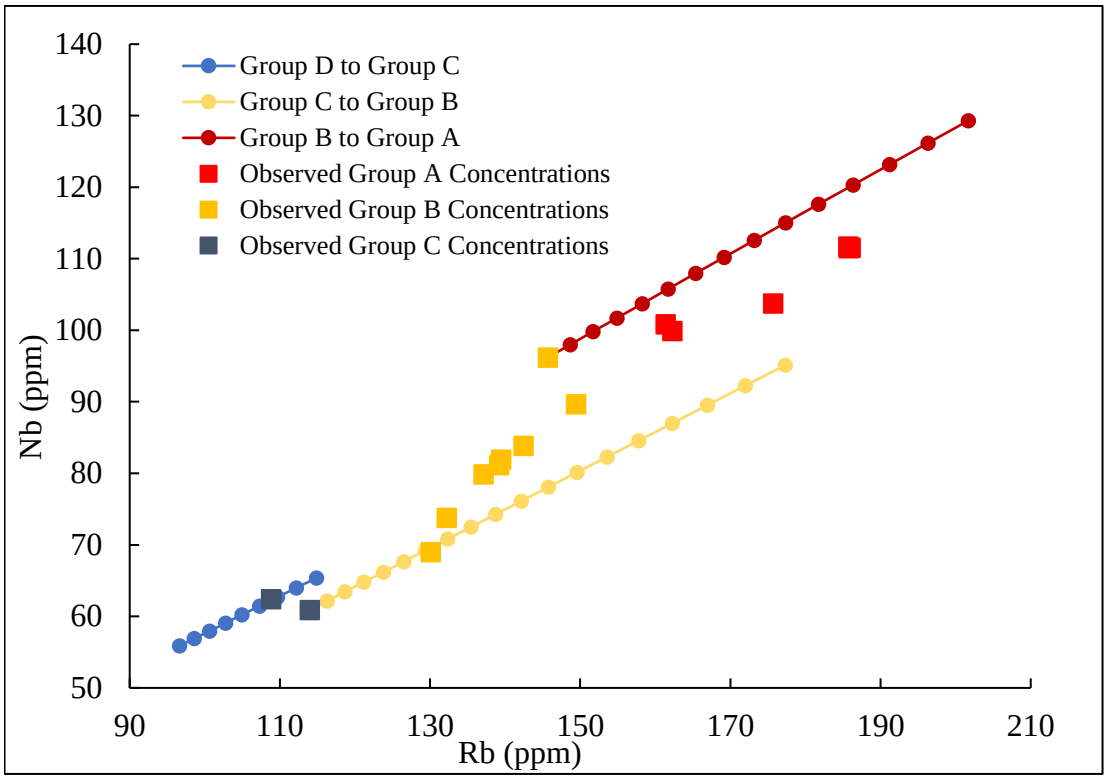

Figure 28. Modeled fractional crystallization of groups B, C and D. Circle symbol represent the modeled Rb and Nb (ppm) concentrations found in Tables 15, 16 and 17. Square symbols indicate observed Rb and Nb (ppm) within pumices from groups A, B and C. Corresponding fractionation increments found in Tables 15, 16 and 17.

Low $\delta^{18}O$ Rhyolites of The Devine Canyon Tuff

Meteoric waters are generally isotopically-light leading to negative $\delta^{18}O$ values, whereas silicate rocks and magmas trend towards positive $\delta^{18}O$ values with basaltic magmas having values of 5.5-5.9‰ (Bindeman, 2008). Crustal rocks, metasediments and S-type granites, inherit more positive $\delta^{18}O$ signatures from their source. However, rocks that interact with low-$\delta^{18}O$ meteoric water at high-temperature, resulting in hydrothermal alteration, display lower $\delta^{18}O$ values relative to mantle rocks and their direct differentiates (Bindeman, 2008). Equilibrium isotope fractionation differs between certain minerals based on their Si-O-M bonds. The heavier oxygen isotope will partition itself into a mineral with strong, more covalent, bonds due to variable vibrational frequencies, i.e., quartz. Thus, pure silica (quartz) will incorporate the heavier isotope first while other common igneous minerals, albite, anorthite, zircon, pyroxene, amphibole, biotite, etc., will progressively become lighter (Bindeman, 2008).

Low $\delta^{18}O$ values in magmas are hypothesized to be induced by several processes including: 1) partial melting and mixing of hydrothermally altered rocks with normal magma (e.g., Bacon et al., 1989; Grunder 1987; Laron and Tayloe, 1986) ; 2) rapid assimilation of rocks significantly different in $\delta^{18}O$ that affects the magma, but not original phenocrysts (Taylor, 1986); or 3) bulk melting of shallow hydrothermally altered rocks that subsequently erupt at the surface (Bindeman and Valley, 2000) or 4) direct assimilation of meteoric water (Hildreth et al, 1984), although this is very unlikely.

The Devine Canyon Tuff's $\delta^{18}O$ values range from 6.2‰ to 4.57‰. Thus, the DCT rhyolites fall within the "low" - $\delta^{18}O$ category defined by Bindeman (2008) and

others. The Harney Basin setting today, with its proximity to hydrologic system of lakes, rivers and hot springs, could make it an ideal setting for producing low-$\delta^{18}O$ crustal rocks above and around the magma chamber. Considering the extensional stress regime and distributed normal faulting within the High Lava Plains today we assume that groundwater could easily find pathways deep into the crust. Furthermore, assuming the $\delta^{18}O$ values collected in the Silver (-15.35‰) and Donner and Blitzen (-14.94‰) rivers reflect similar $\delta^{18}O$ values present during the mid-Miocene provides the input of negative $\delta^{18}O$ water into the crust.

Magma Generation Model

The model here provides a scenario by which observed diversity of rhyolite magmas are created after two distinct rhyolite batches, assuming group A and D, were generated through partial melting dominated processes. If this assumption is viable it will require further testing to demonstrate that partial melting is indeed a viable process to generate these highly evolved rhyolites. Initial models reveal the trace element enrichments seen in the DCT (Zr, Rb, Th, Nb) are not achievable through partial melting of dacites exposed in the northern vicinity of the High Lava Plains (Isom and Streck, unpublished data). However, 30% partial melting of the group E dacite to generate group D high-silica rhyolite reveals a better fit. Finally, partially melting group D to generate group A high-silica rhyolite again reveals unachievable trace element concentrations with a reasonable amount of partial melting.

High-silica rhyolite groups A and D reside in a single reservoir in the upper crust where assimilation of hydrothermally altered crustal rock, or crustal rock which has reacted with depleted meteoric waters, can create the observed low-$\delta^{18}O$ signatures. However, the assimilation process was not homogenous throughout the magma chamber creating variability in $\delta^{18}O$ values.

Initial mixing of A and D magmas generated B magmas that mixed again with D to make rhyolite C compositions. Subsequent crystallization and removal of crystals lead to modification of mixing induced chemical gradients as observed in the compatible trace elements of the LREE, Ba, Sr, and Eu. As crystallization progresses convection decreases and intermediate rhyolite members B and C, being less crystal-rich, sit stratigraphically below group A and above group D in the magma chamber. The crystallization and convective removal of liquid from crystals (Sparks et al., 1984) could generate more melt similar to the more evolved group A and B rhyolites. Furthermore, employing crystal settling will explain the dramatic increase of crystals within group D. As group B and C crystallize the more evolved liquid is generated and removed, buoyantly driven to the top of the chamber, while crystals settle below within group D.

An influx of hot (~900 C°) magma that affected the entire reservoir is represented by the bright rims surrounding darker cores observed in quartz phenocrysts from all rhyolite groups A – D. Heterogeneous internal zonations and anhedral cores reflect a period of thermal disequilibrium in the magma chamber, i.e., influx of hotter magma or magma mixing (Watts et al., 1997). During this time, it is hypothesized that the group D rhyolite mixed with the influx of magma, possibly basalt, to generate the group E dacite.

Furthermore, the injection of hot basaltic magma could have destabilized the chamber causing the eruption of the Devine Canyon Tuff.

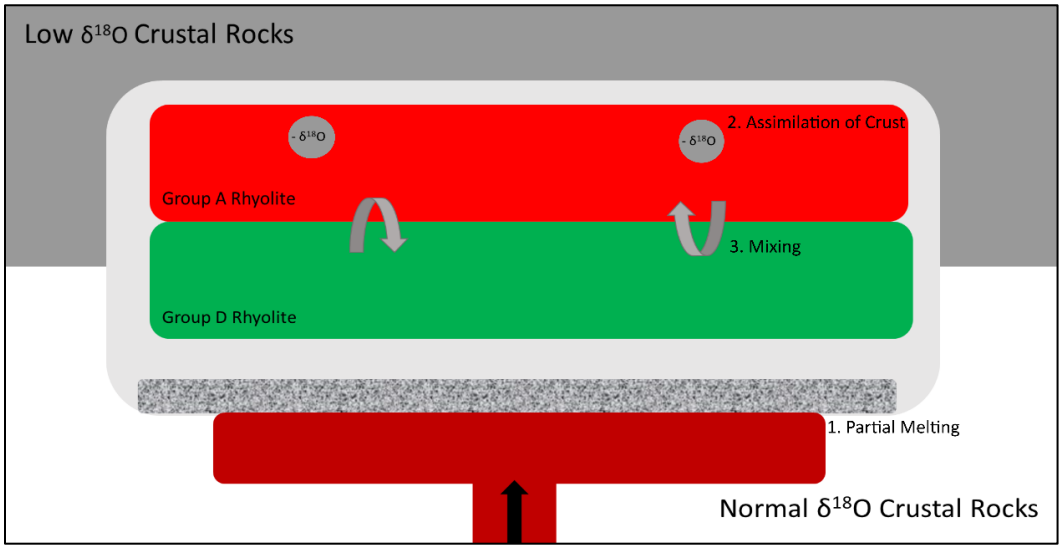

Figure 29. Magma chamber model of the DCT. Figure depicts first three processes to occur within the magma chamber. 1) injection of a basic magma, which undergoes two partial melting events of a component to generate end-ember rhyolites (A & D); 2) assimilation of low-$\delta^{18}O$ crust lowering the $\delta^{18}O_{magma}$ values of group A rhyolite; and 3) mixing of end-member rhyolites where group D inherits a similar low $\delta^{18}O_{magma}$ value.

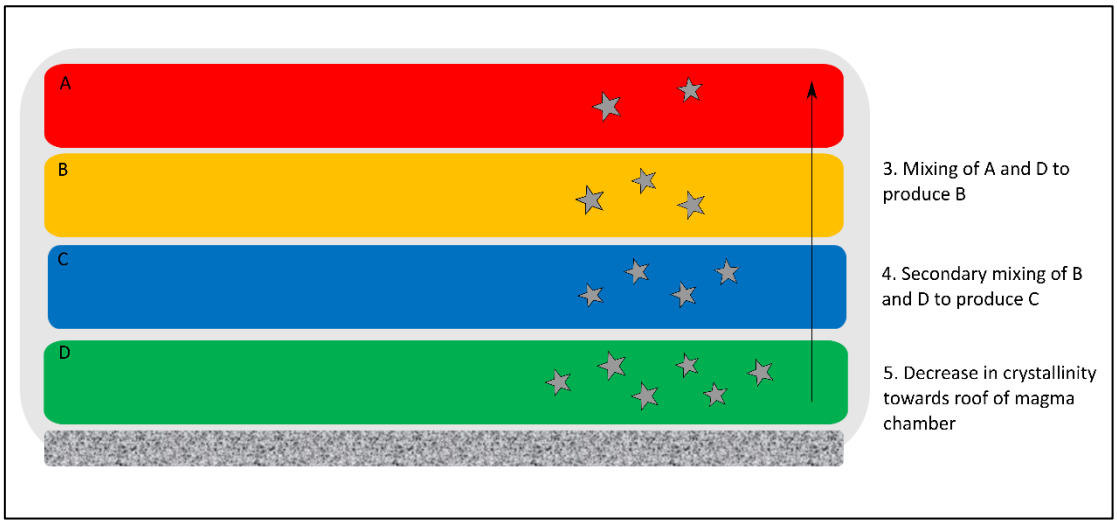

Figure 30. Magma chamber model continued. 3) mixing of end-member rhyolites produce intermediate rhyolite B; 4) secondary mixing of B and D rhyolite produce intermediate rhyolite C; 5) crystallization decreases roof-ward possibly due to crystal settling.

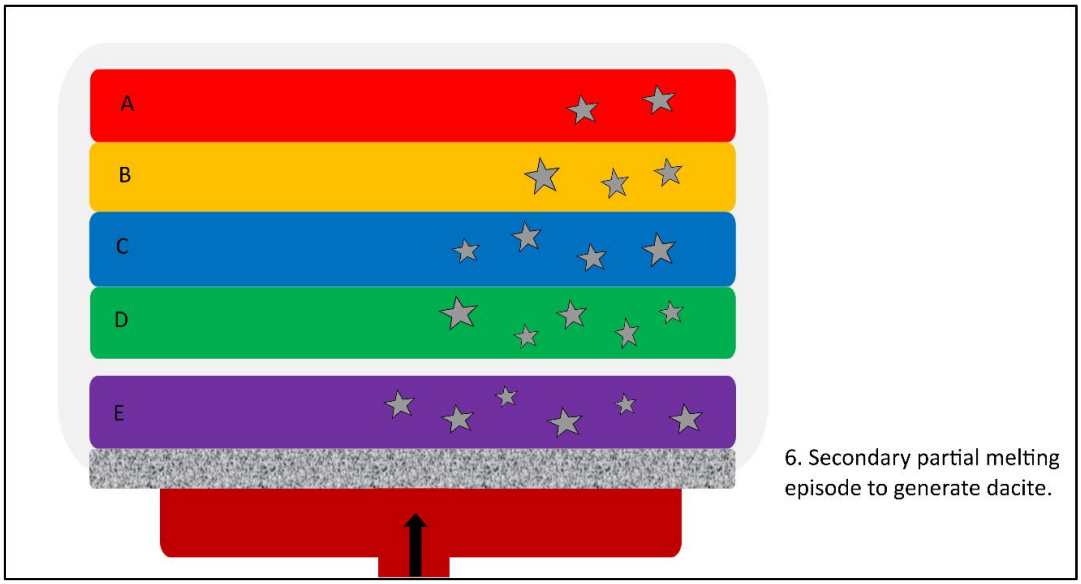

Figure 31. Magma chamber model continued. 6) secondary influx of basic magma causing partial melting to generate dacite.

CONCLUSIONS

The Devine Canyon Tuff erupted ~250-300 km^3 of pyroclastic material to produce a single cooling unit. This research supplements previous studies on the DCT with oxygen isotope data, calculated temperature data from zoned quartz phenocrysts, H_2O and CO_2 content and extends chemical data previously collected for all groups, and data on accessory phase assemblages of all DCT magmas.

The DCT is a strongly compositionally zoned ignimbrite that reflects the inverted zonation of a magma reservoir that grades upward from least evolved, crystal-rich dacite, to most evolved, crystal-poor high-silica rhyolite, with a gradational trace element enrichment. Group A exhibits the highest water content, >3 w.t. %, attesting to a roofward increase in H_2O, consistent with the lower crystallinity. Deeper reaches of the reservoir had <1 w.t. % water. Maximum volatile saturation pressures are less than 1,000 bars. Using these for minimal depth estimates indicates a depth of less than ~3.5 km for the pre-eruptive DCT rhyolites.

The DCT exhibits low-$\delta^{18}O$ values across all high-silica rhyolite and dacite groups. The calculated $\delta^{18}O_{magma}$ values range from 4.5 to 5.76‰ based on equilibrium with sanidine and quartz. Single crystal analysis reveals variation of as much as 1.5 ‰ $\delta^{18}O$ values over the whole compositional range of all magma groups. Within the DCT chevkinite, apatite, titanomagngetite, ilmenite, zircon and pyrite are the accessory phases present in hedenbergite. Removal of chevkinite, which incorporates the LREE, is consistent with the observed progressive depletion of LREE and which is illustrated in REE diagrams. The presence of zircon allowed the application of the zircon

geothermometer yielding a temperature of 1000-900 C°. The bright Ti-rich rims, seen in all high-silica rhyolite groups, indicates the influx of hotter magma, which affected all magmas. This also effectively excluding the possibility that A to D rhyolites erupted from separated reservoirs that mixed during eruption. We deduce a temperature of 900 C° just prior to eruption.

The mixing of end-member rhyolites A and D produced rhyolite B, and subsequent mixing of intermediate rhyolite B and end-member rhyolite D generated rhyolite C. However, some trace element inconsistencies, between mixing model and observed intermediate rhyolites suggest a secondary process. Post mixing, rhyolites B and C require some modification by fractional crystallization to account for LREE and other inconsistencies between mixed models and observed rhyolites. I envision a scenario where all magmas are stored within a single reservoir, which allows for mixing and fractional crystallization to occur. Finally, the dacite is likely generated from the mixing of group D rhyolite and an intrusive fractionated basalt, which could have led to the eruption of the Devine Canyon Tuff.

REFERENCES

Anderson, A.T., 1976, Magma mixing: petrological process and volcanological tool: Journal of Volcanology and Geothermal Research, v. 1, p. 3–33, doi: 10.1016/0377-0273(76)90016-0.

Bacon, C.R., Adami, L.H., and Lanphere, M.A., 1989, Direct evidence for the origin of low-18O silicic magmas: quenched samples of a magma chamber's partially-fused granitoid walls, Crater Lake, Oregon: Earth and Planetary Science Letters, v. 96, p. 199–208, doi: 10.1016/0012-821X(89)90132-5.

Baertschi, P., 1976, Absolute 18O content of standard mean ocean water: Earth and Planetary Science Letters, v. 31, p. 341–344, doi: 10.1016/0012-821X(76)90115-1.

Bindeman, I., 2008a, Oxygen Isotopes in Mantle and Crustal Magmas as Revealed by Single Crystal Analysis: Reviews in Mineralogy and Geochemistry, v. 69, p. 445–478, doi: 10.2138/rmg.2008.69.12.

Bindeman, I., 2008b, Oxygen Isotopes in Mantle and Crustal Magmas as Revealed by Single Crystal Analysis: Reviews in Mineralogy and Geochemistry, v. 69, p. 445–478, doi: 10.2138/rmg.2008.69.12.

Bindeman, I.N., Ponomareva, V. V., Bailey, J.C., and Valley, J.W., 2004, Volcanic arc of Kamchatka: A province with high-??18O magma sources and large-scale 18O/16O depletion of the upper crust: Geochimica et Cosmochimica Acta, v. 68, p. 841–865, doi: 10.1016/j.gca.2003.07.009.

Bindeman, I.N., and Valley, J.W., 2000, Formation of low-??18O rhyolites after caldera collapse at Yellowstone, Wyoming, USA: Geology, v. 28, p. 719–722, doi: 10.1130/0091-7613(2000)28<719:FOLRAC>2.0.CO.

Bindeman, I.N., and Valley, J.W., 2002, Oxygen isotope study of the Long Valley magma system, California: isotope thermometry and convection in large silicic magma bodies: Contributions to Mineralogy and Petrology, v. 144, p. 185–205, doi: 10.1007/s00410-002-0371-8.

Cathey, H.E., and Nash, B.P., 2004, The Cougar Point Tuff: Implications for Thermochemical Zonation and Longevity of High-Temperature, Large-Volume Silicic Magmas of the Miocene Yellowstone Hotspot: Journal of Petrology, v. 45, p. 27–58, doi: 10.1093/petrology/egg081.

Eichelberger, J.C., 1975, Origin of andesite and dacite: Evidence of mixing at Glass Mountain in California and at other circum-Pacific volcanoes: Bulletin of the Geological Society of America, v. 86, p. 1381–1391, doi: 10.1130/0016-7606(1975)86<1381:OOAADE>2.0.CO;2.

Ellis, B.S., Bachmann, O., and Wolff, J.A., 2014, Cumulate fragments in silicic ignimbrites: The case of the Snake River Plain: Geology, v. 42, p. 431–434, doi: 10.1130/G35399.1.

Ellis, B.S., Barry, T., Branney, M.J., Wolff, J.A., Bindeman, I., Wilson, R., and Bonnichsen, B., 2010, Petrologic constraints on the development of a large-volume, high temperature, silicic magma system: The Twin Falls eruptive centre, central Snake River Plain: Lithos, v. 120, p. 475–489, doi: 10.1016/j.lithos.2010.09.008.

Ford, M.T., Grunder, A.L., and Duncan, R.A., 2013, Bimodal volcanism of the High Lava Plains and Northwestern Basin and Range of Oregon: Distribution and tectonic implications of age-progressive rhyolites: Geochemistry, Geophysics, Geosystems, v. 14, p. 2836–2857, doi: 10.1002/ggge.20175.

Greene, R.C., 1973, Petrology of the Welded Tuff of Devine Canyon, Southeastern Oregon: USGS Professional Paper, v. 797.

Hervig, R.L., and Dunbar, N.W., 1992, Cause of chemical zoning in the Bishop (California) and Bandelier (New Mexico) magma chambers: Earth and Planetary Science Letters, v. 111, p. 97–108, doi: 10.1016/0012-821X(92)90172-R.

Hildreth, W., 1981a, Gradients in silicic magma chambers: Implications for lithospheric magmatism: v. 86, 10153 p., doi: 10.1029/JB086iB11p10153.

Hildreth, W., 1981b, Gradients in silicic magma chambers: Implications for lithospheric magmatism: Journal of Geophysical Research: Solid Earth, v. 86, p. 10153–10192, doi: 10.1029/JB086iB11p10153.

Hildreth, W., 2004, Volcanological perspectives on Long Valley, Mammoth Mountain, and Mono Craters: Several contiguous but discrete systems: Journal of Volcanology and Geothermal Research, v. 136, p. 169–198, doi: 10.1016/j.jvolgeores.2004.05.019.

Hildreth, W., Christiansen, R.L., and O'Neil, J.R., 1984, Catastrophic isotopic modification of rhyolitic magma at times of caldera subsidence, Yellowstone Plateau Volcanic Field: Journal of Geophysical Research, v. 89, p. 8339–8369, doi: 10.1029/JB089iB10p08339.

Hooper, P.R., Binger, G.B., and Lees, K.R., 2002, Ages of the Steen and Columbia River flood basalts and their relationship to extension-related calc-alkalic volcanism in eastern Oregon: Geological Society Of America Bulletin, v. 114, p. 923–924, doi: 10.1130/0016-7606(2002)114.

Johnson, D.M., Hooper, P.R., and Conrey, R.M., 1999, XRF analysis of rocks and minerals for major and trace elements on a single low dilution Li-tetraborate fused bead: Advances in X-ray Analysis, v. 41, p. 843–867.

Jordan, B.T., Grunder, A.L., Duncan, R.A., and Deino, A.L., 2004, Geochronology of age-progressive volcanism of the Oregon High Lava Plains: Implications for the plume interpretation of Yellowstone: Journal of Geophysical Research B: Solid Earth, v. 109, doi: 10.1029/2003JB002776.

Leeman, W.P., MacRae, C.M., Wilson, N.C., Torpy, A., Lee, C.-T.A., Student, J.J., Thomas, J.B., and Vicenzi, E.P., 2012, A study of cathodoluminescence and trace element compositional zoning in natural quartz from volcanic rocks: mapping titanium content in quartz.: Microscopy and microanalysis, v. 18, p. 1322–1341, doi: 10.1017/S1431927612013426.

Leschik, M., Heide, G., Frischat, G.H., Behrens, H., Wiedenbeck, M., Wagner, N., Heide, K., Geißler, H., and Reinholz, U., 2004, Determination of H2O and D2O contents in rhyolitic glasses: Physics and Chemistry of Glasses, v. 45, p. 238–251, doi: 10.1007/s10765-009-0615-1.

Macdonald, R., and Belkin, H.E., 2002, Compositional variation in minerals of the chevkinite group: Mineralogical Magazine, v. 66, p. 1075–1098, doi: 10.1180/0026461026660078.

Mahood, G., and Hildreth, W., 1983, Large partition coefficients for trace elements in high-silica rhyolites: Geochimica et Cosmochimica Acta, v. 47, p. 11–30, doi: 10.1016/0016-7037(83)90087-X.

Michael, P.J., 1988, Partition coefficients for rare earth elements in mafic minerals of high silica rhyolites: The importance of accessory mineral inclusions: Geochimica et Cosmochimica Acta, v. 52, p. 275–282, doi: 10.1016/0016-7037(88)90083-X.

Newman, S., and Lowenstern, J.B., 2002, VOLATILECALC: A silicate melt-H2O-CO2 solution model written in Visual Basic for excel: Computers and Geosciences, v. 28, p. 597–604, doi: 10.1016/S0098-3004(01)00081-4.

Pierce, K.L., and Morgan, L.A., 1992, The track of the Yellowstone hotspot: Volcanism, faulting and uplift, in Regional Geology of Eastern Idaho and Western Wyoming: Geological Society Of America Bulletin, v. 179, p. 1–53.

Shoemaker, K.A., and Hart, W.K., 2002, Temporal controls on basalt genesis and evolution on the Owyhee Plateau, Idaho and Oregon: Idaho Geologic Survey Bulliten, v. 30, p. 313–328.

Simakin, A.G., and Bindeman, I.N., 2012, Remelting in caldera and rift environments and the genesis of hot, “recycled” rhyolites: Earth and Planetary Science Letters, v. 337–338, p. 224–235, doi: 10.1016/j.epsl.2012.04.011.

Skirius, C.M., Peterson, J.W., and Anderson, A.T., 1990, Homogenizing rhyolitic glass inclusions from the Bishop Tuff: American Mineralogist, v. 75, p. 1381–1398.

Smith, R.L., and Leudke, R.G., 1984, Potentially active volcanic lineaments and loci in western conterminous United States, in, Explosive Volcanism: Inception, Evolution and Hazards, National Research Council: National Research Council, p. 47–66.

Sparks, R.S.J., Huppert, H.E., Turner, J.S., Sakuyama, M., and O'Hara, M.J., 1984, The fluid dynamics of evolving magma chambers: Philos. Trans. R. Soc. Lond., v. 310, p. 511–534, doi: DOI: 10.1098/rspa.1955.0102.

Streck, M.J., 2014, Evaluation of crystal mush extraction models to explain crystal-poor rhyolites: Journal of Volcanology and Geothermal Research, v. 284, p. 79–94, doi: 10.1016/j.jvolgeores.2014.07.005.

Streck, M.J., and Grunder, A.L., 1997, Compositional gradients and gaps in high-silica rhyolites of the Rattlesnake Tuff, Oregon: Journal of Petrology, v. 38, p. 133–163, doi: 10.1093/petrology/38.1.133.

Streck, M.J., and Grunder, A.L., 2013, Erratum: Temporal and crustal effects on differentiation of tholeiite to calcalkaline and ferro-trachytic suites, high lava plains, Oregon, USA (Geochemistry, Geophysics, Geosystems (2013) 14 (1678-1684)): Geochemistry, Geophysics, Geosystems, v. 14, p. 1678–1684, doi: 10.1002/ggge.20099.

Streck, M.J., and Grunder, A.L., 2008, Phenocryst-poor rhyolites of bimodal, tholeiitic provinces: the Rattlesnake Tuff and implications for mush extraction models: Bulletin of Volcanology, v. 70, p. 385–401, doi: 10.1007/s00445-007-0144-3.

Sun, S. -s., and McDonough, W.F., 1989, Chemical and isotopic systematics of oceanic basalts: implications for mantle composition and processes: Geological Society, London, Special Publications, v. 42, p. 313–345, doi: 10.1144/GSL.SP.1989.042.01.19.

Trench, D., Meigs, A., and Grunder, A., 2012, Termination of the northwestern Basin and Range province into a clockwise rotating region of transtension and volcanism, southeast Oregon: Journal of Structural Geology, v. 39, p. 52–65, doi: 10.1016/j.jsg.2012.03.007.

Wallace, P.J., Anderson, Jr., A.T., and Davis, A.M., 1999, Gradients in H2O, CO2, and exsolved gas in a large-volume silicic magma system: Interpreting the record preserved in melt inclusions from the Bishop Tuff: Journal of Geophysical Research, v. 104, p. 20097–20122, doi: 10.1029/1999JB900207.

Watson, E.B., and Capobianco, C.J., 1981, Phosphorus and the rare earth elements in felsic magmas: an assessment of the role of apatite: Geochimica et Cosmochimica Acta, v. 45, p. 2349–2358, doi: 10.1016/0016-7037(81)90088-0.

Watson, E.B., Wark, D.A., and Thomas, J.B., 2006, Crystallization thermometers for

zircon and rutile: Contributions to Mineralogy and Petrology, v. 151, p. 413, doi: 10.1007/s00410-006-0068-5.

Wilson, C.J.N., Seward, T.M., Allan, A.S.R., Charlier, B.L.A., and Bello, L., 2012, A comment on: “TitaniQ under pressure: The effect of pressure and temperature on the solubility of Ti in quartz”, by Jay B. Thomas, E. Bruce Watson, Frank S. Spear, Philip T. Shemella, Saroj K. Nayak and Antonio Lanzirotti: Contributions to Mineralogy and Petrology, v. 164, p. 359–368, doi: 10.1007/s00410-012-0757-1.

Wolff, J.A., Ellis, B.S., Ramos, F.C., Starkel, W.A., Boroughs, S., Olin, P.H., and Bachmann, O., 2015, Remelting of cumulates as a process for producing chemical zoning in silicic tuffs: A comparison of cool, wet and hot, dry rhyolitic magma systems: Lithos, v. 236–237, p. 275–286, doi: 10.1016/j.lithos.2015.09.002.

Wysoczanski, R., and Tani, K., 2006, Spectroscopic FTIR imaging of water species in silicic volcanic glasses and melt inclusions: An example from the Izu-Bonin arc: Journal of Volcanology and Geothermal Research, v. 156, p. 302–314, doi: 10.1016/j.jvolgeores.2006.03.024.

APPENDIX A- Geochemical Data

Table A1. XRF Results

Sample ID	DCT-8.1-BA	DCT-10-BA	SI-16-72	SI-16-62a
Sample Type	Bulk Tuff	Bulk Tuff	Pumice	Pumice Composite
Coordinates	43.8413°, -118.7721°	43.8418°, -118.7718°	43.7474°, -118.7969°	42.9842°, -118.8733°
This Study				
XRF Normalized 100% volatile free, weight %				
SiO_2	76.79	76.21	71.28	75.85
TiO_2	0.187	0.250	0.431	0.193
Al_2O_3	10.87	11.67	12.95	11.25
FeO*	2.86	2.71	4.52	3.32
MnO	0.060	0.042	0.146	0.059
MgO	0.00	0.09	0.10	0.26
CaO	0.14	0.30	0.96	0.23
Na_2O	3.42	3.36	3.57	3.62
K_2O	5.67	5.35	5.97	5.21
P_2O_5	0.000	0.018	0.060	0.002
Pre-normalized Total	96.28	96.39	96.86	94.65
LOI %	2.62	2.74	2.49	4.54
XRF, unnormalized ppm				
Ni	3	4	3	4
Cr	1	2	6	3
Sc	0	1	3	1
V	2	5	6	15
Ba	33	123	230	11
Rb	157	96	71	161
Sr	3	19	28	9
Zr	1319	741	595	1539
Y	163	98	101	173
Nb	93.9	56.5	59.2	101.4
Ga	30	26	28	30
Cu	6	5	6	7
Zn	265	179	176	282
Pb	38	20	16	41
La	85	111	174	77
Ce	187	204	325	173
Th	15	10	9	17
Nd	93	102	146	91
U	6	3	2	5

Table A2. ICP-MS Results

Sample ID	DCT-8.1-BA	DCT-10-BA	SI-16-72	SI-16-62a
Sample Type	Bulk Tuff	Bulk Tuff	Pumice	Pumice Composite
Coordinates	43.8413°, -118.7721°	43.8418°, -118.7718°	43.7474°, -118.7969°	42.9842°, -118.8733°
This Study				
ICP-MS, ppm				
La	90.51	118.32	184.33	82.81
Ce	193.86	209.72	354.79	179.69
Pr	24.54	27.22	39.87	23.48
Nd	98.13	104.44	152.48	94.89
Sm	24.90	21.33	26.91	25.42
Eu	0.69	0.96	1.76	0.72
Gd	25.75	18.71	22.18	27.00
Tb	4.71	3.13	3.48	4.98
Dy	30.36	19.24	20.60	32.20
Ho	6.39	3.93	4.13	6.80
Er	17.98	10.89	11.37	19.32
Tm	2.72	1.61	1.69	2.89
Yb	17.43	10.46	10.95	18.41
Lu	2.69	1.61	1.80	2.83
Ba	32	123	233	10
Th	16.05	9.70	8.24	17.94
Nb	91.88	55.30	58.49	99.91
Yb	164.96	97.81	100.67	175.19
Hf	29.48	16.52	13.86	32.37
Ta	5.64	3.21	3.10	6.34
U	6.46	3.44	2.61	6.92
Pb	35.51	19.65	16.04	38.92
Rb	157.7	96.5	70.1	162.2
Cs	4.83	2.61	1.76	5.59
Sr	4	19	28	9
Sc	0.0	1.1	2.2	0.8
Zr	1312	753	613	1508

Table A1 continued.

Sample ID	SI-16-62c	SI-16-66	SI-16-66a	SI-16-66c
Sample Type	Bulk Tuff	Bulk Tuff	Bulk Tuff	Lithic
Coordinates	42.9850°, -118.8734°	43.7125°, -119.0083°	43.7125°, -119.0083°	43.7125°, -119.0083°
This Study				
XRF Normalized 100% volatile free, weight %				
SiO_2	75.06	73.37	75.44	75.35
TiO_2	0.186	0.357	0.313	0.262
Al_2O_3	11.01	14.12	12.33	12.12
FeO*	2.91	3.23	2.85	2.93
MnO	0.062	0.073	0.035	0.068
MgO	0.63	0.97	0.16	0.38
CaO	1.76	0.85	0.18	0.47
Na_2O	3.47	2.76	4.08	2.42
K_2O	4.89	4.22	4.56	6.00
P_2O_5	0.022	0.045	0.050	0.015
Pre-normalized Total	93.68	93.33	97.97	94.75
LOI %	5.48	6.31	1.62	4.35
XRF, unnormalized ppm				
Ni	5	3	4	3
Cr	2	6	5	4
Sc	1	4	2	1
V	11	16	19	6
Ba	29	255	163	130
Rb	134	52	95	94
Sr	37	61	24	27
Zr	1437	594	722	780
Y	154	85	75	106
Nb	86.8	46.6	55.5	58.6
Ga	28	28	27	27
Cu	13	7	8	6
Zn	242	144	157	161
Pb	35	17	22	20
La	80	101	83	109
Ce	171	196	169	210
Th	15	8	10	10
Nd	85	87	76	100
U	6	2	3	3

Table A2 continued.

Sample ID	SI-16-62c	SI-16-66	SI-16-66a	SI-16-66c
Sample Type	Bulk Tuff	Bulk Tuff	Bulk Tuff	Lithic
Coordinates	42.9850°, -118.8734°	43.7125°, -119.0083°	43.7125°, -119.0083°	43.7125°, -119.0083°
This Study				
ICP-MS, ppm				
La	82.06	108.93	88.70	117.89
Ce	177.84	208.33	178.68	219.37
Pr	22.59	24.44	21.23	27.29
Nd	90.69	93.65	81.22	105.08
Sm	23.38	18.27	16.69	21.11
Eu	0.71	1.21	0.89	0.87
Gd	24.04	16.17	14.33	19.48
Tb	4.39	2.69	2.41	3.26
Dy	28.68	16.29	14.67	20.19
Ho	6.02	3.35	3.02	4.17
Er	17.28	9.35	8.51	11.74
Tm	2.59	1.40	1.29	1.75
Yb	16.42	9.19	8.28	11.30
Lu	2.50	1.45	1.25	1.80
Ba	25	267	162	131
Th	15.17	7.91	9.78	10.07
Nb	85.87	46.21	54.70	57.33
Yb	155.97	84.93	74.68	106.42
Hf	27.82	13.47	16.38	17.26
Ta	5.34	2.68	3.21	3.38
U	5.74	2.41	3.89	3.43
Pb	34.21	15.61	20.01	18.98
Rb	133.9	51.7	94.2	95.0
Cs	4.68	1.51	2.09	2.42
Sr	37	61	24	26
Sc	0.2	2.7	2.6	1.3
Zr	1418	611	735	791

Table A1 continued.

Sample ID	SI-16-loc33_smp1	SI-16-loc33_smp2	SI-16-loc33_smp3	SI-16-FT-smp1
Sample Type	Pumice	Pumice	Pumice	Pumice
Coordinates	43.0353°, -118.9605°	43.0353°, -118.9605°	43.0353°, -118.9605°	43.0958°, -118.7835°
This Study				
XRF Normalized 100% volatile free, weight %				
SiO_2	75.11	76.01	76.44	68.75
TiO_2	0.253	0.253	0.226	0.580
Al_2O_3	11.75	11.12	11.14	13.63
FeO*	2.75	2.89	2.67	5.35
MnO	0.080	0.088	0.066	0.140
MgO	0.04	0.03	0.01	0.65
CaO	0.54	0.51	0.33	1.62
Na_2O	3.24	2.73	2.91	3.23
K_2O	6.19	6.33	6.20	5.97
P_2O_5	0.044	0.057	0.020	0.074
Pre-normalized Total	96.93	96.78	97.02	94.66
LOI %	2.36	2.78	2.44	4.53
XRF, unnormalized ppm				
Ni	3	2	4	3
Cr	3	3	2	5
Sc	2	2	0	5
V	1	5	2	32
Ba	142	181	62	436
Rb	79	86	96	58
Sr	13	16	6	45
Zr	603	705	770	484
Y	86	101	100	80
Nb	49.5	54.9	55.9	50.7
Ga	25	26	27	26
Cu	5	5	4	10
Zn	143	159	156	167
Pb	20	22	25	18
La	126	125	112	108
Ce	234	239	211	214
Th	9	8	9	6
Nd	103	110	96	102
U	2	2	3	2

Table A2 continued

Sample ID	SI-16-loc33_smp1	SI-16-loc33_smp2	SI-16-loc33_smp3	SI-16-FT-smp1
Sample Type	Pumice	Pumice	Pumice	Pumice
Coordinates	43.0353°, -118.9605°	43.0353°, -118.9605°	43.0353°, -118.9605°	43.0958°, -118.7835°
This Study				
ICP-MS, ppm				
La	132.02	134.73	117.16	118.84
Ce	248.43	247.23	225.93	220.03
Pr	29.09	29.91	27.11	27.62
Nd	109.43	114.46	104.35	107.09
Sm	20.25	22.20	20.88	20.13
Eu	1.01	1.01	0.80	2.49
Gd	17.31	19.32	18.74	17.64
Tb	2.84	3.21	3.13	2.76
Dy	17.14	19.42	19.33	16.37
Ho	3.48	4.02	3.99	3.27
Er	9.79	11.23	11.09	8.83
Tm	1.46	1.67	1.67	1.32
Yb	9.48	10.87	10.84	8.66
Lu	1.53	1.72	1.70	1.48
Ba	149	183	51	448
Th	8.37	9.34	9.68	6.15
Nb	49.36	53.91	55.87	49.66
Yb	87.76	100.35	99.76	80.25
Hf	13.88	15.85	16.96	11.29
Ta	2.81	3.13	3.26	2.63
U	2.83	3.40	3.40	2.06
Pb	18.14	20.54	23.23	17.33
Rb	79.7	86.9	96.6	58.2
Cs	2.07	2.30	2.55	1.34
Sr	13	15	6	46
Sc	1.2	1.1	0.6	4.2
Zr	625	721	790	504

Table A1 Continued

Sample ID	SI-16-FT-60sp	SI-16-60L	SI-16-60D	SI-16-63
Sample Type	Single Pumice	Banded Pumice	Banded Pumice	Composite Pumice
Coordinates	43.0958°, -118.7835°	43.0958°, -118.7846°	43.0958°, -118.7846°	43.0304°, -118.7535°
This Study				
XRF Normalized 100% volatile free, weight %				
SiO_2	76.74	75.52	75.38	72.70
TiO_2	0.192	0.205	0.243	0.353
Al_2O_3	10.71	10.85	11.65	13.66
FeO*	2.71	2.63	2.70	4.56
MnO	0.049	0.040	0.045	0.067
MgO	0.11	0.58	0.88	0.78
CaO	0.21	0.75	0.62	0.67
Na_2O	2.46	3.16	2.39	2.95
K_2O	6.82	6.25	6.08	4.23
P_2O_5	0.000	0.010	0.007	0.030
Pre-normalized Total	96.20	91.52	92.17	92.02
LOI %	3.11	6.76	6.67	7.28
XRF, unnormalized ppm				
Ni	5	2	4	10
Cr	2	2	2	6
Sc	1	1	2	6
V	5	6	8	28
Ba	10	41	86	86
Rb	133	113	92	146
Sr	2	16	19	34
Zr	1153	916	684	1359
Y	133	107	89	172
Nb	76.1	61.8	52.2	98.6
Ga	27	25	26	34
Cu	2	5	6	35
Zn	212	173	149	266
Pb	29	21	17	41
La	90	94	121	72
Ce	185	177	230	166
Th	13	10	8	17
Nd	91	89	108	89
U	4	3	2	6

Table A2 continued

Sample ID	SI-16-FT-60sp	SI-16-60L	SI-16-60D	SI-16-63
Sample Type	Single Pumice	Banded Pumice	Banded Pumice	Composite Pumice
Coordinates	43.0958°, -118.7835°	43.0958°, -118.7846°	43.0958°, -118.7846°	43.0304°, -118.7535°
This Study				
ICP-MS, ppm				
La	94.58	97.33	128.65	74.67
Ce	196.12	189.24	236.67	173.01
Pr	24.68	23.91	28.83	22.53
Nd	96.99	92.90	108.63	92.09
Sm	22.62	20.38	20.53	25.19
Eu	0.72	0.68	0.84	1.00
Gd	22.19	18.91	17.81	26.77
Tb	3.95	3.25	2.89	5.00
Dy	24.94	20.51	17.27	32.52
Ho	5.28	4.26	3.54	6.86
Er	14.69	11.91	9.83	19.62
Tm	2.24	1.80	1.46	3.00
Yb	14.29	11.53	9.50	19.15
Lu	2.27	1.86	1.55	3.04
Ba	7	43	85	84
Th	12.89	10.79	8.87	18.66
Nb	73.78	60.90	50.28	96.21
Yb	134.02	107.95	87.77	174.82
Hf	24.44	19.69	15.24	31.18
Ta	4.49	3.70	2.99	6.08
U	4.92	3.82	2.74	6.02
Pb	27.69	21.80	16.49	39.86
Rb	132.2	114.0	91.7	145.7
Cs	3.54	2.76	1.98	5.65
Sr	3	16	19	35
Sc	0.3	0.7	0.8	5.7
Zr	1163	933	697	1359

Table A1 continued

Sample ID	MS-1990-75	MS-14-8	DC_4_F3	MS-11-JunturaDCT
Sample Type	Bulk Tuff	Bulk Tuff	Single Fiamme	Bulk Tuff
Coordinates	44.2333°, -119.0500°	43.6251°, -117.9913°	43.0816°, -118.8902°	43.7728°, -118.1281°
This Study				
XRF, Normalized 100% volatile free, weight %				
SiO_2	76.97	74.58	76.60	76.62
TiO_2	0.226	0.211	0.166	0.184
Al_2O_3	11.56	11.00	10.54	10.76
FeO*	2.34	2.93	3.08	2.84
MnO	0.040	0.062	0.062	0.056
MgO	0.08	0.09	0.00	0.03
CaO	0.15	2.32	0.17	0.19
Na_2O	3.34	3.77	4.89	3.83
K_2O	5.30	5.01	4.52	5.49
P_2O_5	0.003	0.026	0.000	0.007
Pre-normalized Total	95.71	94.01	98.26	96.21
LOI %	3.47	4.94	0.95	2.93
XRF, unnormalized ppm				
Ni	3	8	4	2
Cr	3	4	1	2
Sc	1	1	0	1
V	3	4	2	1
Ba	100	238	7	20
Rb	115	128	188	146
Sr	12	47	0	3
Zr	948	1132	1592	1254
Y	117	149	201	153
Nb	66.7	80.8	114.7	87.0
Ga	28	27	30	27
Cu	5	4	9	5
Zn	183	222	320	246
Pb	24	32	46	34
La	97	91	79	82
Ce	201	185	179	183
Th	12	14	19	14
Nd	95	96	95	92
U	4	4	7	5

Table A2 continued

Sample ID	MS-1990-75	MS-14-8	DC_4_F3	MS-11-JunturaDCT
Sample Type	Bulk Tuff	Bulk Tuff	Single fiamme	Bulk Tuff
Coordinates	44.2333°, -119.0500°	43.6251°, -117.9913°	43.0816°, -118.8902°	43.7728°, -118.1281°
This Study ICP-MS, ppm				
La	107.15	96.39	82.66	89.67
Ce	210.39	191.98	185.89	189.74
Pr	26.01	25.19	24.48	24.22
Nd	99.51	99.31	98.73	95.00
Sm	21.52	23.85	27.79	23.57
Eu	0.77	0.87	0.71	0.69
Gd	20.05	24.09	29.86	24.30
Tb	3.53	4.29	5.66	4.39
Dy	22.09	27.67	36.82	28.45
Ho	4.60	5.79	7.85	5.98
Er	12.84	16.38	22.41	16.85
Tm	1.94	2.42	3.36	2.57
Yb	12.41	15.48	21.34	16.38
Lu	2.00	2.42	3.32	2.59
Ba	98	239	3	17
Th	11.54	13.85	19.80	14.89
Nb	65.25	78.41	111.56	84.78
Yb	116.05	149.48	203.60	154.70
Hf	20.66	25.23	35.98	27.39
Ta	3.92	4.80	7.05	5.21
U	4.27	5.31	8.22	5.92
Pb	23.67	30.10	44.82	32.74
Rb	113.6	129.0	186.0	146.1
Cs	3.06	3.95	6.05	4.35
Sr	12	48	1	3
Sc	0.5	0.6	0.3	0.2
Zr	953	1146	1561	1253

Table A1 continued

Sample ID	SI-16-HQ1	SI-16-HQ2
Sample Type	Single fiamme	Single fiamme
Coordinates	43.7399°, -118.8173°	43.7399°, -118.8173°
This Study		
XRF, Normalized 100% volatile free, weight %		
SiO_2	76.63	76.47
TiO_2	0.168	0.169
Al_2O_3	10.50	10.53
FeO*	3.12	3.15
MnO	0.061	0.061
MgO	0.00	0.00
CaO	0.16	0.18
Na_2O	4.89	4.97
K_2O	4.49	4.48
P_2O_5	0.000	0.000
Pre-normalized Total	98.79	98.67
LOI %	0.40	0.43
XRF, unnormalized ppm		
Ni	3	4
Cr	4	3
Sc	0	1
V	3	3
Ba	5	5
Rb	188	189
Sr	0	2
Zr	1588	1594
Y	200	201
Nb	113.3	114.2
Ga	31	31
Cu	10	10
Zn	321	322
Pb	46	45
La	78	83
Ce	178	178
Th	19	19
Nd	97	95
U	7	8

Table A2 continued

Sample ID	SI-16-HQ1	SI-16-HQ2
Sample Type	Single Fiamme	Single Fiamme
Coordinates	43.7399°, -118.8173°	43.7399°, -118.8173°
This Study		
ICP-MS, ppm		
La	83.04	82.17
Ce	187.33	185.87
Pr	24.61	24.41
Nd	99.48	99.08
Sm	27.83	27.76
Eu	0.71	0.70
Gd	29.83	30.02
Tb	5.63	5.68
Dy	36.63	36.77
Ho	7.87	7.86
Er	22.05	22.39
Tm	3.32	3.33
Yb	21.05	21.00
Lu	3.28	3.30
Ba	4	3
Th	19.61	19.56
Nb	111.70	111.51
Yb	202.66	204.09
Hf	35.73	35.82
Ta	7.01	7.05
U	8.11	8.15
Pb	44.14	44.38
Rb	185.7	185.7
Cs	6.22	6.06
Sr	3	4
Sc	0.0	0.3
Zr	1565	1563

APPENDIX B – Accessory Phase Compositional Data

Table B1 Group A compositional data for all chevkinite, weight %

Spectrum Label	Site 1; Spectrum 1	Site 1; Spectrum 2	Site 1; Spectrum 3	Site 1; Spectrum 4	Site 1; Spectrum 5	Site 1; Spectrum 7
SiO_2	21.13	21.08	21.74	21.2	21	21.23
TiO_2	19.04	18.84	19.24	19.23	19.04	19.1
Al_2O_3	0.23	0.25	0.17	0.2	0.22	0.2
Fe_2O_3	11.03	10.92	11.12	11.02	11.28	11.64
MnO	0.12	0.27	0.24	0.21	0.02	0.07
MgO	0	0	0	0.01	0	0
CaO	2.76	3.01	3.25	2.82	2.7	3
Na_2O	0.29	0.3	0.4	0.35	0.28	0.38
P_2O_5	0.07	0.16	0.14	0.02	0	0.04
SO_2	0	0	0	0.02	0.02	0
Y_2O_3	0	0	0	0	0	0
Cr_2O_3	0	0.08	0.05	0	0	0
NiO	0	0	0	0.06	0.11	0
Nb_2O_5	0	0	0	0	0	0
La_2O_3	11.84	12.14	11.11	11.91	11.94	11.53
CeO_2	21.79	21.58	21.1	22.04	22.24	21.59
Pr_2O_3	2.18	1.93	2.11	1.95	2.23	2.1
Nd_2O_3	8.14	8.05	8.23	8	8.23	7.97
Sm_2O_3	1.37	1.38	1.12	0.95	0.7	1.15
Eu_2O_3	0	0	0	0	0	0

Table B1 continued

Spectrum Label	Site 1; Spectrum 8	Site 1; Spectrum 9	Site 1; Spectrum 10	Site 1; Spectrum 12	Site 1; Spectrum 13	Site 1; Spectrum 16
SiO_2	21.27	21.08	21.88	21.14	21.32	20.76
TiO_2	19.34	19.29	19.24	18.6	18.67	18.72
Al_2O_3	0.23	0.15	0.2	0.27	0.3	0.26
Fe_2O_3	10.76	11.17	10.97	11.52	11.51	11.58
MnO	0.25	0.28	0.09	0.15	0.14	0.29
MgO	0	0.04	0	0	0.03	0.02
CaO	2.94	2.88	2.95	3.17	3.28	3.15
Na_2O	0.29	0.25	0.31	0.35	0.33	0.26
P_2O_5	0	0.21	0.07	0.09	0.13	0.04
SO_2	0	0	0	0	0	0
Y_2O_3	0	0	0	0	0	0
Cr_2O_3	0	0	0	0	0	0
NiO	0	0	0.02	0	0	0
Nb_2O_5	0	0	0	0	0	0
La_2O_3	11.99	12.07	11.71	12.01	11.64	12.43
CeO_2	21.66	21.45	21.8	21.72	21.78	22.04
Pr_2O_3	1.82	1.98	1.99	2.29	2.29	2.1
Nd_2O_3	7.97	7.83	7.9	7.75	7.84	7.32
Sm_2O_3	1.48	1.31	0.88	0.93	0.74	1.03
Eu_2O_3	0	0	0	0	00	0

Table B1 continued

Spectrum Label	Site 1; Spectrum 17	Site 1; Spectrum 18	Site 1; Spectrum 19	Site 1; Spectrum 20	Site 1; Spectrum 22	Site 1; Spectrum 23
SiO_2	21.21	21.18	23.44	21.26	21.32	21.22
TiO_2	19.45	18.74	17.26	18.46	18.77	19.3
Al_2O_3	0.33	0.28	0.26	0.23	0.21	0.24
Fe_2O_3	11.07	11.28	13.02	11.62	11.84	11.26
MnO	0.24	0.16	0.25	0.14	0.12	0.14
MgO	0	0.42	0	0	0	0.02
CaO	2.92	3.25	4.1	2.92	3.15	2.94
Na_2O	0.36	0.28	0.53	0.32	0.34	0.37
P_2O_5	0.07	0.09	0	0.05	0.14	0.01
SO_2	0	0	0.02	0	0	0.01
Y_2O_3	0	0	0	0	0	0
Cr_2O_3	0	0	0	0	0	0
NiO	0.02	0	0.11	0	0	0
Nb_2O_5	0	0	0	0	0	0
La_2O_3	12.24	11.66	11.04	11.58	11.84	11.84
CeO_2	21.7	21.41	20	21.73	21.6	21.44
Pr_2O_3	1.78	2.36	1.63	2.52	1.99	2.18
Nd_2O_3	7.71	7.7	7.28	7.87	7.91	8.03
Sm_2O_3	0.9	1.16	1.07	1.29	0.77	1.01
Eu_2O_3	0	0	0	0	0	0

Table B1 continued

Spectrum Label	Site 1; Spectrum 26	Site 1; Spectrum 27	Site 1; Spectrum 28	Site 1; Spectrum 33	Site 1; Spectrum 35	Site 1; Spectrum 36
SiO_2	21.83	21.46	21.29	21.08	21.55	21.5
TiO_2	19.04	18.33	19.81	19.16	19.86	19.18
Al_2O_3	0.31	0.37	0.22	0.14	0.16	0.21
Fe_2O_3	10.95	11.71	10.75	10.72	10.95	10.84
MnO	0.24	0.2	0.42	0.27	0.15	0.11
MgO	0	0	0	0	0	0
CaO	3.03	3.13	2.78	2.44	2.86	3.31
Na_2O	0.43	0.39	0.2	0.22	0.18	0.4
P_2O_5	0.08	0	0	0.02	0.12	0.13
SO_2	0	0	0	0	0.01	0
Y_2O_3	0	0	0	0	0	0
Cr_2O_3	0	0	0	0	0	0
NiO	0	0.02	0	0.01	0	0
Nb_2O_5	0	0	0	0	0	0
La_2O_3	12.01	12.34	12.49	12.19	12.08	11.77
CeO_2	20.98	21.89	22.38	22.12	22.67	21.61
Pr_2O_3	2.11	1.95	1.6	1.82	1.69	2.14
Nd_2O_3	7.64	7.27	8.05	8.27	7.73	7.84
Sm_2O_3	1.37	0.95	0	1.55	0	0.97
Eu_2O_3	0	0	0	0	0	0

Table B1 continued

Spectrum Label	Site 1; Spectrum 37	Site 1; Spectrum 38	Site 1; Spectrum 41	Site 1; Spectrum 43	Site 5; Spectrum 85	Site 5; Spectrum 87
SiO_2	21.76	21.79	21.62	21.44	21.1	21.31
TiO_2	19.33	19.31	18.74	18.9	19.13	18.97
Al_2O_3	0.15	0.22	0.18	0.25	0.2	0.14
Fe_2O_3	10.93	10.7	11.73	11.75	11.32	11.67
MnO	0.15	0.22	0.12	0.32	0.23	0.07
MgO	0	0	0	0	0	0
CaO	2.71	2.87	3.43	3.33	2.92	3.02
Na_2O	0.4	0.41	0.31	0.31	0.36	0.39
P_2O_5	0	0.02	0.1	0.1	0.13	0.04
SO_2	0	0	0.01	0	0	0
Y_2O_3	0	0	0	0	0	0
Cr_2O_3	0	0	0	0	0	0
NiO	0	0.21	0	0	0.04	0
Nb_2O_5	0	0	0	0	0	0
La_2O_3	11.88	11.99	11.42	11.69	12.14	12.03
CeO_2	21.98	21.64	21.19	21.14	21.76	21.64
Pr_2O_3	1.81	1.73	2.01	1.7	1.84	1.82
Nd_2O_3	7.89	7.68	8.31	7.94	8.03	7.64
Sm_2O_3	1.02	1.22	0.82	1.13	0.82	1.25
Eu_2O_3	0	0	0	0	0	0

Table B1 continued

Spectrum Label	Site 5; Spectrum 90	Site 6; Spectrum 95	Site 6; Spectrum 97	Site 6; Spectrum 98	Site 6; Spectrum 99	Site 6; Spectrum 100
SiO_2	21.03	21.29	21.12	21.51	20.88	20.9
TiO_2	19.35	19.31	19.09	19.08	19.43	19.38
Al_2O_3	0.24	0.22	0.21	0.14	0.32	0.18
Fe_2O_3	10.29	10.88	10.92	10.82	10.37	10.85
MnO	0.25	0.09	0.19	0.11	0.2	0.13
MgO	0	0	0	0	0	0
CaO	2.8	2.64	3.14	2.56	3.09	2.61
Na_2O	0.31	0.36	0.34	0.36	0.38	0.31
P_2O_5	0.19	0	0.11	0.04	0.1	0.16
SO_2	0	0	0	0	0.03	0.02
Y_2O_3	0	0	0	0	0	0
Cr_2O_3	0	0	0	0	0.03	0
NiO	0	0	0.07	0	0	0.04
Nb_2O_5	0	0	0	0	0	0
La_2O_3	12.6	11.85	11.36	11.03	12.87	12.44
CeO_2	22.14	21.84	21.58	22.16	21.52	22.45
Pr_2O_3	2.06	2.04	2.35	2.47	2	2.04
Nd_2O_3	7.69	8.38	8.12	8.48	7.55	7.62
Sm_2O_3	1.05	1.1	1.37	1.22	1.22	0.88
Eu_2O_3	0	0	0	0	0	0

Table B1 continued

Spectrum Label	Site 6; Spectrum 101	Site 6; Spectrum 102	Site 6; Spectrum 103	Site 6; Spectrum 104	Site 6; Spectrum 105	Site 6; Spectrum 106
SiO_2	21.07	20.67	21.8	20.36	21.03	20.85
TiO_2	19.13	19.11	18.37	18.76	18.7	19.09
Al_2O_3	0.19	0.24	0.28	0.24	0.18	0.25
Fe_2O_3	10.58	11.7	11.29	11.76	10.99	11.13
MnO	0.25	0.18	0.25	0.14	0.35	0.13
MgO	0	0	0	0	0	0
CaO	2.69	2.94	2.77	2.72	2.72	2.73
Na_2O	0.26	0.27	0.3	0.3	0.41	0.35
P_2O_5	0.16	0.01	0	0	0.16	0
SO_2	0	0	0.05	0	0.05	0
Y_2O_3	0	0	0	0	0	0
Cr_2O_3	0.19	0	0	0	0	0
NiO	0	0	0.04	0.02	0	0.16
Nb_2O_5	0	0	0	0	0	0
La_2O_3	12.19	11.96	12.34	12.67	12.04	12.34
CeO_2	21.98	21.86	21.84	21.9	21.88	22.3
Pr_2O_3	2.08	1.94	1.97	2.03	2.1	2.12
Nd_2O_3	8.07	8.18	7.68	8.06	8.21	7.59
Sm_2O_3	1.16	0.94	1.01	1.03	1.2	0.98
Eu_2O_3	0	0	0	0	0	0

Table B1 continued

Spectrum Label	Site 6; Spectrum 107	Site 15; Spectrum 158	Site 15; Spectrum 159	Site 15; Spectrum 160	Site 15; Spectrum 162	Site 15; Spectrum 164
SiO_2	20.81	21.04	21.09	21.09	8.05	21.37
TiO_2	19.43	19.47	19.6	19.86	22.61	19.34
Al_2O_3	0.25	0.23	0.31	0.2	2.27	0.18
Fe_2O_3	11.24	10.29	10.72	10.44	11.84	10.85
MnO	0.09	0.29	0.06	0.21	0.39	0.07
MgO	0	0	0	0	0.06	0
CaO	2.55	2.79	2.93	2.92	3.1	3.08
Na_2O	0.3	0.29	0.34	0.33	0.23	0.29
P_2O_5	0.02	0.11	0.2	0.16	0.07	0.2
SO_2	0	0.01	0	0	0.04	0
Y_2O_3	0	0	0	0	0	0
Cr_2O_3	0	0	0	0	0	0
NiO	0.04	0.02	0.08	0.02	0	0.01
Nb_2O_5	0	0	0	0	0	0
La_2O_3	12.36	13.5	11.92	13.18	14.21	12.45
CeO_2	22.16	22.16	21.68	21.83	25.99	21.87
Pr_2O_3	1.45	1.93	2.14	1.71	1.19	1.55
Nd_2O_3	8.12	7.14	7.8	7.2	8.78	7.72
Sm_2O_3	1.17	0.72	1.13	0.86	1.16	1.02
Eu_2O_3	0	0	0	0	0	0

Table B1 continued

Spectrum Label	Site 15; Spectrum 166	Site 19; Spectrum 159	Site 19; Spectrum 160	Site 19; Spectrum 161	Site 19; Spectrum 162	Site 19; Spectrum 163
SiO_2	20.71	17.3	17.68	17.27	47.15	13.65
TiO_2	19.46	20.89	20.96	20.17	0.42	20.62
Al_2O_3	0.18	0	0	0.23	0	0.33
Fe_2O_3	10.83	10.59	11.11	11.59	30.37	11.66
MgO	0	0	0	0	0	0
CaO	2.5	3.14	3.19	3.32	19.22	3.35
Na_2O	0.24	0	0	0	0.62	0
P_2O_5	0.08	0.06	0.13	0.11	0	0.17
SO_2	0.07	0	0	0	0	0
Y_2O_3	0	0	0	0	0	0
Cr_2O_3	0	0	0	0	0	0
NiO	0	0	0	0	0	0
Nb_2O_5	0	0	0	0	0	0
La_2O_3	12.99	13.75	12.64	13.06	0	14.49
CeO_2	22.16	22.88	23.23	22.76	0	24.32
Pr_2O_3	1.82	2.23	2.27	2.23	0.17	2.39
Nd_2O_3	7.87	7.65	7.91	8.17	0.44	7.34
Sm_2O_3	0.86	1.18	0.87	0.91	0.08	1.24
Eu_2O_3	0	0	0	0	0.28	0.21

Table B1 continued

Spectrum Label	Site 19; Spectrum 164	Site 19; Spectrum 165	Site 19; Spectrum 167	Site 19; Spectrum 168	Site 19; Spectrum 169	Site 19; Spectrum 170	Site 19; Spectrum 171
SiO_2	19.71	20.43	16.93	16.64	16.92	17.24	20.3
TiO_2	19.56	20.35	20.63	20.33	20.27	20.56	19.88
Al_2O_3	0.7	0.57	0	0	0	0	1.24
Fe_2O_3	11	10.26	11.02	11.09	10.54	10.62	10.92
MgO	0	0	0	0	0	0	0
CaO	3.68	3.37	3.1	3.01	2.95	2.72	3.55
Na_2O	0	0	0	0	0	0	0
P_2O_5	0.48	0.09	0	0.09	0.02	0.13	0.11
SO_2	0	0	0	0	0	0	0
Y_2O_3	0	0	0	0	1.02	0	0
Cr_2O_3	0	0	0	0	0	0	0
NiO	0	0	0	0	0	0	0
Nb_2O_5	0	0	0	0	0	0	0
La_2O_3	13.19	13.29	13.47	13.82	12.89	12.86	12.38
CeO_2	21.63	21.11	23.18	23.12	22.64	23.18	21.24
Pr_2O_3	1.39	1.57	1.95	2.43	2.11	2.21	1.23
Nd_2O_3	7.18	7.08	8.3	7.96	7.49	8.04	7.45
Sm_2O_3	0.84	1.31	0.87	1.05	1.3	1.37	0.98
Eu_2O_3	0.63	0.58	0.51	0.44	0.19	0.53	0.52

Table B2 Group B compositional data for all chevkinite, weight %

Spectrum Label	Site 11; Spectrum 39	Site 11; Spectrum 40	Site 11; Spectrum 45	Site 22; Spectrum 183
SiO_2	25.2	20.25	20.83	17.42
TiO_2	17.46	18.68	19.18	20.63
Al_2O_3	0	0	0	0
Fe_2O_3	12.94	12.7	11.91	11.71
MnO	0	0	0	0
MgO	0	0	0	0
CaO	3.62	2.98	2.93	3.8
Na_2O	0.91	0	0	0
P_2O_5	0	0	0	0
SO_2	0	0	0	0
Y_2O_3	0	0	0	0
Cr_2O_3	0	0	0	0
NiO	0	0	0	0
Nb_2O_5	0	0	0.69	0
La_2O_3	10.5	12.33	12.42	14.14
CeO_2	20.28	22.91	22.36	22.96
Pr_2O_3	1.89	2.12	1.66	2.25
Nd_2O_3	7.21	8.03	8.02	6.31
Sm_2O_3	0	0	0	0.71
Eu_2O_3	0	0	0	0.06

Table B2 continued

Spectrum Label	Site 22; Spectrum 184	Site 22; Spectrum 185	Site 22; Spectrum 186
SiO_2	16.92	18.68	16.8
TiO_2	20.3	19.88	20.85
Al_2O_3	0	0.33	0.25
Fe_2O_3	11.19	10.6	11.05
MnO	0	0	0
MgO	0	0	0
CaO	3.05	3.21	3.44
Na_2O	0	0	0
P_2O_5	0.16	0.21	0.09
SO_2	0	0	0
Y_2O_3	0	0	0
Cr_2O_3	0	0	0
NiO	0	0	0
Nb_2O_5	0	0	0
La_2O_3	14.07	13.79	14.17
CeO_2	22.94	21.72	22.66
Pr_2O_3	2.34	2.33	1.89
Nd_2O_3	7.21	7.05	7.41
Sm_2O_3	1.24	1.01	1.07
Eu_2O_3	0.57	0.59	0.31

Table B2 continued

Spectrum Label	Site 22; Spectrum 188	Site 22; Spectrum 189	Site 23; Spectrum 193	Site 24; Spectrum 197
SiO_2	15.97	17.98	16.22	16.94
TiO_2	20.42	21.29	20.7	20.71
Al_2O_3	0.32	0	0	0
Fe_2O_3	11.01	10.98	11.34	11.27
MnO	0	0	0	0
MgO	0	0	0	0
CaO	3.42	3.6	3.49	3.29
Na_2O	0	0	0	0
P_2O_5	0.2	0.2	0.12	0.12
SO_2	0	0	0	0
Y_2O_3	0	0	0	0
Cr_2O_3	0	0	0	0
NiO	0	0	0	0
Nb_2O_5	0	0	0	0
La_2O_3	13.73	14.7	12.63	12.93
CeO_2	22.19	22.7	22.78	23.53
Pr_2O_3	2.11	1.23	2.06	2.42
Nd_2O_3	7.4	6.73	8.28	7.69
Sm_2O_3	1.55	0.19	1.62	1.1
Eu_2O_3	0.87	0.38	0.61	0

Table B2 continued

Spectrum Label	Site 24; Spectrum 198	Site 24; Spectrum 201	Site 24; Spectrum 202	Site 24; Spectrum 203
SiO_2	18.51	17.39	16.85	17.64
TiO_2	19.77	21.05	20.65	20.2
Al_2O_3	0	0	0	0
Fe_2O_3	11.43	10.47	11.2	10.69
MnO	0	0	0	0
MgO	0	0	0	0
CaO	2.67	2.97	2.66	2.8
Na_2O	0	0	0	0
P_2O_5	0	0	0	0.02
SO_2	0	0	0	0
Y_2O_3	0	0	0	0
Cr_2O_3	0	0	0	0
NiO	0	0	0	0
Nb_2O_5	0	0	0	0
La_2O_3	12.23	14.14	13.81	12.52
CeO_2	23.16	23.13	23.64	22.59
Pr_2O_3	2.56	1.53	1.81	2.3
Nd_2O_3	8.31	7.6	8.18	8.46
Sm_2O_3	0.95	0.83	1.17	1.31
Eu_2O_3	0.42	0.74	0	1.02

Table B3 Group C compositional data for all chevkinite, weight %

Spectrum Label	Site 10; Spectrum 125	Site 10; Spectrum 126	Site 11; Spectrum 131	Site 11; Spectrum 133	Site 11; Spectrum 134
SiO_2	19.7	20.32	20.02	19.59	20.08
TiO_2	19.43	19.09	19.71	19.36	19.15
Al_2O_3	0.15	0.22	0.29	0.25	0.26
Fe_2O_3	11.22	11.59	10.97	11.52	12.04
MnO	0.27	0.08	0.28	0.07	0.24
MgO	0	0.01	0.01	0	0
CaO	2.88	2.79	3.27	2.89	3
Na_2O	0.31	0.33	0.31	0.36	0.33
P_2O_5	0.19	0	0.23	0.16	0.15
SO_2	0	0.08	0.02	0	0
Y_2O_3	0	0	0	0	0
Cr_2O_3	0	0	0	0	0.04
NiO	0.06	0.05	0	0	0.09
Nb_2O_5	0	0	0	0	0
La_2O_3	13.36	12.04	12.98	13.45	11.93
CeO_2	22.34	22.05	21.61	22.05	21.76
Pr_2O_3	1.85	2.33	1.92	2.13	1.82
Nd_2O_3	7.6	8.02	7.72	7.2	7.89
Sm_2O_3	0.65	1	0.66	0.94	1.22
Eu_2O_3	0	0	0	0	0

Table B3 continued

Spectrum Label	Site 13; Spectrum 142	Site 13; Spectrum 143	Site 13; Spectrum 145	Site 13; Spectrum 146	Site 13; Spectrum 148
SiO_2	20.28	19.71	19.87	20.21	19.83
TiO_2	19.62	19.79	19.82	19.54	19.79
Al_2O_3	0.3	0.25	0.17	0.23	0.22
Fe_2O_3	11.2	11.96	10.84	10.96	10.89
MnO	0.21	0.29	0.2	0.14	0.13
MgO	0	0	0	0	0
CaO	2.82	2.93	2.95	2.89	3.02
Na_2O	0.33	0.22	0.27	0.36	0.27
P_2O_5	0.18	0.11	0.1	0.14	0.16
SO_2	0	0	0.01	0	0
Y_2O_3	0	0	0	0	0
Cr_2O_3	0	0	0	0	0
NiO	0.06	0.15	0.08	0	0
Nb_2O_5	0	0	0	0	0
La_2O_3	12.03	12.42	13.83	12.52	12.21
CeO_2	21.7	22.27	21.94	22.28	22.14
Pr_2O_3	1.91	1.61	1.69	1.92	2.33
Nd_2O_3	8.06	8.29	7.46	8.13	7.87
Sm_2O_3	1.29	0	0.76	0.69	1.15
Eu_2O_3	0	0	0	0	0

Table B3 continued

Spectrum Label	Site 13; Spectrum 150	Site 13; Spectrum 152	Site 13; Spectrum 154	Site 14; Spectrum 155	Site 14; Spectrum 156	Site 8; Spectrum 24
SiO_2	19.39	20.66	19.95	20.07	20.28	19.15
TiO_2	19.72	19.54	19.59	19.18	19.35	18.76
Al_2O_3	0.27	0.26	0.29	0.55	0.32	0
Fe_2O_3	10.97	10.8	11.03	11.4	11.3	11.54
MnO	0.02	0.19	0.15	0.17	0.14	0
MgO	0	0.04	0	0	0	0
CaO	2.72	2.77	2.77	2.9	2.68	2.4
Na_2O	0.29	0.38	0.29	0.25	0.34	0
P_2O_5	0.07	0.19	0.08	0	0.05	0
SO_2	0.08	0.02	0	0	0	0
Y_2O_3	0	0	0	0	0	0
Cr_2O_3	0	0	0	0	0	0
NiO	0	0.04	0.14	0.31	0	0
Nb_2O_5	0	0	0	0	0	0
La_2O_3	13.3	13.44	12.73	11.88	12.09	12.71
CeO_2	22.64	21.74	22.4	21.85	22.25	22.86
Pr_2O_3	2.06	1.74	1.99	2	2.03	2.46
Nd_2O_3	7.76	7.44	7.68	7.99	7.93	8.7
Sm_2O_3	0.7	0.75	0.92	1.46	1.23	1.43
Eu_2O_3	0	0	0	0	0	0

Table B4 Group D compositional data for all chevkinite, weight %

Spectrum Label	Site 8; Spectrum 25	Site 27; Spectrum 225	Site 27; Spectrum 227	Site 27; Spectrum 229	Site 27; Spectrum 231	Site 27; Spectrum 232
SiO_2	19.74	16.36	17.81	17.21	16.77	17.34
TiO_2	19.78	20.31	20.79	20.97	20.32	20.01
Al_2O_3	0	0.23	0	0	0	0.19
Fe_2O_3	12.13	11.61	11.1	10.75	10.75	11.04
MnO	0	0	0	0	0	0
MgO	0	0	0	0	0	0
CaO	3.04	2.86	3.19	3.34	2.84	2.93
Na_2O	0	0	0	0	0	0
P_2O_5	0	0.11	0.02	0.17	0	0.17
SO_2	0	0	0	0	0	0
Y_2O_3	0	0	0	0	0	0.69
Cr_2O_3	0	0	0	0	0	0
NiO	0	0	0	0	0	0
Nb_2O_5	0	0	0	0	0	0
La_2O_3	11.85	12.23	12.42	14.03	12.97	11.84
CeO_2	21.98	22.57	23.11	23.18	23.05	23.09
Pr_2O_3	2	2.45	2.26	2.21	2.74	2.41
Nd_2O_3	8.25	8.44	8.17	7.79	8.05	8.36
Sm_2O_3	1.23	1.78	1.13	0.35	1.48	1.3
Eu_2O_3	0	0.42	0	0	0.74	0

Table B4 continued

Spectrum Label	Site 27; Spectrum 234	Site 27; Spectrum 236	Site 35; Spectrum 275	Site 35; Spectrum 276	Site 35; Spectrum 277
SiO_2	18.84	17.58	16.84	16.95	16.54
TiO_2	20.18	20.72	20.15	21.14	20.74
Al_2O_3	0.79	0	0.25	0.24	0
Fe_2O_3	11.49	10.81	10.82	10.69	11.19
MnO	0	0	0	0	0
MgO	0	0	0	0	0
CaO	3.25	3.73	3.01	3.3	3.21
Na_2O	0	0	0	0	0
P_2O_5	0.13	0.15	0.15	0.16	0.01
SO_2	0	0	0	0	0
Y_2O_3	0	0	0	0	0
Cr_2O_3	0	0	0	0	0
NiO	0	0	0	0	0
Nb_2O_5	0	0	0	0	0
La_2O_3	13.12	13.57	14.21	13.61	14.12
CeO_2	21.68	22.2	22.96	22.82	23.4
Pr_2O_3	1.92	2.02	1.89	2.52	2.37
Nd_2O_3	7.29	7.6	7.78	6.96	7.76
Sm_2O_3	1.11	1.01	1.02	1.25	0.56
Eu_2O_3	0	0.62	0.47	0.37	0.01

Table B4 continued

Spectrum Label	Site 35; Spectrum 280	Site 35; Spectrum 281	Site 26; Spectrum 212	Site 26; Spectrum 213	Site 26; Spectrum 216	Site 26; Spectrum 218
SiO_2	17.09	16.65	16.67	16.61	16.82	17.86
TiO_2	20.8	20.71	20.79	21.13	20.93	20.82
Al_2O_3	0	0.27	0	0	0	0
Fe_2O_3	11.16	10.95	10.39	10.58	10.69	11.34
MnO	0	0	0	0	0	0
MgO	0	0	0	0	0	0
CaO	2.8	2.77	2.81	3.37	2.99	3.25
Na_2O	0	0	0	0	0	0
P_2O_5	0	0.1	0.16	0.18	0	0.14
SO_2	0	0	0	0	0	0
Y_2O_3	0	0	0	0	0	0
Cr_2O_3	0	0	0	0	0	0
NiO	0	0	0	0	0	0
Nb_2O_5	0	0	0	0	0	0
La_2O_3	12.77	12.91	14.21	13.73	13.29	12.44
CeO_2	23.48	23.4	23.31	22.82	23.21	23.17
Pr_2O_3	2.03	2.16	1.83	1.73	2.27	2.35
Nd_2O_3	8.39	8.27	7.98	7.63	7.93	7.52
Sm_2O_3	1.25	1.37	1.28	1.35	0.99	1.11
Eu_2O_3	0	0.37	0.5	0.65	0.71	0

Table B4 continued

Spectrum Label	Site 26; Spectrum 219	Site 26; Spectrum 221	Site 26; Spectrum 222	Site 32; Spectrum 247	Site 32; Spectrum 248
SiO_2	17.81	17	18.9	18.12	17.08
TiO_2	20.94	20.52	19.99	21.54	20.4
Al_2O_3	0	0	0	0	0.24
Fe_2O_3	11.63	10.56	10.77	10.9	10.54
MnO	0	0	0	0	0
MgO	0	0	0	0	0
CaO	3.9	3.1	3.24	3.56	3
Na_2O	0	0	0	0	0
P_2O_5	0.2	0.16	0.13	0.14	0.18
SO_2	0	0	0	0	0
Y_2O_3	0	0	0	0	0
Cr_2O_3	0	0	0	0	0
NiO	0	0	0	0	0
Nb_2O_5	0	0	0	0	0
La_2O_3	12.02	12.98	13.07	12.49	13.26
CeO_2	21.97	22.68	21.89	22.58	23.03
Pr_2O_3	1.78	2.42	2.53	1.94	2.8
Nd_2O_3	7.75	8.51	7.92	7.99	7.97
Sm_2O_3	1.36	1.36	1.33	0.67	1.02
Eu_2O_3	0.27	0.26	0.14	0.07	0.45

Table B5 Group E compositional data for all chevkinite, weight %

Spectrum Label	Site 13; Spectrum 81	Site 13; Spectrum 85	Site 13; Spectrum 89	Site 13; Spectrum 91	Site 13; Spectrum 93
SiO_2	17.12	18.08	17.86	17.6	16.68
TiO_2	20.7	20.52	21.02	20.94	21.3
Al_2O_3	0.22	0.3	0	0.25	0
Fe_2O_3	9.89	10.75	10.65	10.67	10.91
MnO	0	0	0	0	0
MgO	0	0	0	0	0
CaO	3.16	2.93	3.34	3.35	3.47
Na_2O	0	0	0	0	0
P_2O_5	0.22	0	0	0	0
SO_2	0	0	0	0	0
Y_2O_3	0	0	0	0	0
Cr_2O_3	0	0	0	0	0
NiO	0	0	0	0	0
Nb_2O_5	0	0	0	0	0
La_2O_3	14.21	13.26	13.07	13	13.75
CeO_2	22.9	23.48	22.58	22.27	23.11
Pr_2O_3	1.87	1.93	2.24	2.23	2.22
Nd_2O_3	7.32	7.8	7.56	8.13	7.4
Sm_2O_3	0.98	0.67	1.35	1.11	1.09
Eu_2O_3	0.78	0.27	0.19	0.12	0.09

Table B5 Group E compositional data for all chevkinite, weight %

Spectrum Label	Site 13; Spectrum 95	Site 15; Spectrum 117	Site 15; Spectrum 121	Site 15; Spectrum 125	Site 15; Spectrum 127
SiO_2	14.69	17.63	17.1	17.82	17.23
TiO_2	20.78	21.11	20.74	20.83	20.58
Al_2O_3	0.25	0.31	0.19	0	0
Fe_2O_3	11.23	10.52	11.3	10.72	10.3
MnO	0	0	0	0	0
MgO	0	0	0	0	0
CaO	3.05	3.87	3.33	3.07	3.28
Na_2O	0	0	0	0	0
P_2O_5	0	0.2	0.08	0.04	0.07
SO_2	0	0	0	0	0
Y_2O_3	0	0	0	0	0
Cr_2O_3	0	0	0	0	0
NiO	0	0	0	0	0
Nb_2O_5	0	0	0	0	0
La_2O_3	13.65	13.04	14.15	12.76	12.45
CeO_2	24.28	22.25	23	23.46	22.26
Pr_2O_3	2.84	1.95	1.94	2.12	2.27
Nd_2O_3	7.97	7.23	7.38	7.4	8.41
Sm_2O_3	0.9	1.28	0.47	1.25	1.73
Eu_2O_3	0.36	0.49	0.06	0	0.41

Table B5 continued

Spectrum Label	Site 18; Spectrum 153	Site 18; Spectrum 154	Site 18; Spectrum 155	Site 14; Spectrum 105	Site 14; Spectrum 106
SiO_2	17.43	17.62	17.19	18.2	17.51
TiO_2	20.16	20.17	21.2	20.47	20.2
Al_2O_3	0.23	0	0.3	0.27	0.19
Fe_2O_3	10.63	11.58	11.32	10.95	10.77
MnO	0	0	0	0	0
MgO	0	0	0	0	0
CaO	2.69	2.99	3.32	2.93	3.14
Na_2O	0	0	0	0.03	0.06
P_2O_5	0.08	0.07	0.06		0.13
SO_2	0	0	0	0	0
Y_2O_3	0	0	0	0	0
Cr_2O_3	0	0	0	0	0
NiO	0	0	0	0	0
Nb_2O_5	0	0	0.53	0	0.3
La_2O_3	13.24	12.86	12.64	13.11	13.3
CeO_2	22.75	23.02	22.91	22.95	22.61
Pr_2O_3	2.02	2.25	1.97	1.93	2.28
Nd_2O_3	8.6	8.17	7.7	7.5	7.85
Sm_2O_3	0.9	0.9	0.85	1.25	1.09

Table B5 continued

Spectrum Label	Site 18; Spectrum 147	Site 18; Spectrum 149	Site 18; Spectrum 150	Site 18; Spectrum 151	Site 18; Spectrum 152
SiO_2	16.76	17.14	16.84	17.35	17.32
TiO_2	21.78	20.64	20.73	20.78	20.25
Al_2O_3	0	0.28	0	0	0.56
Fe_2O_3	11.25	10.33	10.99	10.79	11.46
MnO	0	0	0	0	0
MgO	0	0	0	0	0
CaO	2.88	2.93	3.24	3.17	3.57
Na_2O	0	0	0	0	0
P_2O_5	0.11	0.1	0.06	0.03	0.02
SO_2	0	0	0	0	0
Y_2O_3	0	0	0	0	0
Cr_2O_3	0	0	0	0	0
NiO	0	0	0	0	0
Nb_2O_5	0	0	0	0	0
La_2O_3	13.08	13.81	14.17	12.08	12.09
CeO_2	22.5	23.3	23.13	23.38	22.21
Pr_2O_3	2.03	2.17	2.44	2.77	2.07
Nd_2O_3	8.05	7.85	7.62	8.47	8.22
Sm_2O_3	1.09	0.98	0.55	1.17	1.59

Table B5 continued

Spectrum Label	Site 14; Spectrum 108	Site 14; Spectrum 109	Site 14; Spectrum 110	Site 14; Spectrum 111	Site 14; Spectrum 115
SiO_2	16.71	17.33	17.14	17.99	17.75
TiO_2	20.96	20.29	20.07	20.02	20.4
Al_2O_3	1.18	0.19	0.13	0.33	0.19
Fe_2O_3	11.4	11.27	11.68	11.32	11.54
MnO	0	0	0	0	0
MgO	0	0	0	0	0
CaO	3.24	3.18	3.25	3.2	3.76
Na_2O	0	0.04	0	0	0
P_2O_5	0.02	0.2	0	0.13	0.07
SO_2	0	0	0	0	0
Y_2O_3	0	0	0	0	0
Cr_2O_3	0	0	0	0	0
NiO	0	0	0	0	0
Nb_2O_5	0.23	0.52	0.2	0.5	0.43
La_2O_3	13.07	14.07	12.56	12.28	12.26
CeO_2	22.24	23.31	23.12	21.95	22.75
Pr_2O_3	1.63	1.73	2.15	1.96	2.12
Nd_2O_3	7.98	7.28	8.19	8.33	7.92
Sm_2O_3	0.89	0.58	1.07	1.58	0.81
Eu_2O_3	0.18	0	0.3	0.17	0

Table B5 continued

Spectrum Label	Site 16; Spectrum 129	Site 16; Spectrum 130	Site 16; Spectrum 131	Site 16; Spectrum 132	Site 16; Spectrum 133
SiO_2	16.98	20.02	17.27	16.57	17.79
TiO_2	20.24	20.41	21.03	20.12	21.02
Al_2O_3	0	0.51	0	0	0
Fe_2O_3	10.51	10.95	11.28	10.38	10.94
MnO	0	0	0	0	0
MgO	0	0	0	0	0
CaO	2.85	2.82	2.95	3.02	3.07
Na_2O	0	0	0	0	0
P_2O_5	0.07	0	0	0.06	0
SO_2	0	0	0	0	0
Y_2O_3	0	0	0	0	0
Cr_2O_3	0	0	0	0	0
NiO	0	0	0	0	0
Nb_2O_5	0.26	0.17	0.26	0.2	0.38
La_2O_3	13.96	12.09	12.76	14.3	12.29
CeO_2	23.28	21.02	22.81	23.18	22.93
Pr_2O_3	2.4	2.28	2.38	1.86	2.52
Nd_2O_3	7.68	7.65	8.22	7.58	8.35
Sm_2O_3	0.98	1.57	1.04	1.21	0.57
Eu_2O_3	0.42	0.52	0	0.79	0

Table B6 Group A compositional data for all Ce-rich chevkinite, weight %

Spectrum Label	Site 1; Spectrum 29	Site 1; Spectrum 34	Site 5; Spectrum 83	Site 5; Spectrum 94	Site 15; Spectrum 165	Site 2; Spectrum 47
SiO_2	24.55	24.53	24.74	45.24	33.22	30.97
TiO_2	18.29	18.53	18.32	0	0	0
Al_2O_3	0.23	0.31	0.18	0.57	0.45	0.33
Fe_2O_3	12.79	12.44	13.21	14.39	16.35	15.85
MnO	0	0	0	0.69	0	0
MgO	0	0	0	1.56	0	0
CaO	2.95	3.13	3.25	17.36	5.05	4.19
Na_2O	0.1	0.14	0.04	7.41	0.63	0.56
P_2O_5	0	0	0.03	1.06	0.04	0.21
SO_2	0.01	0.01	0	5.37	0.03	0
Y_2O_3	0.75	0.75	0.62	0	1.34	1.71
Cr_2O_3	0	0	0.16	0.12	0.1	0
NiO	0	0	0	0	0	0
Nb_2O_5	0	0	0	0	0	0
La_2O_3	0	0	0	0	0	0
CeO_2	23.95	23.53	23.71	0	24.43	27.09
Pr_2O_3	6.21	6.07	6.12	0	7.43	8.12
Nd_2O_3	8.11	8.59	8.01	0	8.62	8.77
Sm_2O_3	2.08	1.96	1.63	0	2.32	2.2
Eu_2O_3	0	0	0	0	0	0

Table B7 Group A compositional data for all ilmenite, weight %

Spectrum Label	Site 1; Spectrum 6	Site 1; Spectrum 11	Site 1; Spectrum 14	Site 1; Spectrum 15	Site 1; Spectrum 21
SiO_2	0.13	0.03	0.08	0.1	0.09
TiO_2	51.74	52.5	52.21	52.03	52.23
Al_2O_3	0.11	0.12	0.13	0.1	0.09
Fe_2O_3	46.11	45.58	45.85	46.04	45.8
MnO	1.51	1.4	1.49	1.53	1.51
MgO	0.01	0.01	0.1	0.05	0.04
CaO	0.14	0.15	0.07	0.02	0.02
Na_2O	0.09	0.07	0.05	0.06	0.06
P_2O_5	0.05	0.01	0.02	0.04	0.02
SO_2	0.04	0	0	0	0.03
Cr_2O_3	0.07	0.05	0	0.03	0.04
NiO	0	0.09	0	0	0.07

Table B7 continued

Spectrum Label	Site 1; Spectrum 30	Site 1; Spectrum 31	Site 1; Spectrum 32	Site 3; Spectrum 57	Site 3; Spectrum 58
SiO_2	0.03	0.06	0.26	0.11	0.06
TiO_2	52.23	52.12		52.26	52.26
Al_2O_3	0.07	0.08	0.06	0.13	0.13
Fe_2O_3	45.96	46.04	95.99	45.72	45.74
MnO	1.5	1.4	3.15	1.58	1.57
MgO	0.06	0.01	0.11	0	0.07
CaO	0.03	0.04	0	0.11	0
Na_2O	0.03	0.08	0.21	0.06	0.05
P_2O_5	0.09	0.06	0		0.08
SO_2	0	0	0		0
Cr_2O_3	0	0	0.04	0	0
NiO	0	0.1	0.18	0.04	0.05

Table B7 continued

Spectrum Label	Site 3; Spectrum 59	Site 3; Spectrum 61	Site 3; Spectrum 62	Site 3; Spectrum 63	Site 3; Spectrum 64
SiO_2	0.04	0.12	0.11	0.09	0.09
TiO_2	52.42	52.34	52.18	52.29	52.48
Al_2O_3	0.09	0.05	0.08	0.07	0.1
Fe_2O_3	45.63	45.68	46	45.81	45.58
MnO	1.52	1.5	1.51	1.4	1.43
MgO	0.03	0.05	0.03	0.04	0.03
CaO	0.08	0.01	0	0.03	0.04
Na_2O	0.06	0.14	0.06	0.12	0.02
P_2O_5	0.04	0.08	0	0	0.03
SO_2	0	0	0.02	0	0
Cr_2O_3	0	0.01	0.01	0.1	0
NiO	0.09	0.02	0	0.06	0.19

Table B7 continued

Spectrum Label	Site 3; Spectrum 65	Site 3; Spectrum 66	Site 4; Spectrum 73	Site 4; Spectrum 78	Site 4; Spectrum 81
SiO_2	0.17	0.18	0.12	0.04	1.86
TiO_2	51.38	51.74	52.41	52.15	
Al_2O_3	0.07	0.29	0.16	0.08	0.32
Fe_2O_3	46.27	45.83	45.58	45.92	94.74
MnO	1.56	1.46	1.5	1.57	0.14
MgO	0.07	0.08	0.05	0.07	0.29
CaO	0.32	0.1	0.02	0.07	0.96
Na_2O	0.06	0.19	0.02	0.09	0
P_2O_5	0.07	0.07	0.02	0	0.52
SO_2	0	0.04	0.01	0	0.97
Cr_2O_3	0.03	0	0.03	0.01	0
NiO	0	0.01	0.09	0	0.2

Table B7 continued

Spectrum Label	Site 5; Spectrum 88	Site 5; Spectrum 89	Site 5; Spectrum 91	Site 5; Spectrum 93	Site 6; Spectrum 96	Site 15; Spectrum 163
SiO_2	0.15	0.17	0.06	0.13	0.02	0.1
TiO_2	52.46	52.28	52.33	51.95	52.23	51.91
Al_2O_3	0.1	0.07	0.09	0.13	0.17	0.08
Fe_2O_3	45.4	45.6	45.81	45.85	46.05	45.96
MnO	1.61	1.57	1.46	1.57	1.37	1.56
MgO	0.04	0.09	0.04	0.01	0.03	0.12
CaO	0	0	0	0.21	0.05	0.09
Na_2O	0.07	0.07	0.14	0.06	0.03	0.07
P_2O_5	0	0.05	0.04	0.03	0	0.04
SO_2	0.01	0	0	0	0	0.01
Cr_2O_3	0.05	0	0.03	0.05	0.01	0
NiO	0.1	0.09	0.01	0	0.04	0.05

Table B8 Group B compositional data for all ilmenite, weight %

Spectrum Label	Site 11; Spectrum 42	Site 24; Spectrum 200	Site 24; Spectrum 204	Site 22; Spectrum 182	Site 22; Spectrum 187
SiO_2	0	0	0	0	0
TiO_2	50.31	52.96	53.01	52.37	52.7
Al_2O_3	0	0	0	0	0
Fe_2O_3	46.69	44.92	44.81	45.77	45.3
MnO	1.73	1.74	1.66	1.79	1.5
MgO	0	0	0	0	0
CaO	0.4	0	0	0	0.16
Na_2O	0	0	0	0	0
P_2O_5	0.43	0	0	0	0.06
SO_2	0	0	0	0	0
Cr_2O_3	0	0	0	0	0
NiO	0	0	0	0	0

Table B9 Group C compositional data for all ilmenite, weight %

Spectrum Label	Site 10; Spectrum 121	Site 10; Spectrum 122	Site 10; Spectrum 123	Site 10; Spectrum 124	Site 10; Spectrum 127
SiO_2	0.43	0.05	0.17	4.89	0.13
TiO_2	51.02	51.17	50.76	48.79	50.9
Al_2O_3	0.1	0.1	0.08	0.16	0.07
Fe_2O_3	46.6	46.76	47.19	43.97	46.92
MnO	1.53	1.55	1.55	1.12	1.64
MgO	0.07	0.04	0.05	0.01	0
CaO	0.06	0.08	0.07	0.77	0.14
Na_2O	0.07	0.07	0.09	0.06	0.11
P_2O_5	0.11	0.09	0.01	0.08	0.01
SO_2	0.01	0	0	0	0
Cr_2O_3	0	0	0	0	0.02
NiO	0	0.09	0.03	0.15	0.07

Table B9 continued

Spectrum Label	Site 10; Spectrum 128	Site 11; Spectrum 135	Site 12; Spectrum 136	Site 12; Spectrum 137	Site 12; Spectrum 138	Site 12; Spectrum 139
SiO_2	0.09	0.14	1.21	0.99	0.09	1.03
TiO_2	51.08	51.25	37.81	8.81	35.63	2.35
Al_2O_3	0.07	0.14	0.52	1.72	0.53	3.09
Fe_2O_3	47.05	46.8	56.93	84.65	60.95	90.14
MnO	1.43	1.5	0.43	0.47	0.28	0.46
MgO	0.04	0.04	2.9	2.88	2.43	2.68
CaO	0.05	0	0.06	0.11	0.01	0.01
Na_2O	0.09	0.02	0.05	0.12	0.02	0.02
P_2O_5	0.07	0.01	0.06	0.09	0.03	0.04
SO_2	0	0	0	0.02	0.03	0
Cr_2O_3	0	0	0.04	0.07	0	0.03
NiO	0.04	0.09	0	0.05	0	0.15

Table B10 Group D compositional data for all ilmenite, weight %

Spectrum Label	Site 13; Spectrum 147	Site 13; Spectrum 149	Site 13; Spectrum 151	Site 13; Spectrum 153	Site 16; Spectrum 214
SiO_2	0.21	0.09	0.01	0.05	0
TiO_2	51.02	51.16	51.06	51.3	53.11
Al_2O_3	0.05	0.06	0.03	0.05	0
Fe_2O_3	46.74	46.96	47.04	46.78	45.11
MnO	1.51	1.51	1.58	1.63	1.4
MgO	0.08	0.01	0.06	0	0
CaO	0.1	0.08	0.04	0.06	0
Na_2O	0.11	0.05	0.05	0.05	0
P_2O_5	0.05	0	0.1	0.05	0
SO_2	0	0	0	0	0
Cr_2O_3	0	0	0.03	0	0
NiO	0.13	0.08	0	0.03	0

Table B10 continued

Spectrum Label	Site 16; Spectrum 220	Site 33; Spectrum 250	Site 33; Spectrum 252	Site 33; Spectrum 253	Site 33; Spectrum 254	Site 33; Spectrum 255
SiO_2	0	0	0	0	0	0
TiO_2	52.58	52.98	51.84	52.63	52.25	52.75
Al_2O_3	0	0	0	0	0	0
Fe_2O_3	45.2	45.15	45.68	45.42	45.15	45.37
MnO	1.66	1.56	1.74	1.4	1.29	1.48
MgO	0	0	0	0	0	0
CaO	0.18	0	0.32	0	0	0
Na_2O	0	0	0	0	0	0
P_2O_5	0.07	0.03	0.1	0.01	0	0.03
SO_2	0	0	0	0	0	0
Cr_2O_3	0	0	0	0	0	0
NiO	0	0	0	0	0	0

Table B11 Group E compositional data for all ilmenite, weight %

Spectrum Label	Site 2; Spectrum 6	Site 2; Spectrum 7	Site 14; Spectrum 97	Site 14; Spectrum 101	Site 14; Spectrum 103	Site 14; Spectrum 104	Site 13; Spectrum 80
SiO_2	0	0	0	0	0	0	0
TiO_2	28.24	27.16	52.78	55.21	53.17	52.56	53.32
Al_2O_3	0.37	0.39	0.08	0.08	0	0	0
Fe_2O_3	69.9	71.1	44.26	43.07	44.87	45.07	45.04
MnO	1.49	1.35	1.99	1.18	1.59	1.6	1.61
MgO	0	0	0	0	0	0	0
CaO	0	0	0	0	0	0.16	0
Na_2O	0	0	0.37	0.22	0	0	0
P_2O_5	0	0	0	0	0	0	0
SO_2	0	0	0	0	0	0	0
Cr_2O_3	0	0	0	0	0	0	0
NiO	0	0	0	0	0	0	0

Table B11 continued

Spectrum Label	Site 13; Spectrum 86	Site 13; Spectrum 96	Site 17; Spectrum 138	Site 17; Spectrum 139	Site 17; Spectrum 142	Site 17; Spectrum 143
SiO_2	1.44	0	0	0	0	0
TiO_2	51.57	52.81	52.93	52.57	52.68	52.72
Al_2O_3	0.27	0	0	0	0	
Fe_2O_3	44.57	45.15	45.24	45.41	45.28	44.9
MnO	1.52	1.68	1.64	1.73	1.49	1.59
MgO	0	0	0	0	0	0
CaO	0	0	0	0	0	0.28
Na_2O	0	0	0	0	0	0
P_2O_5	0	0	0	0	0	0
SO_2	0	0	0	0	0	0
Cr_2O_3	0	0	0	0	0	0
NiO	0	0	0	0	0	0

Table B12 Group A compositional data for all apatite, weight %

Spectrum Label	Site 1; Spectrum 39	Site 1; Spectrum 44
SiO_2	9.16	9.02
Al_2O_3	0.05	0.03
Fe_2O_3	1.13	1.14
MnO	0	0
MgO	0	0
CaO	41.44	42.83
Na_2O	0.26	0.51
P_2O_5	30.07	30.46
SO_2	0	0.05
NiO	0	0
Y_2O_3	0	0
La_2O_3	3.44	2.88
CeO_2	7.74	7.41
Pr_2O_3	0	0.88
Nd_2O_3	4.6	4.73
Pm_2O_3	0	0
Sm_2O_3	0	0
Gd_2O_3	0	0
Dy_2O_3	0	0
Ta_2O_5	0	0
Total	98.12	100

Table B13 Group B compositional data for all apatite, weight %

Spectrum Label	Site 23; Spectrum 192	Site 23; Spectrum 194	Site 23; Spectrum 196
SiO_2	5.15	5.92	6.06
Al_2O_3	0	0	0
Fe_2O_3	0	0	0
MnO	0	0	0
MgO	0	0	0
CaO	46.01	42.47	45.19
Na_2O	0	0.15	0
P_2O_5	32.35	28.95	30.36
SO_2	0	0	0
NiO	0	0	0
Y_2O_3	0	0	0
La_2O_3	0.99	1.1	1.02
CeO_2	2.8	2.92	3.05
Pr_2O_3	1.77	2.45	2.27
Nd_2O_3	5.4	6.1	5.74
Pm_2O_3	0.78	1.09	0.81
Sm_2O_3	3.04	3.71	4.12
Gd_2O_3	0.52	1.41	0.36
Dy_2O_3	0.21	0.38	0
Ta_2O_5	0	1.31	0
Total	99.02	99.06	98.97

Table B14 Group C compositional data for all apatite, weight %

Spectrum Label	Site 12; Spectrum 140	Site 12; Spectrum 140
SiO_2	0.12	0.08
Al_2O_3	0.59	0.47
Fe_2O_3	0.08	0.09
MnO	1.1	0.96
MgO	41.92	42.32
CaO	0.15	0.12
Na_2O	54.22	54.88
P_2O_5	0.16	0.17
SO_2	1.61	0.86
NiO	0.05	0.06
Y_2O_3	0	0
La_2O_3	0	0
CeO_2	0	0
Pr_2O_3	0	0
Nd_2O_3	0	0
Pm_2O_3	0	0
Sm_2O_3	0	0
Gd_2O_3	0	0
Dy_2O_3	0	0
Ta_2O_5	0	0
Total	100	100

Table B15 Group D compositional data for all apatite, weight

Spectrum Label	Site 13; Spectrum 144	Site 33; Spectrum 258	Site 33; Spectrum 259	Site 34; Spectrum 269	Site 35; Spectrum 272
SiO_2	7.08	3.78	3.29	3.08	2.85
Al_2O_3	0.11	0	0	0	0
Fe_2O_3	0.99	1.29	0.84	0.81	0.71
MnO	0.12	0	0	0	0
MgO	0	0	0	0	0
CaO	43.68	47.87	49.53	49.37	49.58
Na_2O	0.39	0.13	0.1	0.18	0.18
P_2O_5	31.17	34.43	35.49	35.08	36.41
SO_2	0	0	0	0	0
NiO	0	0	0	0	0
Y_2O_3	0	1.7	1.78	1.71	0
La_2O_3	3.09	0	0	1.48	1.39
CeO_2	7.29	1.05	0.96	3.76	3.37
Pr_2O_3	0.9	4.02	3.66	0.75	0.33
Nd_2O_3	4.62	0.76	0.44	2.31	2.05
Pm_2O_3	0	2.48	2.15	0	0
Sm_2O_3	0.57	0.1	0.28	0.4	0.27
Gd_2O_3	0	0.86	0.24	0	0
Eu_2O_3	0	0.55	0.22	0	0.32
Ta_2O_5	0	0	0	0.06	0
Total	100	99.03	98.98	99.06	98.9

Table B16 Group A compositional data for all pyrite, element %

Spectrum Label	Site 20; Spectrum 175
SiO_2	0.33
Fe_2O_3	46.79
CaO	0.3
P_2O_5	0.18
SO_2	51.85

Table B17 Group B compositional data for all pyrite, element %

Spectrum Label	Site 10; Spectrum 130
SiO_2	0.24
Fe_2O_3	47.95
MnO	0.09
CaO	0.23
P_2O_5	0.07
SO_2	51.17
Cr_2O_3	0.01
NiO	0.02
Cu_2O	0.13

Table B18 Group D compositional data for all pyrite, element %

Spectrum Label	Site 7; Spectrum 18	Site 7; Spectrum 19	Site 7; Spectrum 20	Site 7; Spectrum 21	Site 26; Spectrum 215
SiO_2	0	0	0.55	1.77	0
TiO_2	0	0	0	1.61	0
Fe_2O_3	49.13	47.69	46.19	80.78	46.15
MnO	0	0	0	0	0
CaO	0.15	0.11	0.29	0.45	0.17
P_2O_5	0	0	0	0	0.1
SO_2	50.72	52.08	51.95	13.49	52.69
Cu_2O	0	0.12	0	1.9	0

Table B19 Group E compositional data for all pyrite, element %

Spectrum Label	Site 13; Spectrum 83	Site 14; Spectrum 107	Site 17; Spectrum 140	Site 15; Spectrum 118	Site 15; Spectrum 120
Fe_2O_3	43.01	46.09	44.21	44.57	45.89
SO_2	54.77	52.72	54.44	54.03	52.68
Pr_2O_3	0.12	0	0	0	0.17
Nd_2O_3	0	0	0	0	0
Pm2O3	0.31	0	0.17	0.16	0.11
Sm_2O_3	0.42	0	0.02	0.08	0.05
Eu_2O_3	0.35	0	0.15	0.06	0
Ta_2O_5	0.06	0.11	0.03	0.04	0.09
HgO	0.97	0.86	0.88	1.04	0.78

Table B20 Group A compositional data for all zircon, weight %

Spectrum Label	Site 1; Spectrum 24	Site 1; Spectrum 25	Site 1; Spectrum 40	Site 1; Spectrum 42	Site 5; Spectrum 86	Site 2; Spectrum 48	Site 3; Spectrum 56
SiO_2	22.16	22.12	22.45	22.46	22.16	22.17	22.36
ZrO_2	76.92	76.74	76.54	76.31	77.04	76.89	76.79
HfO_2	0.92	1.14	1.01	1.23	0.79	0.94	0.85

Table B21 Group D compositional data for all zircon, weight %

Spectrum Label	Site 32; Spectrum 244	Site 32; Spectrum 246	Site 32; Spectrum 249
SiO_2	23.19	22.91	23.09
Fe_2O_3	0	0.86	0
ZrO_2	76.09	75.47	75.76
HfO_2	0.73	0.76	1.04

APPENDIX C - Melt Inclusions

Table C1. Inclusion type summary table for all melt inclusions analyzed, Group A – D.

Sample ID	Glass Inclusion Type	Gas Bubbles (Y/N)	Distance from Rim	Size	Color
GA_MI1	Wholly enclosed	N	30 µm	220 x 110 µm	Clear
GA_MI2	Reentrant	N	Connected	130 x 90 µm	Clear
GA_MI3	Wholly enclosed	Y	250µm	75 x 60 µm	Greenish-clear
GA_MI4	Wholly enclosed	Y	180µm	90 x 70 µm	Brown
GA_MI5	Reentrant	Y	Connected	320 x 140 µm	Greenish-clear
GB_MI4	Reentrant	N	Connected	240 x 80 µm	Clear
GC_MI1	Hourglass	Y	50 µm	150 x 150 µm	Greenish-clear
GC_MI2	Reentrant	Y	Connected	150 x 50 µm	Brown
GC_MI5	Reentrant	Y	Connected	290 x 140 µm	Brown
GD_MI4	Wholly enclosed	Y	90 µm	110 x 100 µm	Brownish-clear
GD_MI6	Hourglass	Y	Connected	400 x 130 µm	Brown

Table C2. H_2O and CO_2 concentrations for all Group A melt inclusions.

Sample ID	H_2O (wt%)	CO_2 (ppm)
Group A - DC11_1P		
GA_MI1	1.550	18.995
	1.310	45.339
	1.418	67.573
GA_MI2	2.459	110.511
	1.238	59.113
	2.998	115.099
	2.597	178.651
GA_MI3	2.760	54.750
	2.647	6.272
GA_MI4	3.057	11.913
	3.694	4.786
GA_MI5	1.550	18.995
	1.310	45.339
	1.418	67.573

Table C3. H_2O and CO_2 concentrations for all Group B melt inclusions.

Sample ID	H_2O (wt%)	CO_2 (ppm)
Group B - DC11_33P8		
GB_MI4	0.5174	4.0754
	0.3486	4.5241
	0.3123	2.0354
	0.3279	15.1540

Table C3. H_2O and CO_2 concentrations for all Group C melt inclusions.

Sample ID	H_2O (wt%)	CO_2 (ppm)
Group C - MS10_28DC-A		
GC_MI1	1.746	59.341
	1.729	3.296
GC_MI2	1.700	15.511
	1.646	6.203
	1.850	12.419
GC_MI5	1.574	44.101
	1.540	45.726
	2.147	19.661

Table C4. H_2O and CO_2 concentrations for all Group D melt inclusions.

Sample ID	H_2O (wt%)	CO_2 (ppm)
Group D - DC11_33P7		
GD_MI6	0.459	2.681
	0.799	25.965
	0.767	41.593
GD_MI4	0.678	9.624
	0.638	5.929
	0.729	10.696

APPENDIX D - TitaniQ Thermometry

Table D1. Aluminum and titanium concentrations of quartz phenocrysts analyzed with EMP from Group A. Annotated site locations found in Figure D1.

Group - Site #	Al (ppm)	Ti (ppm)	Location
DCT-A_site8Q1	65	80	1
DCT-A_site8Q1	79	82	2
DCT-A_site8Q1	69	140	3
DCT-A_site8Q1	81	109	4
DCT-A_site13Q1	63	0	1
DCT-A_site13Q1	58	27	2
DCT-A_site13Q1	82	11	3
DCT-A_site13Q1	71	76	4
DCT-A_site12Q1	64	80	1
DCT-A_site12Q1	66	89	2
DCT-A_site12Q1	75	88	3
DCT-A_site12Q1	70	109	4

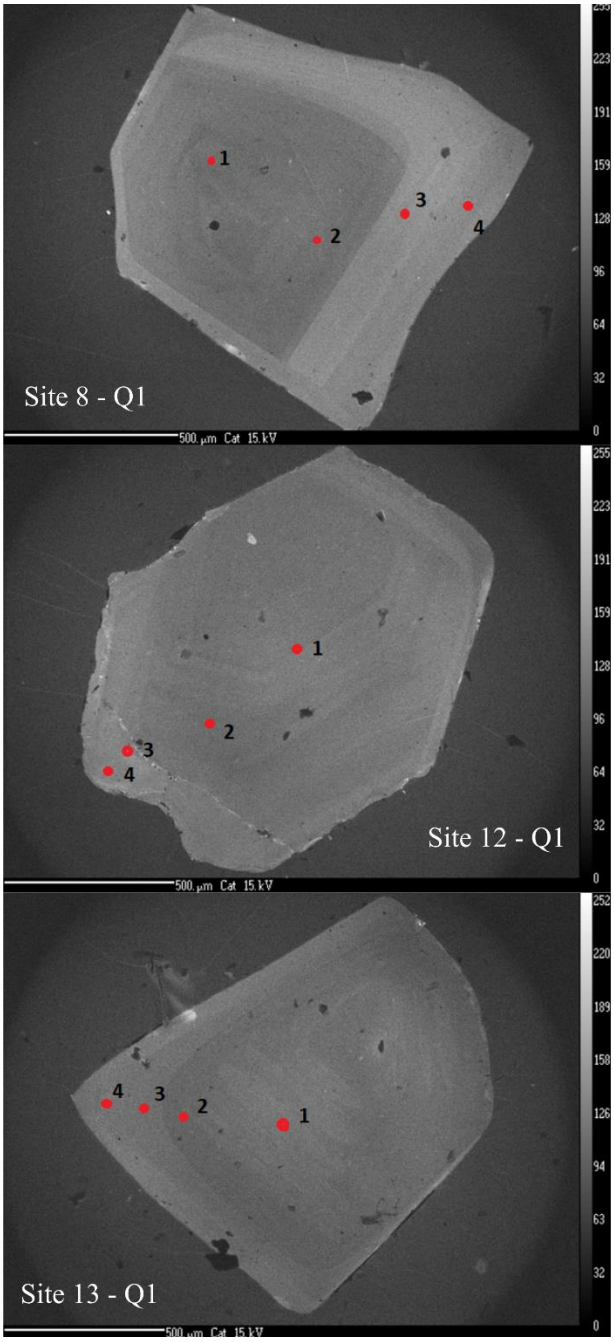

Figure D1. Annotated cathodoluminescence images of group A quartz. Numbers coincide with locations and Al and Ti concentrations reported in Table D1.

Table D2. Aluminum and titanium concentrations of quartz phenocrysts analyzed with EMP from Group B. Annotated site locations found in Figure D2.

Group - Site #	Al (ppm)	Ti (ppm)	Location
DCT-B_site15Q2	69	32	1
DCT-B_site15Q2	54	29	2
DCT-B_site15Q2	58	83	3
DCT-B_site15Q2	134	82	4
DCT-B_site17Q2	77	74	1
DCT-B_site17Q2	68	78	2
DCT-B_site17Q2	84	98	3
DCT-B_site17Q2	75	112	4
DCT-B_site13Q1	52	42	1
DCT-B_site13Q1	67	58	2
DCT-B_site13Q1	68	66	3
DCT-B_site13Q1	66	63	4

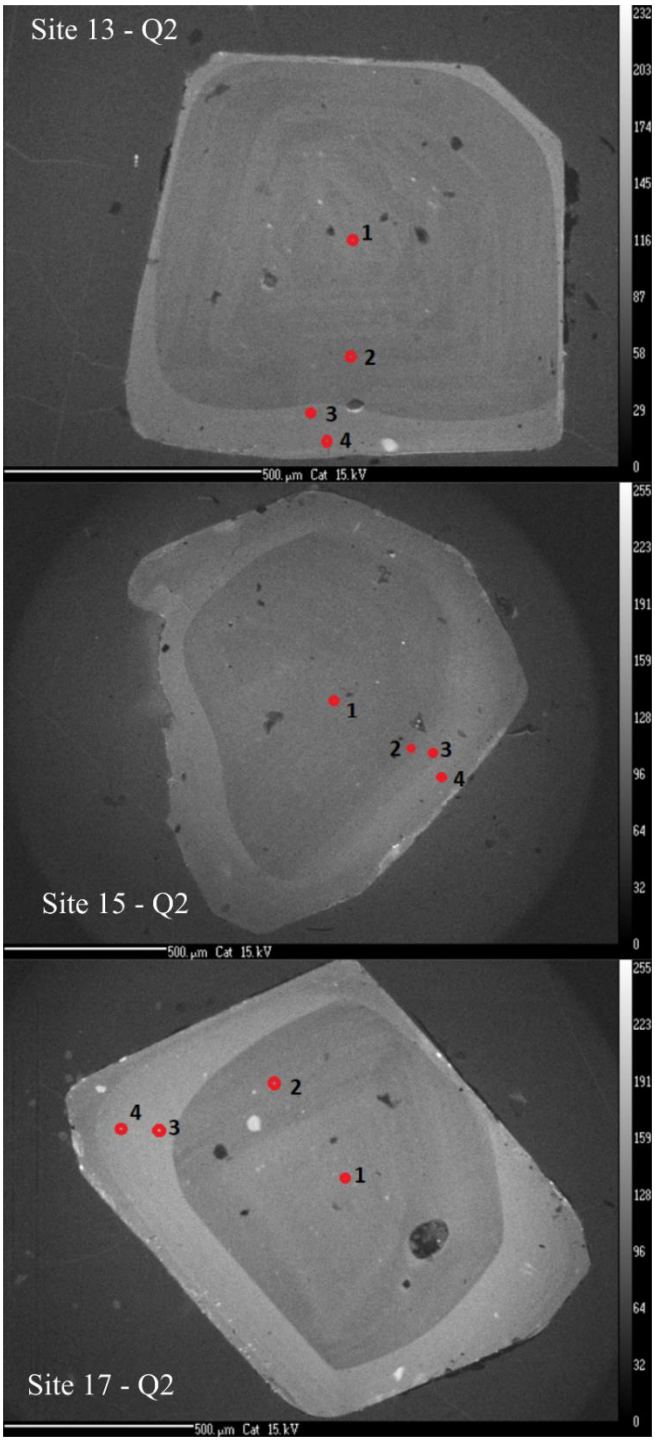

Figure D2. Annotated cathodoluminescence images of group B quartz. Numbers coincide with locations and Al and Ti concentrations reported in Table D2.

Table D3. Aluminum and titanium concentrations of quartz phenocrysts analyzed with EMP from Group C. Annotated site locations found in Figure D3.

Group - Site #	Al (ppm)	Ti (ppm)	Location
DCT-C_site18Q3	76	61	1
DCT-C_site18Q3	65	32	2
DCT-C_site18Q3	95	100	3
DCT-C_site18Q3	96	106	4
DCT-C_site20Q3	76	58	1
DCT-C_site20Q3	83	0	2
DCT-C_site20Q3	84	83	3
DCT-C_site20Q3	95	91	4
DCT-C_site201Q3	73	39	1
DCT-C_site201Q3	75	47	2
DCT-C_site201Q3	76	106	3
DCT-C_site201Q3	77	93	4

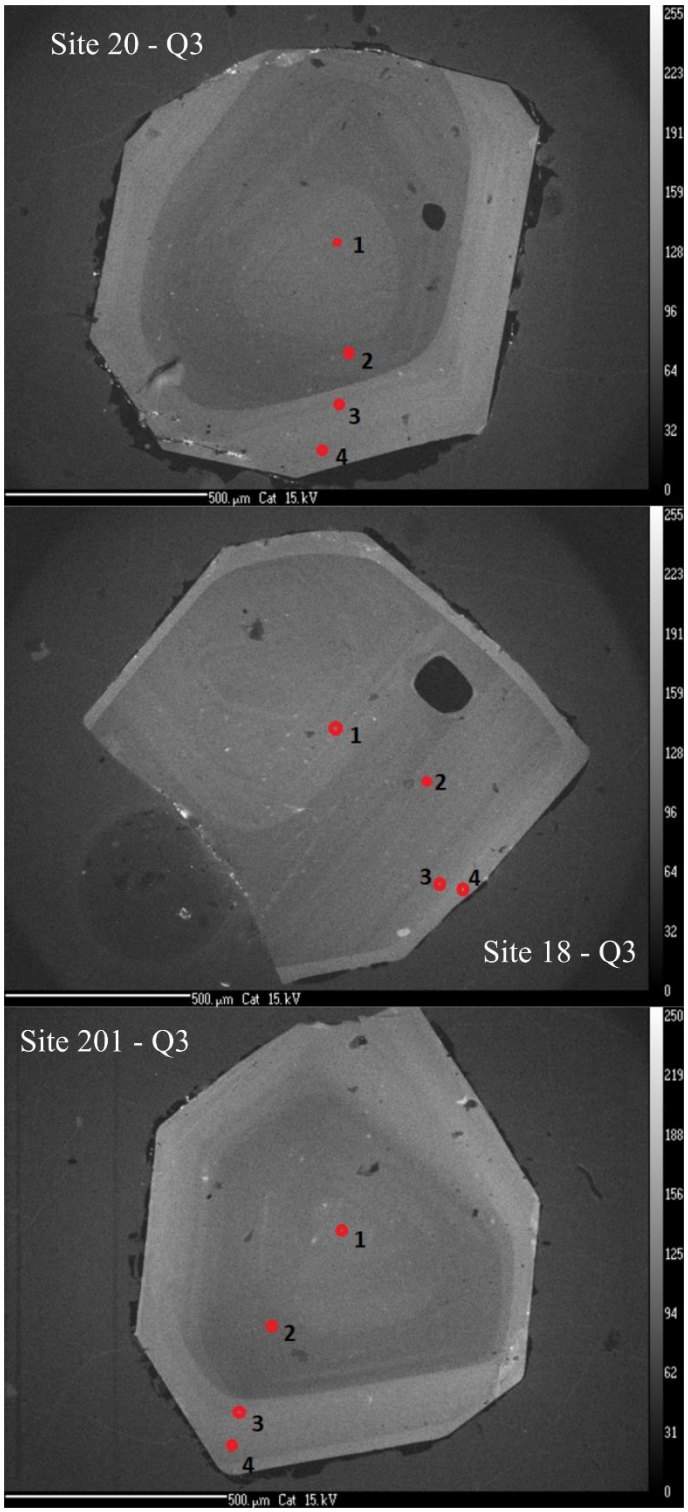

Figure D3. Annotated cathodoluminescence images of group C quartz. Numbers coincide with locations and Al and Ti concentrations reported in Table D3.

Table D4. Aluminum and titanium concentrations of quartz phenocrysts analyzed with EMP from Group D. Annotated site locations found in Figure D4.

Group - Site #	Al (ppm)	Ti (ppm)	Location
DCT-D_site1Q4	61	51	1
DCT-D_site1Q4	80	61	2
DCT-D_site1Q4	104	131	3
DCT-D_site1Q4	100	121	4
DCT-D_site2Q4	77	62	1
DCT-D_site2Q4	69	56	2
DCT-D_site2Q4	72	84	3
DCT-D_site2Q4	79	78	4
DCT-D_site7Q4	53	51	1
DCT-D_site7Q4	54	59	2
DCT-D_site7Q4	69	81	3
DCT-D_site7Q4	80	92	4

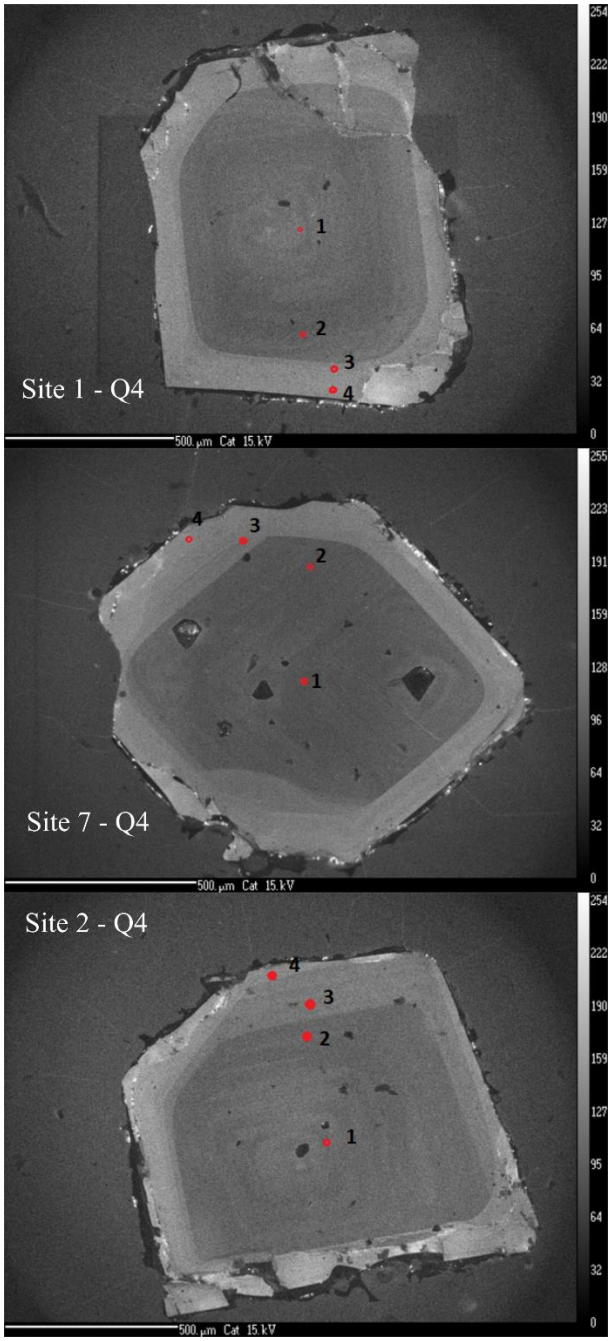

Figure D4. Annotated cathodoluminescence images of group D quartz. Numbers coincide with locations and Al and Ti concentrations reported in Table D4.